Journal of Non-Crystalline Solids 668 (2025) 123721

Contents lists available at ScienceDirect

Journal of Non-Crystalline Solids

journal homepage: www.elsevier.com/locate/jnoncrysol

Establishement of generalized empirical force-fields for sulfide glasses and crystals used as superionic electrolytes in all-solid-state batteries

L.-M. Poitras, M. Micoulaut *

Sorbonne Université, Laboratoire de Physique Théorique de la Matière Condensée, CNRS UMR 7600, 4 Place Jussieu, 75252 Paris Cedex 05, France

ARTICLE INFO

Keywords:
Sulfide glasses and crystals
Molecular dynamics simulations
Structural properties
electrolytes

ABSTRACT

A generalized force-field of Born–Mayer type is proposed for sulfide crystals and glasses containing a network former (e.g. SiS_2) and an alkali or alkaline earth sulfide modifier (e.g. Li_2S or MgS). These systems which are analogous to the archetypal and popular alkali silicates have been rarely described in the literature from molecular simulations due to a lack of interaction potentials, although they have become tremendously attractive as superionic electrolytes in all-solid state batteries. The force-field also contains a harmonic 3-body potential able to describe the role of bridging sulfur atoms between Group III (Al), Group IV (Si,Ge) and Group V (P) polyhedra, and is needed in order to obtain a first sharp diffraction peak compatible with X-ray or neutron scattering experiments in the glassy state. The fitting procedure builds on a least square minimization of numerical data with respect to crystallographic positions of crystalline phases together with a minimization of the spread between computed and experimental scattering functions in the glassy state. Results indicate an excellent reproduction of structural properties of the latter, and additional analysis reveals the usual features encountered in alkali silicates: progressive depolymerization of the base network, distribution of Q^n species with changing composition, breakdown of the ring structure. Atomic scale results in the glassy state for unreported alkaline earth thiosilicate and thiogermanate glasses suggest the similar role played by Mg, Ca or Ba with respect to alkali counterparts (Li, Na). The force field being able to reproduce realistic structures for a variety of sulfide glasses, it opens new avenues to tackle from classical molecular dynamics simulation mechanical, dynamic and electric properties of disordered sulfide electrolytes in the context of all solid state battery applications, together with properties arising from interfaces such as glass ceramics or features from crystallization.

1. Introduction

Fast ion batteries have attracted a broad attention because of their intensive use in mobile phones, electric bikes, scooters, larger vehicles [1,2]. These setups consist of an alkali-based (usually Li) oxide cathode together with an electrolyte that ensures conduction during charge and discharge cycling. As they represent a safety hazard because of the presence of flammable polymeric liquid electrolytes and the possibility of electrical shortcuts with the growth of Li dendrites connecting the two electrodes, there have been successful attempts to introduce solid electrolytes instead [3] such as the popular $Li_{10}GeP_2S_{12}$ (LGPS [4]) system. Among such solid materials, amorphous or glassy electrolytes [5] are also considered as promising candidates for battery applications because of the possibility to alloy a number of components into base materials which permits to continuously improve crucial properties such as ionic conduction or mechanical properties [6] at the electrode–electrolyte interface. The other reason of interest is the important conductivity level (10^{-3} Ω^{-1} cm^{-1}) which can now be achieved in highly depolymerized sulfide glasses such as SiS_2–$2Li_2S$ [7,8] or P_2S_5–$3Li_2S$, the latter having inspired a large number of studies because of its important level of conductivity [9–12]. The interest in modified sulfide glasses containing a network former such as SiS_2 or GeS_2 and an alkali or alkaline earth sulfide termed as 'modifier' (e.g. Na_2S or Li_2S) has, therefore, increased in the very recent years. There are many reasons for this increased interest which is of basic and applied nature. First, with the presence of the more polarizable sulfur atom and a reduced electronegativity difference between atomic species, one expects to have different bonding features and physico-chemical properties with respect to the archetypal oxide counterparts such as e.g. silicates or borates. These manifest in profound differences of network topology: rings, tetrahedral connections, chemical defects, angular distributions etc. Secondly, the increased polarization is thought to increase the ionic conductivity in sulfide glasses and this has been acknowledged by a certain number of studies over the past decades [8].

* Corresponding author.
E-mail address: mmi@lptl.jussieu.fr (M. Micoulaut).

https://doi.org/10.1016/j.jnoncrysol.2025.123721
Received 27 May 2025; Received in revised form 11 July 2025; Accepted 30 July 2025
Available online 8 September 2025

1.1. Atomic simulations of sulfides : lack of interaction potentials

Computational techniques using ab initio (density functional theory (DFT) based) or classical molecular dynamics (MD) simulations are insightful and permit to establish relationships between such physico-chemical features and the atomic scale properties averaged in appropriate statistical ensembles. When compared to the corresponding oxides and the huge database of simulations on e.g. silicates [13], sulfide glasses and liquids have received only a limited attention due in part to the difficulty in treating correctly the covalent bond linked with the reduced charge separation. This induces a certain number of unique structural properties typical of chalcogenide network formers such as Ge–Ge or S–S homopolar defects or edge-sharing (ES) tetrahedra. Early efforts have been achieved from classical modeling [14–16] but led to spurious results in terms of coordination numbers with e.g. five-fold Si atoms or a rather poor reproduction of experimental structure functions accessed from diffraction (pair correlation function $g(r)$, structure factor $S(k)$). Recent scattering experiments (X-ray [7,17,18] or neutron [19,20]) on various compositions of e.g. thiosilicate glasses have actually completely ruled out certain of these reported force fields. Efforts on chalcogenide network formers have not been more successful [21,22]. The classical simulation of chalcogenide network formers such as GeS_2, As_2Se_3 or $GeSe_2$, therefore, remains a challenging task because of the presence of these specific structural features and needs most of the time a full electronic account of the chemical bonding via *ab initio* descriptions [23–29]. DFT, however, has its own limitations in terms of time (100's of picoseconds) and systems size (100's of atoms) which prevents from extensive investigations of the ion dynamics at low temperature. Because of the growing interest in sulfides, and because there is need to consider larger systems on longer simulation time in order to access e.g. mechanical or electric properties with the goal of battery applications, it becomes mandatory to establish classical force-fields for the description of modified chalcogenides containing conducting ions. Classical models have emerged in the recent years on sulfide glasses, and these include $SiS_2 - Na_2S$ [30,31], $SiS_2 - Li_2S$ [32], $P_2S_5 - Li_2S$ [33], $P_2S_5 - Li_2S - LiI$ [34] or $SiS_2 - Li_2S - Li_2S - LiI$ [35], such studies being validated by a growing database from scattering experiments [11,12,17,18,30].

More and more numerical force fields have also been proposed from machine learning (ML) techniques for crystalline and amorphous sulfides (e.g. Ref. [36] and [37] for a review). These appear as alternative and promising methods to *ab initio* and classical MD simulations, and will certainly lead to more efficient calculations with respect to the former in close future, although certain DFT benchmarks are often needed to establish ML potentials which not always reproduce the experimental structure as exemplified in recent studies on the popular lithium thiophosphate and thiosilicate systems [36,38]. In this respect, when they can be accurately fitted, classical MD force fields offer the most optimal balance between computational efficiency and the full control or insight of the physical basis of interatomic interactions.

1.2. Specific features regarding modified sulfides

A conventional way to quantify the short-range order (SRO) in modified glasses uses distributions of so-called Q^n-units where n represents the number of bridging atoms, oxygen (BO) or sulfur (BS), connecting two polyhedra together (Fig. 1a). The characterization of SRO is here similar to oxides and sulfides and uses essentially spectroscopic signatures (nuclear magnetic resonance (NMR) or Raman [8]) to identify specific frequencies or chemical shifts in glasses from crystalline counterparts since the structure of the latter usually contains only a single Q^n species, e.g. 100 % Q^3 in crystalline $Na_2Ge_2S_5$ (33 % modifier) or 100 % Q^0 in Li_4SiS_4 (66 % modifier). This leads to well-defined spectroscopic signatures which serve to decode corresponding spectra in glasses, and lead in most of the cases to a distribution of Q^n species [8,39,40]. The other common feature is the progressive

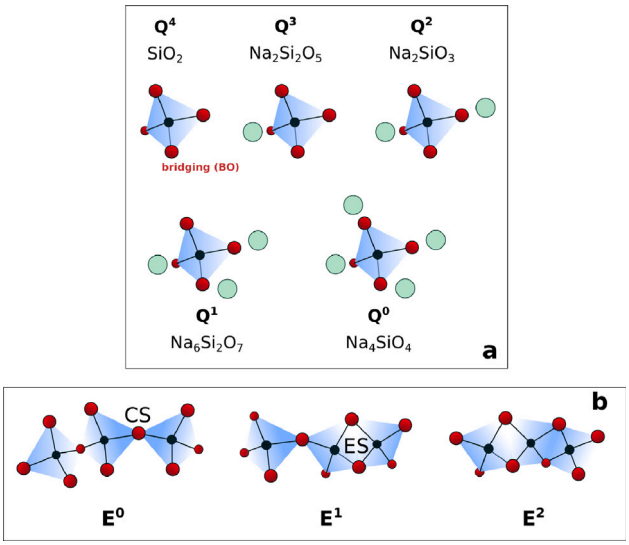

Fig. 1. (a) Typical Q^n species found in e.g. sodium modified silicates and thiosilicates, ranging from Q^4 the base tetrahedra of silica or SiS_2 to Q^0 found in crystalline orthosilicates (Na_4SiO_4). (b) Typical connections found only in modified sulfide glasses : corner-sharing (CS) and edge-sharing (ES) tetrahedra which lead to three distinct topologies : E^0, E^1 and E^2 where the superscript refers to the number of ES connections for a central tetrahedra.

depolymerization of the base network upon modifier addition so that the number of bridging atoms decreases with modified content, and the average n decreases down to zero (Q^0) for extremely depolymerized glasses. Such features are common to modified oxides, sulfides and selenides [8].

A certain number of other structural features are specific to chalcogenides (S,Se, and Te-based) among which, the tendency to form ES tetrahedral motifs (Fig. 1b). The best known example is the sulfide counterpart of silica, SiS_2, which has a crystalline structure made of infinite chains of ES tetrahedra [8], i.e. quite different in terms of network topology from the 3D corner-sharing (CS) tetrahedral structure of quartz, coesite or tridymite in the oxide counterpart. This situation is also met in GeS_2[41] or B_2S_3, the latter having a structure made of borosulfol rings [42] (the sulfide analogue of boroxol rings [43] in B_2O_3) and edge-sharing triangles $BS_{3/2}$. Early NMR work on thiosilicates has shown that the spectra are essentially dominated by three resonances associated with three possibles motifs or topologies [8,9,44–47] (Fig. 1b): a first one (E^0) containing no ES at all, a second one (E^1) having only a single edge shared tetrahedra with its neighbor, and a third one (E^2) containing two ES connections for a central tetrahedra. As for the Q^n population, the statistics of such E^k motifs evolves with modifier composition [8,48] and with its increase there is a general tendency of a double $E^2 \rightarrow E^1$, and $E^1 \rightarrow E^0$ conversion as acknowledged from specific NMR signatures.

Simulations must take into account such structural features typical of sulfides, and dedicated force-fields must among other results be able to obtain the correct fraction of ES structures and their signature in correlation functions which manifests by a prepeak in e.g. Si–Si or Ge–Ge pair correlation functions, as also detected from isotopic substituted neutron scattering [49,50] or from *ab initio* simulations [51,52] when such information on partial correlations is available.

1.3. Purpose of the contribution

In the present contribution, we build on a recent effort [32] regarding a promising electrolyte (SiS_2–Li_2S) and generalize the approach to a variety of binary systems containing a sulfide network former (SiS_2,

GeS_2, P_2S_5, Al_2S_3) and an alkali (M_2S) or alkaline earth (MS) modifier. We restrict ourselves to systems having some interest in battery applications, i.e. we will consider only glasses with light modifiers such as M=Li, Na, Mg or Ca, and will disregard elements such as K, Cs or Sr, while also targeting during the first part of this article on modifier-rich compositions and highly depolymerized networks which lead to conductivity levels interesting for applications. The choice to investigate such glass systems and compositions is essentially driven by two reasons. First, unlike crystalline sulfides (such as the popular LGPS with $\sigma \simeq 10^{-3}$ Ω^{-1} cm^{-1}), the present investigated glasses exhibit such elevated conductivities only in select cases, and only for a modifier content in the range 50–75 %. For instance, $34SiS_2$–$66Li_2S$, and $25P_2S_5$–$75Li_2S$ glasses meet this range of conductivities [44,53,54] as already stressed above. While it is known that Li-based glasses appear more promising for battery applications, Na-based crystalline electrolytes have now also become attractive [55] although Na-based glasses display a somewhat more reduced conductivity with respect to the Li counterparts [56]. Alkaline-earth (e.g. Mg-based) have been rarely considered but might also be attractive. The second motivation of the choice in compositions and systems is driven by the presence of experimental scattering functions at select compositions which permit to validate our model structures.

We fit a generalized self-consistent force field containing 2-body and select 3-body interactions able to successfully model the structural properties of sulfide glasses and crystals. Numerical approaches usually assume that atomic forces in crystals and corresponding glasses must be of the same order of magnitude so that a force field able to capture the salient atomic features in the crystalline structure should be able to describe the liquid and the glassy phase as well. Such investigations have been performed in corresponding oxides and especially silicates or silica [57–59]. This permits to fit force fields from a series of crystals and from mechanical observables such as bulk and shear modulus, the latter providing some information on the potential energy curvature. In contrast to oxides however, mechanical observables of sulfide systems have been rarely reported in the literature (see however Ref. [60]).

Here we fit empirically the crystal structure data of a variety of these binary sulfide systems within the General Utility Lattice Program (GULP) [61–63], in conjunction with (i) a relaxation technique and a vibrational eigenmode calculation that permits to select among fitted parameters those which lead to stable crystalline structures at ambient temperature, and (ii) a convergence criteria which permits to reproduce the experimental functions of corresponding glasses. The approach if fully in line with the one initiated by Pedone and coworkers for multicomponent silicates [57], and the need of interaction refinement for oxides [64,65] (i.e. 3-body forces) seems to apply as well in sulfide glasses, probably in an even more crucial fashion. The obtained structures and thermal results in both glasses and crystals are discussed and compared with measurements obtained from scattering and diffraction experiments. This permits to validate the parameters when both structure factor $S(k)$ and pair correlation function $g(r)$ are reproduced with a reasonable accuracy. We then provide in a second part different structural descriptions of the investigated glasses, and put them into perspective.

2. Methodology

2.1. General framework

Within the GULP framework [63], force-fields are fitted with respect to a certain number of observables among which experimental crystallographic data such as atomic positions, density or lattice parameters. In order to model modified sulfide network glasses, we use the Born–Mayer (BM or Buckingham) potential that contains a strong repulsive interaction at short distances, a Coulomb interaction, and a long-range attractive dispersive interaction for an atomic pair $i--j$:

$$V_{ij}(r) = A_{ij}e^{-r/\rho_{ij}} + \frac{q_i q_j}{r} - \frac{C_{ij}}{r^6}, \tag{1}$$

together with a three-body interaction for select network species (A,S) with A=Si, Ge, P, Al.

$$V_3(\theta) = k_b(\theta - \theta_0)^2 \tag{2}$$

with a cut-off for V_3 given by the minimum of the A-S correlation (typically 2.7 Å). The usefulness of an interaction constraining the angles being part of the network structure has been recently emphasized [64,65], and for the specific case of sulfides, the addition of Eq. (2) is of special importance if one wants to reproduce one of the salient characteristics which is the presence of both CS and ES polyhedral connections (in contrast to oxides), as will be discussed below. The presence of such mixed connections leads to bimodal bond angle distributions (e.g. Ge–S–Ge) in network formers [28,51] which cannot be obtained from a simple 2-body interaction such as the one proposed in Eq. (1). In all considered systems, and materials, we will use both Eqs. (1) and (2) termed as the BM3PM model hereafter. The used model is rather standard in the field of glass modeling, and bears all the advantages of a "traditional" force-field : obvious physical insight, control of the different terms appearing in Eqs. (1), and (2), easy implementation in simulation codes, etc. As a matter of fact, it has been parametrized for a variety of glasses such as e.g. the analogue silicate systems (Teter potential [66]), silica (Tsuneyuki potential [59]) or germania (Oeffner–Elliott potential [58]). The interest of developing such force-fields is also linked with the possibility to model crystal–glass (ceramics) or crystal–liquid interfaces, the latter allowing for a possible investigation of crystallization effects. We have verified that for select systems such interfaces were stable. At this stage however, and since the scope of our contribution is already quite broad, we will focus on crystal and glass phases separately.

In order to adjust the parameters of Eqs. (1) and (2), we proceed in two steps and ways (Fig. 2). Firstly, for each system, we identify the relevant and known crystalline polymorphs with reported crystallographic data. We then follow the GULP fitting procedure [63] which minimizes a weight function

$$F = \sum_{i=k}^{M} \left(C_{calc}(k) - C_{obs}(k) \right)^2 \tag{3}$$

with M observables, $C_{obs}(k)$ being the atomic coordinates of the crystalline elementary cell and the forces set to zero. The fitting procedure, i.e. the variation of the potential parameters so as to get the positions with zero forces, stops when the energy gradient becomes lower than a certain value (typically 0.01 a.u.). In the GULP approach, this default strategy can be improved by adding other observables such as high-frequency or static dielectric constants, elastic constants or bulk moduli which represent second derivatives of the energy. However, while such data are abundant in crystalline silicates [57], we are not aware of such mechanical or optical observables in corresponding crystalline sulfides so that one cannot rely on such additional observables to constrain the curvature of the energy surface. In addition, in order to take into account the fact that the fitting is performed at finite temperature, thermal forces are explicitly included in the GULP code by means of a Gibbs free energy minimization [61], rather than an energy minimization. This technique termed as "*relaxed fitting*" leads to a slight change in atomic positions.

We constrain the minimization process (3) by performing in addition a calculation of the $3N$ vibrational eigenmodes ω_i of the structure that are determined [67] from the eigenvalues of the dynamical matrix:

$$D_{i\alpha j\beta} = \frac{1}{\sqrt{m_i m_j}} \sum_R \frac{\partial^2 V}{\partial\alpha\partial\beta} e^{ik(r_{ij}+R)} \tag{4}$$

where the sum runs over the relative position change R of distance r_{ij} under the influence of a vibration. We require that most (if not all) vibrational modes satisfy $\omega_i > 0$ in order to have energy second derivatives with respect to positions (i.e. the force constant matrix) positive. This leads to stable (phonon) vibrations. The lowest three

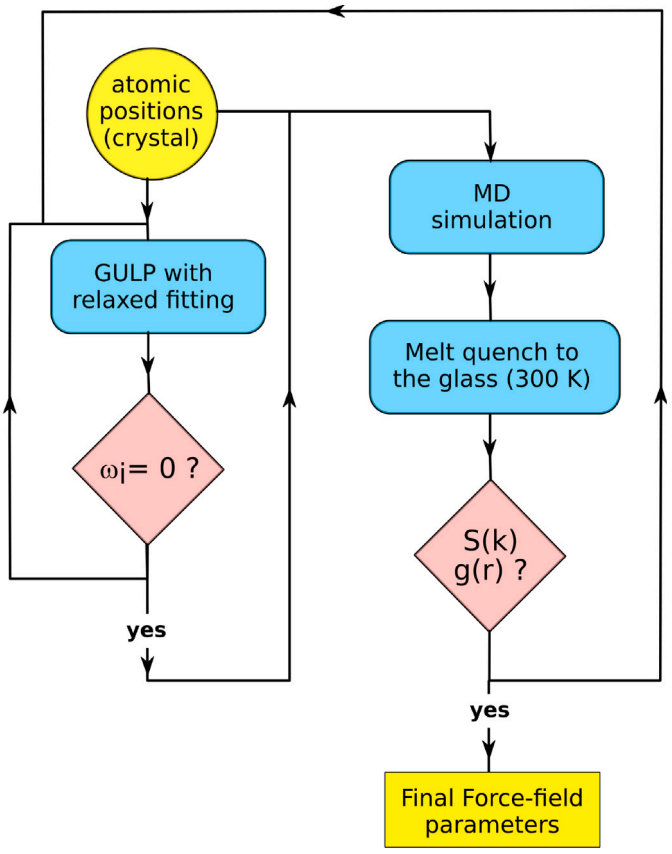

Fig. 2. Fitting procedure for sulfide crystals and glasses. It builds on a GULP fitting for crystalline polymorphs and a minimization of a goodness-of-fit parameter R_X for the glassy state when comparing to experimental structure functions ($g(r)$ and $S(k)$).

modes are zero at the center of the Brillouin zone (Γ point), and these correspond to the pure translation of the crystal lattice, identified with the acoustic branch.

Secondly, we verify that the chosen set of parameters also reproduce structural features of glasses, that is, experimental pair correlation functions $g(r)$ and neutron or X-ray structure factors $S_i(k)$ given by :

$$S_i(k) = \langle f_i \rangle^{-2} \sum_{n,m} c_n c_m f_n^i(k) f_m^i(k) S_{nm}(k) \tag{5}$$

with :

$$\langle f_i \rangle = \sum_n c_n f_n^i(k) \tag{6}$$

and $S_{nm}(k)$ are the Faber–Ziman partial structure factors. Here, the $f_n^i(k)$ represent either the atomic form factors (i=X) or the neutron scattering lengths (i=N), and c_n represents the species concentration. For X-ray scattering, the atomic form factors are usually approximated as $f_n^X(k) \approx f_n^X = Z_n$ ($f_{Si}^X = 14$, $f_S^X = 16$, etc.). In order to reach an increased accuracy, we will take into account the k-dependence of the atomic form factors using a method described in the following. Neutron diffraction require the neutron scattering lengths [68] that are tabulated: $f_n^N(k) = f_n^N$ (e.g. $f_{Si}^N = 4.149$ fm, $f_S^N = 2.847$ fm, $f_{Li} = -1.900$ fm, etc.). Partial correlations in reciprocal space in Eq. (5) are obtained from a Fourier transform of the calculated partial pair correlation functions $g_{nm}(r)$:

$$S_{nm}(k) = 1 + n_0 \int_0^\infty 4\pi r^2 \left[g_{nm}(r) - 1 \right] \frac{sin(kr)}{kr} dr \tag{7}$$

Table 1
2-body Born–Mayer parameters of the BM3PM model (Eq. (1)) that describe different sulfide crystals and glasses. Coulombic charges appear in superscripts of corresponding elements.

Atom i	Atom j	A_{ij} (kcal mol^{-1})	ρ_{ij} (Å)	C_{ij} (kcal Å^{-6} mol^{-1})
$S^{-1.2}$	$S^{-1.2}$	991 603	0.284	692
$Si^{2.4}$	$S^{-1.2}$	3 459 081	0.178	1150
$Ge^{2.4}$	$S^{-1.2}$	4 612 108	0.178	
$Al^{1.8}$	$S^{-1.2}$	4 150 897	0.178	
$P^{3.0}$	$S^{-1.2}$	714 877	0.200	
$Si^{2.4}$	$Li^{0.6}$	345 908	0.300	25 367
$Ge^{2.4}$	$Li^{0.6}$	553 453	0.300	34 591
$Al^{1.8}$	$Na^{0.6}$	691 816	0.300	27 673
$P^{3.0}$	$Li^{0.6}$	484 271	0.300	31 132
$Si^{2.4}$	$Na^{0.6}$	876 301	0.300	23 061
$Ge^{2.4}$	$Na^{0.6}$	253 666	0.300	16 140
$P^{3.0}$	$Na^{0.6}$	807 119	0.300	13 840
$Si^{2.4}$	$Mg^{1.2}$	691 816	0.300	34 591
$Ge^{2.4}$	$Mg^{1.2}$	830 180	0.300	39 203
$Si^{2.4}$	$Ca^{1.2}$	345 908	0.300	25 367
$Ge^{2.4}$	$Ca^{1.2}$	392 029	0.300	27 673
$Si^{2.4}$	$Ba^{1.2}$	1 844 840	0.300	57 651
$Ge^{2.4}$	$Ba^{1.2}$	2 767 265	0.300	80 712
$Li^{0.6}$	$S^{-1.2}$	1 153 030	0.200	461
$Na^{0.6}$	$S^{-1.2}$	5 073 319	0.200	2306
$Mg^{1.2}$	$S^{-1.2}$	1 153 030	0.200	346
$Ca^{1.2}$	$S^{-1.2}$	4 612 108	0.200	231
$Ba^{1.2}$	$S^{-1.2}$	64 569 517	0.200	9224
$Li^{0.6}$	$Li^{0.6}$	46	1.000	
$Na^{0.6}$	$Na^{0.6}$	46	1.000	
$Si^{2.4}$	$Si^{2.4}$	3 459 081	0.200	7610
$Ge^{2.4}$	$Ge^{2.4}$	5 995 741	0.200	8071
$Al^{1.8}$	$Al^{1.8}$	2 767 265	0.200	4612
$P^{3.0}$	$P^{3.0}$	691 816	0.350	115 300

where n_0 is the system density (in Å^{-3}). Using amorphous structures obtained after a melt-quench procedure from molecular dynamics simulations of the targeted systems (see methods below), we minimize over the same k range for all systems (0.6 Å^{-1} $\leq k \leq$ 12.0 Å^{-1}) a goodness-of-fit (Wright) parameter [69] that builds on a direct comparison between experimental and simulated data.

$$R_X = \left(\frac{\sum_i \left[S_{exp}(k_i) - S_{calc}(k_i) \right]^2}{\sum_i S_{exp}^2(k_i)} \right)^{1/2} \tag{8}$$

The fit stops as R_X does not evolve any more with incremental parameter change, and when the R_X variation becomes less than 0.001%. A final constraint selects parameters which lead to a near zero pressure at the glass density. We have applied this methodology to SiS_2 – Li_2S, SiS_2 – Na_2S, GeS_2 – Li_2S, GeS_2 – Na_2S, P_2S_5 – Li_2S, P_2S_5 – Na_2S glasses, in combination with the GULP approach applied to crystalline e-Li_2SiS_3, m-Li_2SiS_3, HT-Li_4SiS_4, LT-Li_4SiS_4, α-Na_2SiS_3, Na_4SiS_4, $Na_2Si_2S_5$, Mg_2SiS_4, Ca_2SiS_4, Ba_2SiS_4, Ba_3SiS_5, Li_2GeS_3, Li_4GeS_4, $Na_2Ge_2S_5$, Na_2GeS_3, $Na_6Ge_2S_7$, Na_4SiS_4, Mg_2GeS_4, Ca_2GeS_4, $BaGe_2S_5$, Ba_3GeS_5, Ba_2GeS_4, $BaGeS_3$, β-Li_3PS_4, γ-Li_3PS_4, $Li_7P_3S_{11}$, $Li_2P_2S_6$.

This dual approach (GULP for crystals and R_X for glasses) leads to a satisfying convergence of the parameters of the BM3PM model, and also permits to improve the recent force-field proposed for Li_2S-SiS_2 [32], and the force-fields proposed in the literature [30,34,70]. For other systems for which X-ray or neutron scattering data in the glassy state are unavailable, we have restricted our fitting procedure to the GULP approach to get the parameters of the BM3PM model. These include: SiS_2 – MgS, SiS_2 – CaS, SiS_2 – BaS, GeS_2 – MgS, GeS_2 – CaS, GeS_2 – BaS, Al_2S_3 – Li_2S, Al_2S_3 – Na_2S. All obtained parameters are given in Tables 1 and 2.

A final comment deals with the calculation of the pair correlation function. Due to the limited momentum transfer range accessible experimentally in scattering experiments ($k < k_{max}$), and in order to

Table 2
3-body harmonic potential (Eq. (2)) of the BM3PM model that describes different sulfide crystals and glasses.

Triplet *i-j-k*	k_b (eV.deg^{-2})	θ_0
Si – S – Si	0.8	0.0
Ge – S – Ge	0.9	0.0
Al – S – Al	0.7	0.0
P – S – P	1.0	0.0
S – Si – S	1.6	107.0
S – Ge – S	1.8	107.0
S – P – S	1.0	107.0
S – Al – S	1.4	107.0

be consistent with the experimental methodology, the functions $S_X(k)$ have been calculated with the implementation of a sinc kernel of the form $sin(k_{max}r)/k_{max}r$ that leads to typical ripples at very short distances in real space (below the first correlating distance, see below). Alternative strategies [71,72] use a convolution by a normalized Gaussian distribution with a full-width at half maximum $\propto k_{max}^{-1}$, with maximum wavevector k_{max} found between 12 and 40 Å^{-1}. Here we chose to follow as closely as possible the experimental methodology which also induces typical ripples at short distances in the calculated $g(r)$. In addition, we use for X-ray weighted functions momentum dependent form factors $f_n^X(k)$ as discussed next.

2.2. Effect of the energy dependence of the form factors

We remind that X-ray measurements in multi-component materials present unique challenges due to the complex dependency of atomic form factors on the momentum transfer k. Unlike neutron scattering, where the structure factor can be represented by a simple weighted sum of partial structure factors using constant parameters (i.e. neutron coherence lengths f_n^N), X-ray $S_X(k)$ lack an exact expression, as the k-dependence of atomic scattering form factors f_n^X varies with momentum transfer. As the atomic form factor is basically the Fourier transform of the electron density around the nucleus, it represents the scattering amplitude of a wave of energy $\vec{k}$ by an atom of electronic density $\rho(\vec{r})$[73].

$$f_n^X(\vec{k}) = \int_0^\infty \rho(\vec{r}) e^{i\vec{k}.\vec{r}} d\vec{r} \tag{9}$$

where the vectorial dependence can be simplified due to the isotropic character of glasses, and this also means that the deformation of the electronic density around a bond between two atoms is usually neglected. The basic and standard approximation uses $k = 0$ which leads to $f_n^X = Z_n$, and is known as the Warren–Krutter–Morningstar (WKM) approximation [74] in the literature, and widely used. However, this approximation has significant drawbacks, including potential inaccuracies and limitations in distinguishing structural subtleties, especially for materials containing both light and heavy elements. To fully address these issues, the calculations of the X-ray structure factor should ideally incorporate form factors that account for the precise k-dependent variations in scattering behavior. Such an approach enables a more precise calculation of $S_X(k)$ from structural models, especially in the context of a convergence process (Eq. (8)) for the establishment of a MD force-field, and an explicit expression of the atomic partial distribution function obtained by X-ray diffraction has been recently derived by Masson and Thomas [75]. Here, we implement the k-dependence of f_n^X in the calculation of $S_X(k)$ using a sum of Gaussians as proposed in the International Crystallography Table [76] which has been found to be particularly efficient up to $k = 25$ Å^{-1} :

$$f_n^X(k) \approx c + \sum_{j=1}^{4} a_j e^{-b_j \frac{k^2}{(4\pi)^2}} \tag{10}$$

where c, a_j and b_j are atomic species related coefficient given e.g. in Table 3 for the benchmark system $80GeS_2$–$20Li_2S$ used to characterize

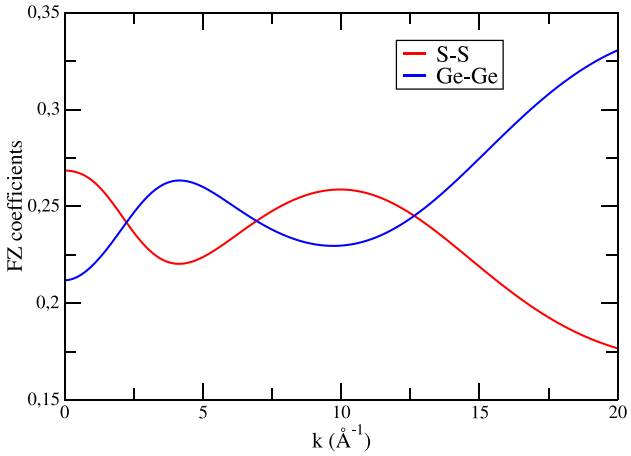

Fig. 3. Variation as a function of k of $80GeS_2$ – $20Li_2S$ Faber–Ziman coefficients $f_n^X(k)f_m^X(k)c_nc_m$ for select atomic pairs: S–S (red) and Ge–Ge (blue).

Table 3
Coefficients for the analytical approximation (Eq. (10) of $(1-x)GeS_2$ – xLi_2S form factors.

Atom	a_1 b_1	a_2 b_2	a_3 b_3	a_4 b_4	c	mean error
Li	1.1282	0.7508	0.6175	0.4653	0.0377	0.001
	3.9546	1.0524	85.3905	168.261		
Ge	16.0816	6.3747	3.7068	3.683	2.1313	0.008
	2.8509	0.2516	11.4468	54.7625		
S	6.9053	5.20340	1.4379	1.5863	0.8669	0.002
	1.4679	22.2151	0.2536	56.172		

the effect of the energy dependency of form factors. For the other reported systems of the paper, we used the $\{a_j, b_j, c\}$ values of the International Table of Crystallography [76]. The effect of Eq. (10) is exemplified for the case of Ge-S-Li systems, and Fig. 3 represents the Faber–Ziman weights for selected pairs (Ge–Ge and S–S) which indicate that variations in f_n^X can contribute, and modify the overall evaluation of the total function $S_X(k)$.

This explicit dependence (10) leads to an increased agreement of the calculated structure factor $S_X(k)$ when compared to experiments, and this appears to be particularly visible when both heavy (e.g. Ge) and light (e.g. Li) elements are present. Fig. 4 shows the comparison of $S_X(k)$ for the benchmark system $80GeS_2$ – $20Li_2S$ which clearly suggests that an explicit account of the k-dependence of the form factors leads to an improved reproduction of the entire experimental diffraction pattern, and this is especially visible in the 0–6 Å^{-1} range.

For the sake of consistency, we will, therefore, compute all X-ray structure factors with the explicit k-dependence of f_n^X used in Eq. (10). It should be noted that we do not account for the deformation of the electronic cloud around a covalent bond, which can be approximated using spherical harmonics [76]. However, given the extremely satisfying accuracy of the Gaussian approximation (Eq. (10)) in the reproduction of the upcoming structure factors for various glasses, we will disregard this issue.

2.3. Molecular dynamics

Molecular dynamics of crystals, liquids and glasses have been always, unless specified, performed on different system sizes, depending on the size of corresponding elementary crystalline cells which have been duplicated (usually 4–5 times in each direction) in order to reach sizes of about $2000 \leq N \leq 5000$, prior to a melting at high temperature, and a quench to the glassy state. The Coulombic part of the interaction potential has been treated with the Ewald sum.

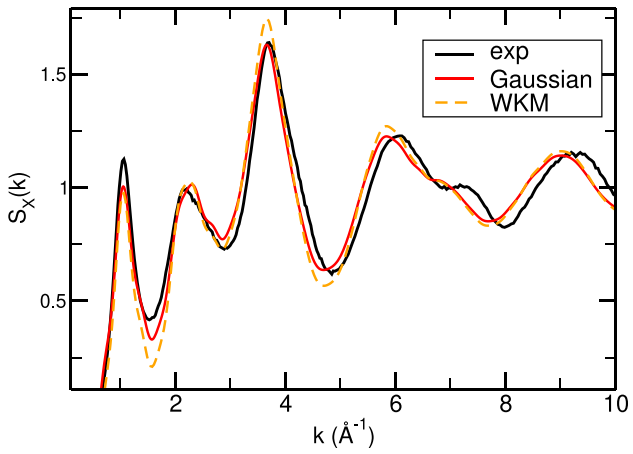

Fig. 4. Calculated structure factor $S_X(k)$ of a mass-contrasted material (80 GeS_2 – Li_2S) using the WKM approximation (i.e. constant f_n^X, broken orange curve) and the Gaussian approximation (red) of the form factors f_n^X using Eq. (10). Calculated curves are compared to the XRD experiment (black [17]).

These initial configurations have been mostly considered in NPT Ensemble with a Verlet algorithm (timestep Δt=1 fs) for the integration of the equation of motion at low temperature (100 K) in the crystalline state, in order to verify the stability and crystallographic data, to be compared with experiments. In select cases, we have also performed runs in NVT ensemble in order to quantify the presence of residual pressures at ambient conditions. For the liquid and glassy state, we have first performed a high temperature run in NPT at 2000 K for 100 ps in order to melt the crystalline alloys of the desired composition, prior to a quench to 300 K at a cooling rate of 1 K/ps and zero pressure. Resulting densities (ρ_0, η_0) have been accumulated in order to be compared to experimental glass densities. Additional liquids, and glasses have been created by a random substitution of species in order to meet the desired composition, e.g. once the crystalline Li_2SiS_3 melted and quenched to the $50SiS_2$ – $50Li_2S$ glass, we have substituted atoms in order to start $40SiS_2$ – $60Li_2S$, etc. After thermalization, statistical analysis of all glasses (structure) has been performed in NVT over 100 ps.

3. Results

We now consider each investigated system, review some basic knowledge, and discuss the relevance of the BM3PM model with respect to experimental measurements.

3.1. SiS_2-Na_2S glasses and crystals

The (100-x)SiS_2 – $x$$Na_2S$ system can form glasses [44,48] over the range 10 % ≤ x ≤ 70 %, and has five identified crystalline polymorphs that we describe together with our obtained results for select polymorphs.

3.1.1. Crystalline phases

Crystalline phases of this binary include $Na_2Si_2S_5$ (x=33 % Na_2, dithiosilicate), α-Na_2SiS_3 (50 %, metathiosilicate), β-Na_2SiS_3, $Na_6Si_2S_6$ (pseudo-pyrothiosilicate) and Na_4SiS_4 (66 %, orthothiosilicate). The low alkali-content crystalline form ($Na_2Si_2S_5$) is thought to be isomorphic [77,78] of the Ge analogue crystal ($Na_2Ge_2S_5$). Formed in orthorhombic symmetry, it is supposed to be made of a periodic replication of an adamatane-like $Si_4S_{10}^{4\ominus}$ unit [79] with two crystallographically inequivalent Q^3 species [46] (Fig. 5 right). The low temperature α-Na_2SiS_3 crystallizes in a monoclinic lattice [80] (space group P21/c) with unit cell a = 6.61 Å, b = 15.16 Å, c = 5.73 Å, β=110.26°. Its structure consists in $SiS_{4/2}$ tetrahedra sharing two corners via bridging sulfur (BS) atoms, isostructural [80] to Na_2GeS_3 whose crystallographic data have been solved [80]. The two other sulfur atoms of the cell are NBS atoms so that the general structure is thought to be made of 100 % Q^2 in E^0 configuration (Fig. 1b). Conversely, the (metastable) high temperature form β-Na_2SiS_3 is proposed to be made of edge-sharing tetrahedral species $Na_4Si_2S_6$ which are also observed in the Ge counterpart [81] or in the lithium thiosilicate high temperature phase [82] Li_2SiS_3. We are not aware of the crystallographic data (exact atomic positions in the unit cell) as the structure has been only inferred from NMR measurements [46]. Lastly, the Na_4SiS_4 phase crystallizes [83,84] in an orthorhombic space group ($P2_12_12_1$, Fig. 5 left) with cell parameters given in Table 4. The structure is made of isolated Q^0 tetrahedra in combination with Na found in 5+1 coordination and defect octahedral geometries [84] (see also Fig. 5a). The pseudo-pyrothiosilicate [85,86] $Na_6Si_2S_6$ is formed at high Na concentration and contains a homopolar Si–Si bond but while thermal results have been reported, its crystallographic positions are unknown.

Table 4
Experimental cell parameters, system density (n_0, ρ_0) and main distances of different sodium thiosilicate crystals, compared to the present calculated values from the BM3PM model in NPT Ensemble at zero pressure, and 100 K. The number N of particles is indicated for each compound. The range of interatomic distances is related to the neighbor rank between species of the unit cell, e.g. S–Na(1), S–Na(2), etc.

	Expt.	Model
$Na_2Si_2S_5$	Cmcm	N=**4608**
a (Å)	12.68 [77]	12.76
b (Å)	12.72 [77]	12.80
c (Å)	10.35 [77]	10.41
n_0 (Å^{-3})	0.043 [77]	0.042
ρ_0 (g cm^{-3})	2.09 [77]	2.05
d_{Si-S} (Å)	2.05–2.13 [78]	2.15
d_{Na-S} (Å)	2.83–2.93 [78]	2.90
α-Na_2SiS_3	P21/c	N=**3000**
a (Å)	6.61 [80]	6.55
b (Å)	15.16 [80]	15.02
c (Å)	5.73 [80]	5.60
n_0 (Å^{-3})	0.045 [80]	0.046
ρ_0 (g cm^{-3})	2.10 [80]	2.16
d_{Si-S} (Å)	2.14 [80]	2.10
d_{Na-S} (Å)	2.70–3.06 [80]	2.79
Na_4SiS_4	$P2_12_12_1$	N=**3240**
a (Å)	13.68 [84]	13.95
b (Å)	8.78 [84]	8.96
c (Å)	6.89 [84]	7.03
n_0 (Å^{-3})	0.043 [84]	0.042
ρ_0 (g cm^{-3})	1.99 [84]	1.89
d_{Si-S} (Å)	2.01–2.15 [84]	1.99–2.15
d_{Na-S} (Å)	2.63–2.96 [84]	2.63–3.11

Once the fitting procedure is applied, we find the force-field parameters for the sodium thiosilicate system (Table 1). These lead to a correct reproduction of the crystallographic data for the three considered crystals. The BM3PM model leads to stable structures with cell parameters that slightly increase in $Na_2Si_2S_5$ (e.g. a=12.76 Å, see Table 1) with respect to reported experimental data [77] (12.68 Å). Note that the proposed adamatane-like $Si_4S_{10}^{4\ominus}$ unit for $Na_2Si_2S_5$ is only tentative [77,78] so that the starting crystallographic data on which we have applied the force field might not correspond to the true structure of sodium dithiosilicate and might need some additional experimental refinement, although the force-field maintains this molecular grouping during the NPT simulation (Fig. 5 right). At zero pressure in NPT Ensemble, the densities and cell parameters for the two high Na content polymorphs are found to be either slightly larger (e.g. n_0=0.046 Å^{-3} in α-Na_2SiS_3) than the experimental counterparts [78] (e.g. n_0=0.045 Å^{-3}) or smaller as in Na_4SiS_4 (see also Fig. 7). Typical calculated bonding distances are recovered, i.e. we find for the maximum of the

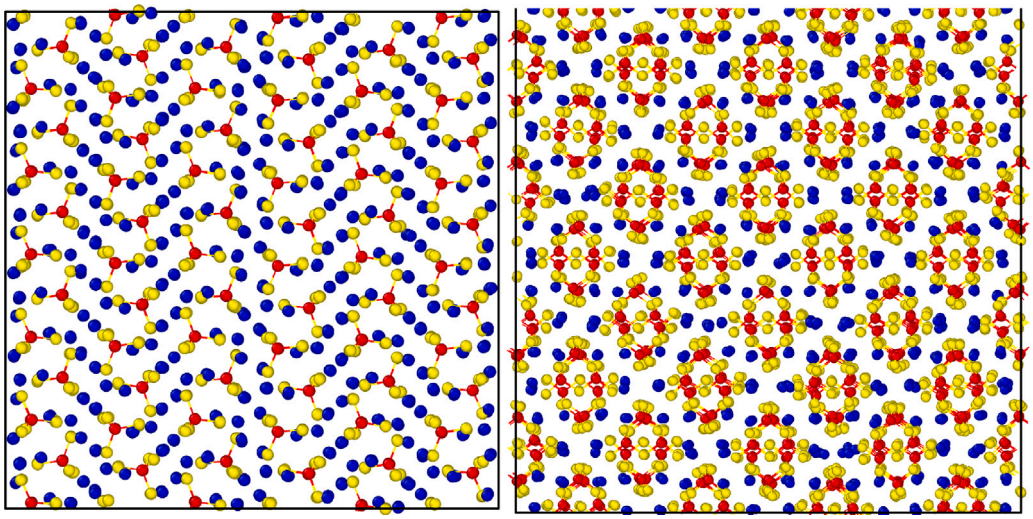

Fig. 5. 2D view of the simulation box after 100 ps trajectory in NPT at 100 K and zero pressure of the Na_4SiS_4 in (a, c) direction (left) and the $Na_2Si_2S_5$ crystalline phases in (a, b) direction (right). Note that the simulation maintains in the latter the proposed adamatane-like $Si_4S_{10}^{4\ominus}$ unit [79]. Sulfur, Silicon and Sodium are colored in yellow, red, and blue, respectively.

principal peak in the $g(r)$ function a distance d_{Si-S}=2.05 Å (experimentally [84] 2.01–2.15 Å in Na_4SiS_4, depending on the neighbor rank, i.e. Si(1)–S(1), Si(1)–S(2), etc.).

3.1.2. Sodium thiosilicate glasses

The force-field is able to reproduce the main structural features in the glassy state in reciprocal and real space as we obtain for two select compositions (50:50 and 66:34) a calculated X-ray weighted structure factor $S_X(k)$ that is in excellent agreement with corresponding experimental measurements [30,87], and leads to Wright parameters R_X that are exceptionally low (0.20–0.26%). Fig. 6a showcases the results of the interaction potential which is able to reproduce the position, amplitude and width of the principal peaks of $S_X(k)$, observed at 2.3 $Å^{-1}$, 4.0 $Å^{-1}$ and the first sharp diffraction peak measured at 1.2 $Å^{-1}$. Eqs. (1) and (2) provide, indeed, a description of reciprocal space properties that are, by far, improved with respect to previous simulations on the same system (Fig. 6c): an *ab initio* simulation [30] (black curve), and a classical 2-body BM potential of the same form as Eq. (1) with different parameters (A_{ij}, ρ_{ij}, C_{ij}) that have been "improved" from an initial parametrization [30] but with an obvious limited success [31] (green curve). The low-k peaks representing the medium-range order exhibit, indeed, a clear shift with respect to experiments for these previous simulation results, the FSDP being poorly reproduced, or even absent in the *ab initio* simulation [30]. Noteworthy is the fact that recent DFT simulations [87] using a plane wave basis and an exchange correlation functional suited for network-forming sulfides have led to a very good reproduction of the structure factor $S_X(k)$, of the same level of agreement as the present classical force-field. An estimation of the Wright parameter (Eq. (8)) R_X over the range 0.6 $Å^{-1} \leq k \leq$12.0 $Å^{-1}$ for the three simulations of the NS glass (Fig. 6c) leads to R_X=1.22% (ab initio [30]), 1.35% (classical force field [31]) and 0.20% for the present work which confirms the quantitative improvement brought by the new set of parameters given in Tables 1 and 2.

With the increase of Na_2S content (Fig. 6a), we note that the principal peak at 2.3 $Å^{-1}$ broadens, and shifts to higher wavevector, and this is due to the growing contribution of the Na–S partial structure factor (not shown), this correlation contributing also to the intensity of the peak found at 3.70 $Å^{-1}$.

In real space, we also obtain a very good reproduction of the experimental total pair correlation function [87] (Fig. 8) which contains a principal peak at 2.11 Å corresponding to the Si-S bond distance (the apex of the $SiS_{4/2}$ tetrahedra) for all Na-based systems, and very close to the bond distance d_{Si-S} determined both experimentally and numerically in crystals (Table 4). Additional peaks found at 3.61 Å and 2.81 Å are visible, and these correspond to S–S and Na–S bond distances, respectively that are clearly detected in the calculated partial correlation functions $g_{ij}(r)$ (Figs. 9c and e). The Si–Si partial (Fig. 9a) contains features revealing ES connections with a typical peak found at 3.0 Å that corresponds to the Si–Si correlating distance involved in 4-membered rings (Fig. 1b), different from the CS correlating distance found at 3.64 Å. This represents a clear improvement with respect to previous force-fields [32] using only Eq. (1) as it led to a structure without ES units. The presence of the additional 3-body interaction obviously forces, indeed, the atoms the adopt configurations with shorter Si–S–Si angles which induce the presence of cyclic structures (rings), as discussed below.

The distance d_{S-S} which defines the edge of the $SiS_{4/2}$ is determined at 3.61 Å (Fig. 9c) and is fully consistent with the distance of 3.65 Å which corresponds to the secondary principal peak of the total experimental [87] function $g_X(r)$ (Fig. 8), the latter resulting from different partial contributions (S–S, Na–Na, Si–Na). The corresponding tetrahedral parameter [88] defined by d_{Si-S}/d_{S-S} is, indeed, found to be equal to 0.58, i.e. very close to the value for a perfect tetrahedra ($\sqrt{3/8}$=0.61). Other typical distances such as d_{Na-S}=3.0 Å are those expected from *ab initio* simulations in the glassy state [87] (see below the partial correlations in Fig. 9) or from the typical distances between a NBS atom and a Na ion in the corresponding crystalline phases [78,84] (Table 4). The main difference with the *ab initio* result [87] is detected in the $g_{SiSi}(r)$ pair correlation function (Fig. 9a) as DFT suggests the presence of homopolar Si–Si bonds at a distance of 2.37 Å which are not recovered with the BM3PM model. Such bonds are observed in certain chalcogenide network formers [89] but not [90,91] in SiS_2. Once modified by an alkali modifier, we are only aware that such bonds are present [85,86] in crystalline $Na_6Si_2S_6$, although there is some evidence [48] that these might be present as well in highly depolymerized sodium thiosilicates containing between 50 and 66 % Na_2S.

3.1.3. The role of 3-body BS potentials

The most serious drawback of previous approaches [30,31] is the near complete absence of the first sharp diffraction peak (Fig. 6c), and our results indicate that it is linked with the utility of a 3-body interaction [92] which constrains the Si–S–Si angle involving a BS atom. Fig. 10 highlights the effect of this 3-body term (Eq. (2)) on the small k-region of the structure factor $S_X(k)$, and on the corresponding

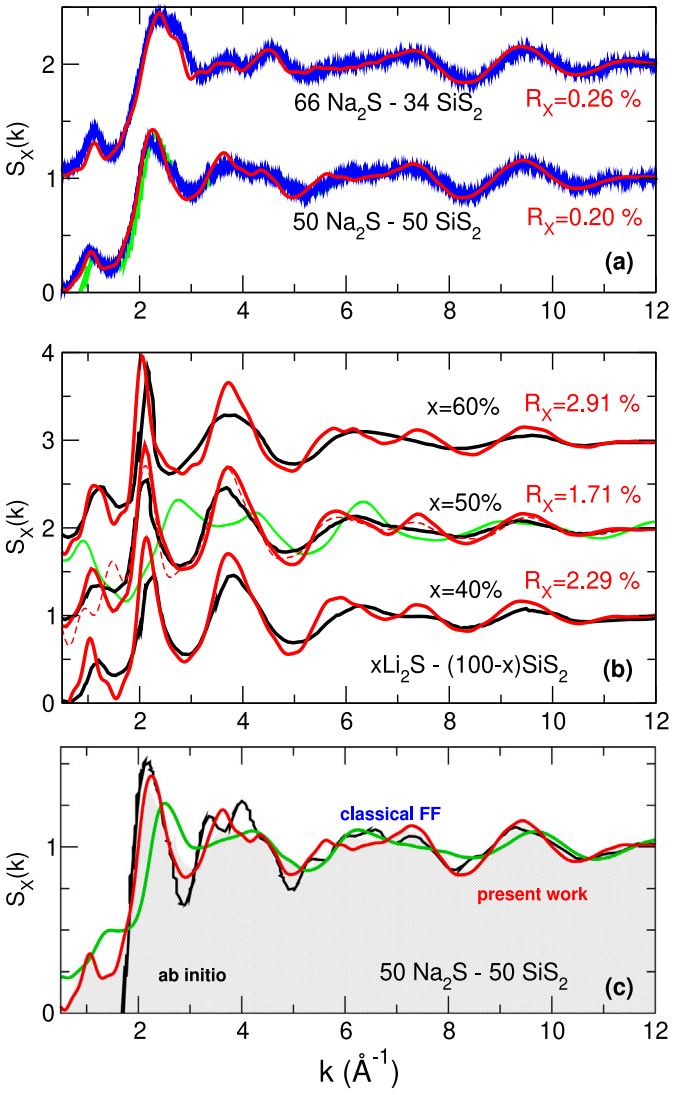

Fig. 6. Calculated X-ray weighted total structure factor $S_X(k)$ (red curves) obtained from the BM3PM model in glassy alkali thiosilicates : (100-x)SiS_2 – $x$$Na_2S$ (a), and (100-x)SiS_2 – $x$$Li_2S$ with different compositions x (b), and compared to experimental data from X-ray scattering on Na (blue [87] and green [30]) and Li-based glasses [7,11] (black) including a result (green curve) from a previous force field for 50SiS_2–50Li_2S [16]. The broken red curve for 50Li_2S – 50SiS_2 is also a result from a recent force-field using only a 2-body potential [32]. Wright parameters R_X are indicated in each panel. (c) Comparison of calculated structure factors $S_X(k)$ obtained from different molecular dynamics modeling schemes applied to the sodium thiosilicate 50SiS_2 – 50Na_2S: red curve (present work, same as panel a) compared to a recent classical potential [31] (green) and ab initio calculations [30] (black). The gray shaded zone corresponds to the experimental [87] $S_X(k)$ (same as panel a).

Si–S–Si bond angle distribution (BAD). For k_b=0 (absence of angular interaction), our results are of the same quality at low k as those previously reported [30,31]. Although we fairly reproduce with k_b=0 the global pattern of the function $S_X(k)$ over extended ranges in k (not shown), the FSDP reduces only to a shoulder peak (at 1.5 Å^{-1}, experimentally [87] 1.04 Å^{-1}) of the principal peak found at 2.5 Å^{-1} (black curve, Figs. 10a and b). We, furthermore, note that in absence of a 3-body potential, the Si–S–Si BAD essentially mimics the one obtained in corresponding sodium silicate glasses [93] which consists in a broad distribution centered at ≃140° (k_b=0, black curves in Figs. 10c, and d). These features are not consistent with the documented structure

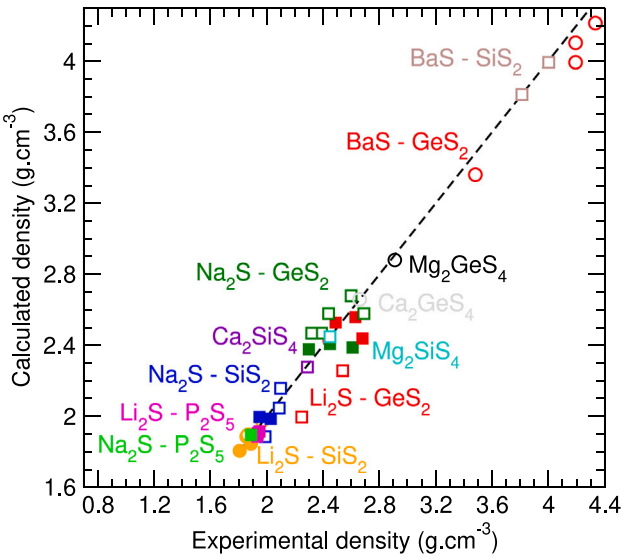

Fig. 7. Calculated densities versus measured densities ρ_0 in various sulfide glasses using the BM3PM model. Open and filled symbols correspond to crystalline and glassy compositions, respectively. The BaS-GeS_2 polymorphs are represented by open red circles. Details are provided in corresponding tables or in text.

of chalcogenides made of both ES and CS tetrahedra (Fig. 1b). As a result, Si–S–Si BADs should display a bimodal distribution representing both types of connections as in other typical network-forming chalcogenides [28,51,52].

Once the presence of an angular interaction is taken into account via Eq. (2), the effect of both parameters (k_b, θ_0) on the FSDP and the Si–S–Si BAD becomes obvious. Note that the effect of the parameters governing the intra-tetrahedral interaction (S–Si–S) is weak. The choice of θ_0 (100°, Fig. 10d) close to the unconstrained (i.e. k_b=0) value of 140° has little effect upon increasing k_b, and the FSDP region still remains poorly reproduced (Fig. 10b). The average Si–S–Si angle (Fig. 10d) automatically reduces but without inducing the typical contribution associated with ES connections. For the case (θ_0=100°, k_b=1.5), the corresponding ES statistics estimated from the King algorithm [94] (see below) yields a fraction of zero ES tetrahedra, still in obvious disagreement with experimental estimates from NMR [44]. A drastic reduction of θ_0 down to 0° now leads to a clear bimodal BAD with increasing k_b, and the convergence criteria based on the Wright parameter fixes the best set of angular force-field parameters to k_b=0.8 (Table 2). At a first glance, one might argue that the choice of θ_0=0 could lead to an unphysical and acute Si–S–Si angle at low angle θ but such a situation would lead to a strong repulsion arising from the S–S 2-body interaction of Eq. (1). The interplay between the angular penalty when $\theta_0 \neq 0$ and the repulsive $V_{SS}(r)$ interaction at short distance finally leads to an excellent reproduction of the FSDP region (position, width, intensity) and produces an ES:CS ratio of 40:60 in 50SiS_2 – 50Na_2S that is compatible with the experimental determination from NMR [44].

These conclusions on the utility of an angular interaction are actually in line with recent ones formulated by Bertani et al. [64] for a large family of silicates, aluminosilicate and phosphate crystals, and multicomponent oxide glasses. The inclusion of three-body interactions T-O-T (T=Si,P) for the bridging oxygen atoms between polyhedra leads, indeed, to an improved bond angle and more realistic Q^n distributions, and to an increased agreement with experimental properties on structure: network former-oxygen distances, densities, structure functions $g(r)$ and $S(k)$. Our conclusions hold to some extent also to the SiS_2-Li_2S system discussed in the following, and one remarks that a simple Born–Mayer 2-body interaction [32] also leads to a poor description of

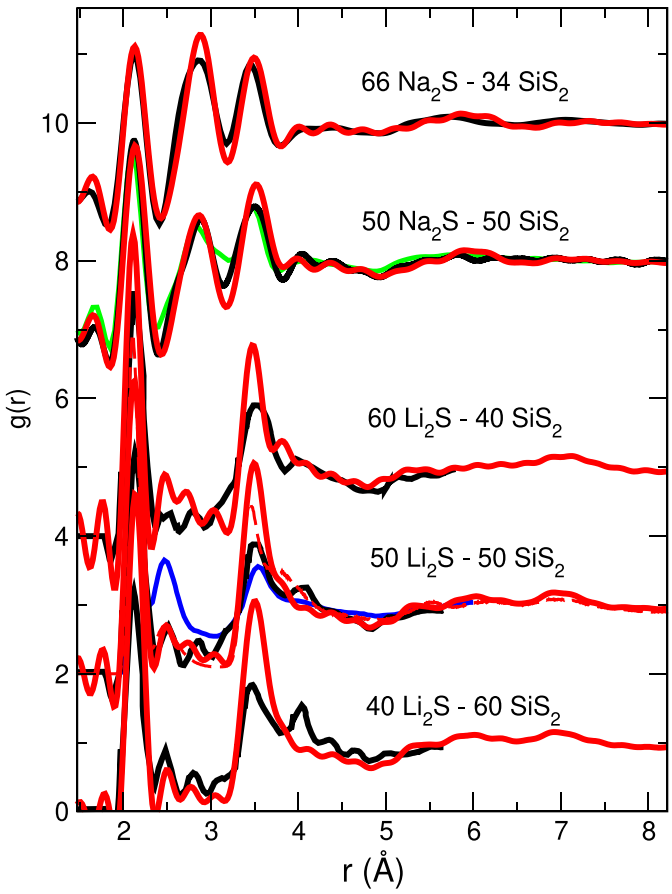

Fig. 8. Calculated pair correlation function $g(r)$ (red) in $34SiS_2$ – $66Na_2S$ (N2S) and $50SiS_2$ – $50Na_2S$ (NS) glasses, compared to the experimental counterpart (black [87]) and to a Fourier transform of an experimental $S_X(k)$ (green [30]) for NS. The calculated $g(r)$ (red) are also shown for different compositions in $(100\text{-}x)SiS_2$–xLi_2S glasses for different Li content x, and compared to experimental counterparts [7] (black curves, digitized), to the result of a recent force-field using only a 2-body potential [32] (broken red curve), and to a ML based potential [36] (blue curve).

the FSDP region (broken red curve or green curve in Fig. 6b), whereas an explicit account of the 3-body interaction via Eq. (2) now permits to reproduce the pattern for all considered compositions (solid red curves).

3.2. SiS_2-Li_2s glasses and crystals

The second considered material is the lithium thiosilicate of the form $(1\text{-}x)SiS_2$ – xLi_2S that has just been mentioned. Four different crystalline polymorphs have been reported in the literature.

3.2.1. Crystalline phases

In this system, two polymorphs with at least two different stabilities and temperatures can be formed: the metathiosilicate Li_2SiS_3, and the orthothiosilicate Li_4SiS_4. The former melts uniformly at 745 ± 10 °C, and depending on the cooling conditions after the melting temperature, two distinct phases can be formed: equilibrium (e-Li_2SiS_3), metastable crystalline (m-Li_2SiS_3 with a melting temperature of T_m=1018 K [95]). The structure of the crystals is made of corner-sharing tetrahedra using Q^2 units with the NBS in the vicinity of Li ions, and which form a one-dimensional chain structure *via* the BS atoms connecting two close $SiS_{4/2}$ tetrahedra together [53,82]. Although e-Li_2SiS_3 and m-Li_2SiS_3 have been studied by ^{29}Si NMR [44], the crystallographic data of the former are only conjectured [95], and result from a simulated X-ray powder measurement using the appropriately rescaled atomic coordinates of the isochemical Li_2SiO_3. NMR only indicates that the structure of e-Li_2SiS_3 might differ from m-Li_2SiS_3 with the possible presence of ES $SiS_{4/2}$ tetrahedra [44]. However, the exact atomic coordinates of the "true" phase being unknown, we test the performance of the force-field on the isochemical model [95] proposed from Li_2SiO_3, as we realized previously [32].

Table 5
Experimental cell parameters, system density (n_0, ρ_0) and main distances of different lithium thiosilicate crystals, compared to the present calculated values from the BM3PM model in NPT Ensemble at zero pressure, and 100 K. The number N of particles is indicated for each compound.

	Expt.	Model
e-Li_2SiS_3		N=**3000**
a (Å)	11.66 [95]	11.64
b (Å)	6.74 [95]	6.72
c (Å)	5.93 [95]	5.92
n_0 (Å^{-3})	0.052 [95]	0.052
ρ_0 (g cm^{-3})	1.97 [95]	1.98
d_{Si-S} (Å)	2.09	2.05
d_{S-S} (Å)	3.36	3.48
d_{Li-S} (Å)	2.46	2.44
m-Li_2SiS_3	P_1	N=**3000**
a (Å)	11.44 [82]	11.38
b (Å)	6.61 [82]	6.57
c (Å)	6.49 [82]	6.45
n_0 (Å^{-3})	0.0490 [82]	0.050
ρ_0 (g cm^{-3})	1.87 [82]	1.90
d_{Si-S} (Å)	2.09	2.08
d_{S-S} (Å)	3.36	3.48
d_{Li-S} (Å)	2.46	2.45
LT-Li_4SiS_4	$Pnma$	**N=2304**
a (Å)	13.78 [97]	13.70
b (Å)	7.77 [97]	7.73
c (Å)	6.14 [97]	6.11
n_0 (Å^{-3})	0.054 [97]	0.055
ρ_0 (g cm^{-3})	1.86 [97]	1.89
d_{Si-S} (Å)	2.09	2.05
d_{Li-S} (Å)	2.46	2.52
HT-Li_4SiS_4	$P2_1/m$	**N=2304**
a (Å)	6.89 [97]	6.86
b (Å)	7.77 [97]	7.73
c (Å)	6.13 [97]	6.10
n_0 (Å^{-3})	0.054 [97]	0.055
ρ_0 (g cm^{-3})	1.86 [97]	1.89
d_{Si-S} (Å)	2.15	2.09
d_{Li-S} (Å)	2.35	2.48

e-Li_2SiS_3 is usually obtained upon rapid cooling to 993 K with subsequent annealing at the same temperature [53,82], and forms [95] with lattice parameters a=11.66 Å, b=6.74 Å, and c=5.93 Å. We succeed in reproducing such data within NPT at zero pressure, and find a=11.64 Å, b=6.73 Å, and c=5.92 Å (Table 5), and a similar density (1.98 g cm^{-3} against the experimental [95] value 1.97 g cm^{-3}). The same encouraging conclusions are maintained for the metastable crystalline m-Li_2SiS_3, and we find, indeed, crystallographic parameters at zero pressure which are close to their experimental counterparts (e.g. b=6.61 Å [82] against our computed 6.57 Å). As the lattice parameters are somewhat larger, the resulting calculated density is increased (1.90 g cm^{-3}) with respect to experiment (1.87 g cm^{-3}).

The second polymorph which crystallize [53,95,96] in the SiS_2 – Li_2S binary forms at 66 %Li_2S and exists as a high (HT) and low-temperature (LT) form [97,98] with slightly different crystallographic parameters (Table 5). Here again, the obtained parameters in Eqs. (1) and (2) lead to crystallographic data that are consistent with those determined from X-ray scattering, i.e. for LT-Li_4SiS_4, we find at zero pressure a cell length a=13.70 Å to be compared with the experimental [97] value of 13.78 Å, the other cell parameters being reproduced in a similar

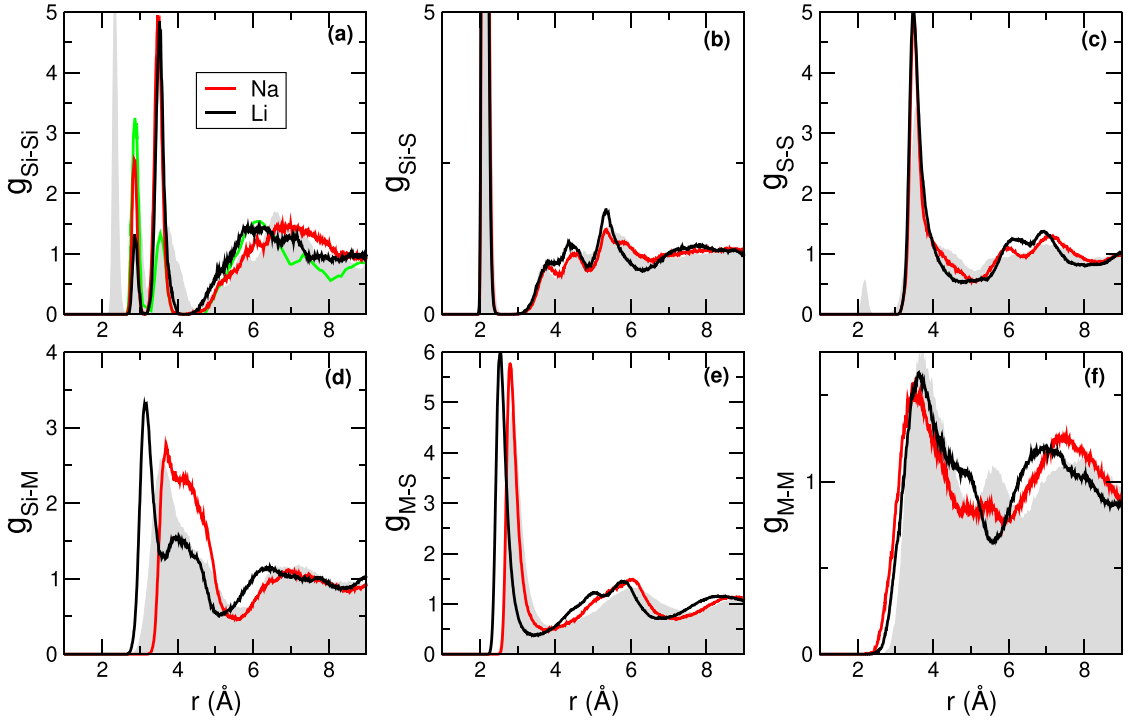

Fig. 9. Calculated partial pair correlation functions $g_{ij}(r)$ in 50 SiS_2–50M_2S with M=Li (black) and M=Na (red). The green curve in panel (a) corresponds to a calculation using a ML force field [36] for the Li glass. The gray areas in the back are the DFT results [87] on 50SiS_2–50Na_2S.

way. Corresponding calculated interatomic distances are compatible with experimental determination, and we found 2.05 Å and 2.52 Å for the Si–S distance, and Li-S distance, respectively. These values are close, indeed, to those determined from X-ray measurements [97]. Regarding HT-Li_4SiS_4, the same level of agreement is achieved, and the resulting density is somewhat increased (1.89 g cm^{-3}) with respect to the experimental counterpart (1.86 g cm^{-3}) which results from a small expansion of the simulation box at zero pressure.

3.2.2. Lithium thiosilicate glasses

Using the fitted parameters of the force-field, we have simulated three compositions in the (1-x)SiS_2 – $x$$Li_2S$ system (x=40, 50 and 60 %) because of available X-ray scattering measurements [7,11] at such compositions. We, therefore, can compare our calculated structure factors $S_X(k)$ (Fig. 6b) and pair correlation functions (Fig. 8) with their experimental counterparts. A certain comments can be made.

First, we obtain glass densities at 300 K during the zero temperature quench which are identical to the measured experimental values (Fig. 7), i.e. we found ρ_g=1.83, 1.80, and 1.90 g cm^{-3} for 40, 50 and 60 % Li_2S, respectively. Regarding the structure functions (Fig. 6b), and when these are compared to the sodium analogue discussed above, we first note that the agreement in reciprocal space is lower in the Li systems, although the model is able to reproduce all main features of the diffraction pattern such as principal peak positions (2.14 Å^{-1}, 3.73 Å^{-1}) and widths, the intensities being overestimated, however. Most noticeable is the clear improvement brought by the 3-body interaction which is now able to correctly describe the FSDP region (1.15 Å^{-1}) when compared to previous simulation efforts [16,32] (broken red and green curves in Fig. 6b).

In real space (Fig. 8), we find a rather good agreement with the corresponding measured functions [7] for all considered compositions, the pair correlation function $g(r)$ being dominated by Si–S bond distance found at 2.18 Å and by a secondary peak at 3.6 Å which results from different contributions: S–S, Si–Si involved in CS tetrahedra, and Li-Li correlations (Fig. 9). Note that due to the weak contribution of Li in such weighted X-ray pair correlation functions, in contrast to the Na analogue no typical peak emerges at a distance somewhat lower than 3.0 Å in the total pair correlation function (Fig. 8). Partial correlations (Fig. 9) indicate a similar structure with the Na-based systems, i.e. the network is dominated by $SiS_{4/2}$ tetrahedra having a well defined apex distance (Si–S) and S–S edge (Fig. 9b and c). The partial Si–Si correlation leads to the same structural pattern with the presence of both ES and CS typical bond distances (Fig. 9a). The alkali-related partials display the same profile as Na-based glasses, albeit shifted in position, and these small differences result from the different cation size and the different system density (1.90 g cm^{-3} versus 2.03 g cm^{-3} for Li and Na thiosilicates, respectively).

3.2.3. Comparison with previous force-fields

We remind that a force-field has been recently established [32] which contains only a two-body interaction (Eq. (1)). It has clearly improved the description of SiS_2 – Li_2S glasses with respect to earlier attempts [16] (green curve in Fig. 6b), and has been able to improve the reproduction of the structure functions accessed from X-ray scattering (broken curve in Fig. 6). However, the main drawback of this earlier effort is (i) the poor reproduction of the FSDP region, and (ii) the complete absence of ES structures although they have been detected from NMR experiment thanks to the identification of the different chemical shifts associated with the E^k functions (Fig. 1, and discussion below). The present parametrization, thus, represents a clear improvement in this respect because the inclusion of Eq. (2) now leads to a finite ES fraction in the 50SiS_2 – 50Li_2S glass, as also detected from the typical ES peak in the Si–Si partial (Fig. 9a). Numbers are provided from the statistical ring analysis in the dedicated section.

A recent ML model has been reported, and is based on a set of trained DFT data [36]. This model is able to correctly predict the main structural features of the 50SiS_2–50Li_2S glass but fails to reproduce correctly the pair correlation function $g(r)$ as certain overestimated atomic correlations lead to a spurious peak at about 2.6 Å (blue curve in Fig. 8) which is not observed experimentally. Despite this obvious drawback, the ML description can be clearly seen as an improvement with respect to Refs. [16,32] because the resulting ML based structure

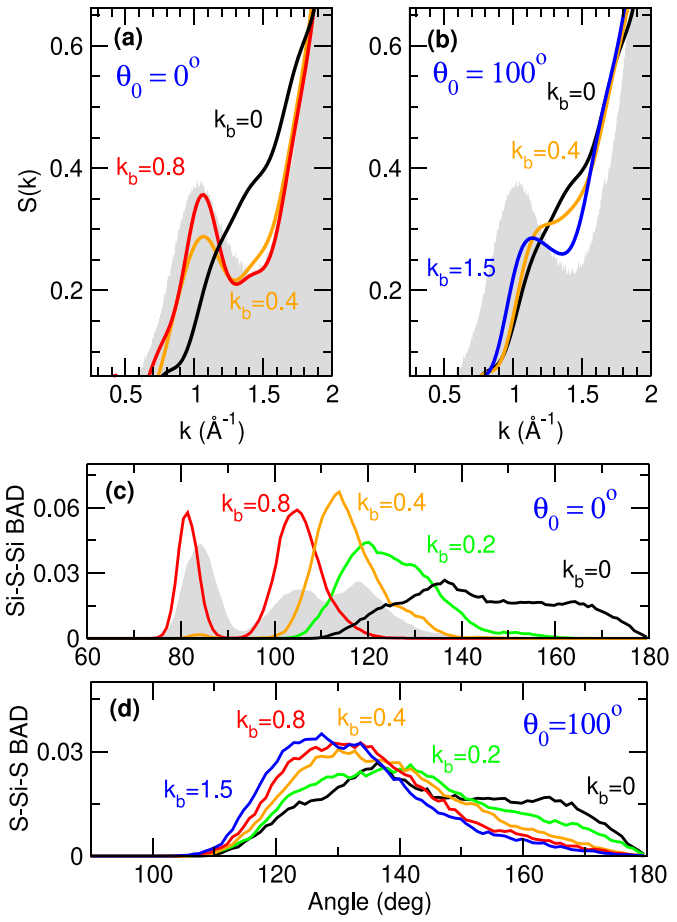

Fig. 10. Effect of the 3-body interaction parameter k_b on the structure factor and the FSDP region in Na_2S – SiS_2 (NS) glasses for θ_0=0° (a) and θ_0=100° (b): k_b=0.8 eV deg^{-2} (red, panel a is the same as Fig. 6a), k_b=0.4 (orange), k_b=0 (black), and k_b=1.5 (blue, panel b). The gray area represents the experimental [30] $S_X(k)$. (c) and (d): Bond angle Si–S–Si distribution for corresponding (k_b) parameters at fixed angle θ_0. The curves k_b=0 are identical in panels c and d, and panels a and b. The gray area in panel c corresponds to a calculation from DFT-MD [87].

contains a certain number of ES motifs which are compatible with experimental observation from NMR. Thanks to the addition of Eq. (2) which constrains the angular Si–S–S interaction and also leads to ES motifs, our present parametrization is now able to compete with the ML technique, the added value being its ease of implementation, and the improved description of the real space properties (Fig. 8).

3.3. Alkaline earth thiosilicates

While a certain but limited number of crystalline polymorphs of alkaline earth thiosilicates have been characterized and investigated, we are not aware of any study of the amorphous phases, and the glass-forming region of these systems is, therefore, unknown. Mg [99], Ca [99] and Ba thiosilicate crystals [100–102] form essentially in the ratio MS:SiS_2 of 2:1, and lead to crystals such as Mg_2SiS_4 which is of olivine type [103] in *Pnma* symmetry (Table 6). Using the parameters of the BM3PM model, the reported phases have been simulated. In NVT ensemble, results lead to residual pressures at 100 K which are less than 0.5 GPa (0.5 GPa in Mg_2SiS_4, −0.1 GPa in Ca_2SiS_4 or 0.1 GPa in Ba_2SiS_4) while simulations in NPT at zero pressure lead to system densities which are very close to the reported values from experiment, e.g. 2.43 g cm^{-3} in Mg_2SiS_4, compared to the experimental value [99] of 2.45 g cm^{-3} (see also Fig. 7). Simulations furthermore suggest

Table 6
Experimental cell parameters, system density (n_0, ρ_0) and main distances of different alkaline earth thiosilicate crystals, compared to calculated values from the BM3PM model in NPT Ensemble at zero pressure, and 100 K. The number N of particles is indicated for each compound.

	Expt.	Model
Mg_2SiS_4	*Pnma*	N=**2880**
a (Å)	12.64 [99]	12.70
b (Å)	7.47 [99]	7.43
c (Å)	5.92 [99]	5.93
n_0 (Å^{-3})	0.050 [99]	0.050
ρ_0 (g cm^{-3})	2.45 [99]	2.43
d_{Si-S} (Å)		2.11
d_{Mg-S} (Å)		2.54–2.80
Ca_2SiS_4	*Pnma*	N=**5376**
a (Å)	13.49 [99]	13.56
b (Å)	8.18 [99]	8.15
c (Å)	6.21 [99]	6.18
n_0 (Å^{-3})	0.041 [99]	0.041
ρ_0 (g cm^{-3})	2.29 [99]	2.30
d_{Si-S} (Å)	2.04 [99]	2.12
d_{Ca-S} (Å)	2.81–2.89 [99]	2.80
Ba_2SiS_4	*Pnma*	N=**5376**
a (Å)	8.92–8.93 [100,101]	8.99
b (Å)	6.78–6.79 [100,101]	6.83
c (Å)	12.01–12.03 [100,101]	12.26
n_0 (Å^{-3})	0.037 [100,101]	0.037
ρ_0 (g cm^{-3})	3.81 [101]	3.81
d_{Si-S} (Å)	2.10 [101], 2.17 [100]	2.10
d_{Ba-S} (Å)	2.82 [101]	3.25
d_{Ba-Ba} (Å)	4.43 [101]	4.20–4.80
Ba_3SiS_5	*Pnma*	N=**4320**
a (Å)	12.12 [102]	12.09
b (Å)	9.53 [102]	9.54
c (Å)	8.55 [102]	8.66
n_0 (Å^{-3})	0.036 [102]	0.036
ρ_0 (g cm^{-3})	3.99 [102]	3.99
d_{Si-S} (Å)	2.14–2.18 [102]	2.08
d_{Ba-S} (Å)	3.07–3.25 [102]	3.14–3.31

a rather constant bond length for the apex of the $SiS_{4/2}$ tetrahedra (2.08–2.12 Å) which is compatible with the experimental findings, the other characteristic distances (M-S with M=Mg, Ca, Ba) being close to the simulated values (e.g. d_{Mg-S}=2.45 Å [99] to be compared with the calculated 2.43 Å, Table 6). With increasing alkaline earth size, we furthermore note increasing bond lengths as in experiment (Table 6). Two other phases in the CaS–SiS_2 binary have been reported [103], $CaSi_2S_5$ and $CaSiS_3$, but their structure is unknown. The latter compound is thought to belong to the family of chalcogenide perovskites, and its structure has been recently conjectured (orthorhombic structure with *Pnma* symmetry) from DFT calculations [104].

In Fig. 11 we report the X-ray weighted pair correlation functions $g(r)$ of corresponding alkaline earth thiosilicate glasses (SiS_2 – 2MS with M=Mg, Ca, Ba, and 3BaS–SiS_2) for which experimental X-ray scattering data is apparently not available. The present results highlight the dominant role played in all systems by the three bond distances Si–S, M–S, and S–S. The first one leads to the principal peak at 2.11 Å (as in alkali thiosilicates) whose intensity decreases with increasing ion size, from Mg to Ba. The secondary distance produces a peak that emerges at some larger distance r, and its location strongly depends on the weight of alkaline earth ion, i.e. we find the Mg–S, Ca–S, and Ba–S bond distances at 2.41 Å, 2.78 Å, and 3.23 Å, respectively. The third peak at larger distances (e.g. 3.49 Å for the Mg glass) is related with S–S bonds as already identified in corresponding alkali thiosilicates (Fig. 9c). This distance reduces in the Ca glass (2.51 Å), and merges as a high r-tail of the Ba-S secondary peak (3.25 Å) in the barium glass.

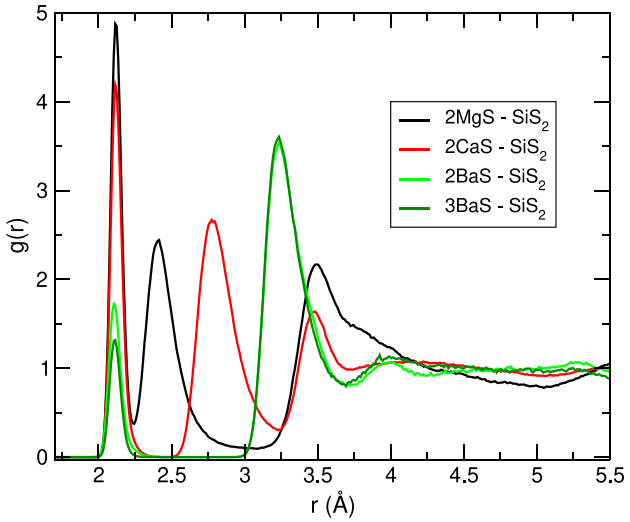

Fig. 11. Calculated X-ray weighted pair correlation function $g(r)$ in SiS_2 – MS (M=Mg, Ca, Ba), and 3BaS – SiS_2 glasses.

3.4. GeS_2-Na_2S glasses and crystals

A certain number of crystalline phases form in the GeS_2 – Na_2S binary whose phase diagram has been characterized by different authors [79,105], and seems to display a tendency to phase separation [106] at small Na_2S content as in low modified alkali silicates [107]. Four polymorphs have been identified, $Na_2Ge_2S_5$, Na_2GeS_3, $Na_6Ge_2S_7$, and Na_4GeS_4 (Table 7), for which the BM3PM model has been tested as well. Regarding the glassy phase, early experimental studies [108–110] have shown that Na_2S can be added to the base network former GeS_2 from 0 up to 60 % by melt quenching technique, forming stable glasses with glass transition temperatures between 250–280 °C. The structure has been characterized by various methods including spectroscopic ones [109,111,112], X-ray and neutron scattering [18,113,114], and the GFD now extended [18] to 66 % Na_2S.

We represent in Fig. 12 the calculated structure factor $S(k)$ (panel a) and pair correlation function (panel b) of different glass composition of this GeS_2 – Na_2S binary which shows, once again, an excellent agreement of the BM3PM model with respect to the available experimental measurements from neutron [114] or X-ray scattering [18,113]. The agreement is of unprecedented accuracy (R_X ≃0.5%) in reciprocal space for high and low modifier content, i.e. $33GeS_2$ – $67Na_2S$ (N2G) and $67GeS_2$ – $33Na_2S$ (NG2) to a lesser extent (wavevector region around 2.5 $Å^{-1}$), with a near complete superposition of both the theory and the experimental curves over the entire wavevector range including the FDSDP region. We note that the agreement with experiment [114] is more reduced (R_X ≃0.82%) for the $50GeS_2$ – $50Na_2S$ (NG) composition for reasons which are not fully understood, although the calculated density agrees with the experimental values (Fig. 7).

In real space, we also find an excellent agreement with the measured pair correlation function (Fig. 12b) for all composition, the principal peak found at 2.20 Å being reproduced in position, width and intensity for all compositions. Secondary peaks at r ≃3.05 Å and 3.75 Å are also obtained, and clearly evolve with composition in intensity, the growing presence of Na atoms leading the emergence and growth of a typical peak associated with the Na-S bond distance at 2.80 Å which is especially visible for the $33GeS_2$–$67Na_2S$ composition (Fig. 12b). On the other hand, the secondary peak (3.60 Å) reminiscent of the base network structure GeS_2 is partly related to CS Ge–Ge correlations which progressively vanish upon network depolymerization (i.e. x=66 %, Fig. 13d). The detail of the partial pair correlations permits to support these observations which are also made on an experimental basis [87,114], and to infer the origin of the observed structural changes driven by Na_2S content.

Table 7
Experimental cell parameters (in Å), system density (n_0, ρ_0) and main distances of different sodium thiogermanate crystals, compared to calculated values from the BM3PM model in NPT Ensemble at zero pressure, and 100 K.

	Expt.	Model
$Na_2Ge_2S_5$	*Cmcm*	**N=4608**
a (Å)	12.85 [78,115]	13.02
b (Å)	12.90 [78]	13.08
c (Å)	10.48 [78]	10.62
n_0 ($Å^{-3}$)	0.041 [115]	0.040
ρ_0 (g cm^{-3})	2.69 [115]	2.58
d_{Ge-S} (Å)	2.14–2.20 [78]	2.23
d_{Na-S} (Å)	2.87–2.92 [78]	2.81
Na_2GeS_3	$P12_1/c1$	**N=3000**
a (Å)	6.95 [116]	6.90
b (Å)	15.23 [116]	15.11
c (Å)	5.72 [116]	5.67
n_0 ($Å^{-3}$)	0.044 [116]	0.045
ρ_0 (g cm^{-3})	2.60 [117]	2.68
d_{Ge-S} (Å)	2.04 [116]	2.15
d_{Na-S} (Å)	2.83 [116]	2.83
$Na_6Ge_2S_7$	$C12/c1$	**N=3840**
a (Å)	9.09 [116,118]	8.93
b (Å)	10.44 [116,118]	10.25
c (Å)	15.46 [116,118]	15.18
n_0 ($Å^{-3}$)	0.043 [116,118]	0.046
ρ_0 (g cm^{-3})	2.44 [116,118]	2.58
d_{Ge-S} (Å)	2.19 [118]	2.19
d_{Na-S} (Å)	2.83 [116]	2.77
Na_4GeS_4	*Im*	**N=2160**
a (Å)	19.81 [117], 20.04 [119]	21.51
b (Å)	29.25 [117], 29.65 [119]	29.03
c (Å)	10.96 [117], 10.98 [119]	9.81
n_0 ($Å^{-3}$)	0.047 [119]	0.046
ρ_0 (g cm^{-3})	2.39 [117], 2.32 [119]	2.47
d_{Ge-S} (Å)	2.19–2.25 [119]	2.19
d_{Na-S} (Å)	2.78–2.83 [119]	2.76

As already mentioned, the structure of sodium thiogermanate glasses is dominated by the $GeS_{4/2}$ tetrahedra which lead to prominent peaks in S–S and Ge–S partials (Figs. 13a and b), whereas their underlying connectedness is revealed from the Ge–Ge partial (Fig. 13d). Here, one acknowledges as for other modified sulfides discussed above, the presence of two principal peaks at 3.05 Å and 3.75 Å which are associated with ES and CS tetrahedral connections, respectively. With growing Na_2S concentration, such peaks evolve and result from the reduction of network polymerization and ring structures. It also leads to the emergence of typical Ge–Na distances which are associated with Ge–NBS–Na triplets, whereas the typical distance Na–Na (3.99 Å for NG2 and 3.62 Å for N2G, Fig. 13f) tends to reduce due to the larger number of Na atoms at elevated Na_2S content.

Again, an inspection of the role of the modifier content indicates that in such sodium thiogermanates, the addition of sodium preserves the tetrahedral character of the base $GeS_{4/2}$ geometry since we find that the tetrahedral parameter [88] defined by $\delta = d_{Ge-S}/d_{S-S}$ is equal to its expected value of $\sqrt{3/8}$ for all compositions, i.e. we find δ=0.62(9), 0.60(3) and 0.60(6) for the compositions at 33 %, 50 % and 66 %, respectively.

3.4.1. Comparison with ab initio results

It is again instructive to compare the classical MD results accumulated for sodium thiogermanates with corresponding results [18] based on DFT simulations, as we did for sodium thiosilicates in Section 3.1.2. Fig. 13 compares the partial pair correlation functions of NG2, NG and N2G with similar results from DFT simulations reported recently [18] for N2G. We, thus, verify that our obtained structures are compatible

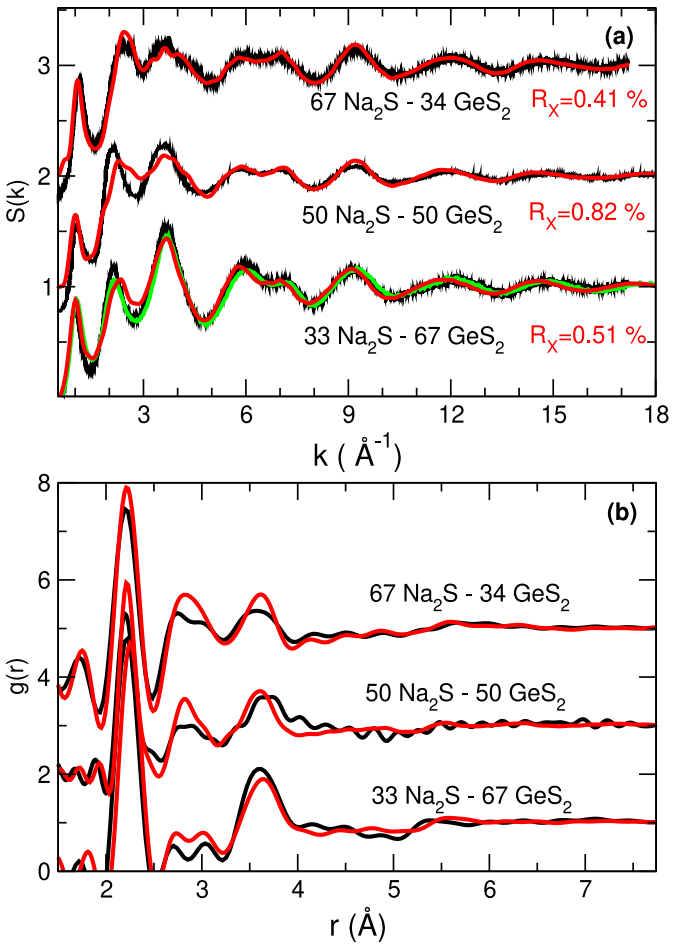

Fig. 12. Calculated (red) structure factors $S(k)$ (a) and pair correlation functions $g(r)$ (b) of different sodium thiogermanates of the form (100-x)GeS_2 – xNa_2S, and compared to experimental data from X-ray and neutron scattering: NG2 (X-ray, green [113] and black [18]), N2G (X-ray, black [18]) and NG (neutron, black [114]). Wright parameters R_X are indicated in panel a.

with such previous results obtained from *ab initio* simulations (gray zones in Fig. 13) which provides an additional strength to the BM3PM model although some differences appear in second shell correlations as highlighted in the S–S (panel a), Na–S (panel c) and Ge–Na partial pair correlation functions (panel e). Specifically, in the first shell of coordination we find that dominant peaks corresponding to d_{Ge-S}=2.20 Å, d_{SS}=3.61 Å and d_{NaS}=2.87 Å are identical to those found in the DFT results. We also note that the two-peak pattern in the Ge–Ge partial (Fig. 13d) identified with ES and CS motifs is also recovered. Finally, the DFT simulations leads to the presence of a small number of homopolar S–S defects (Fig. 13a) detected at $r \simeq$2.20 Å which are reminiscent of the base GeS_2 glass [28]. Upon modifier content increase, the structure leads to a breakdown of ES motifs which manifests by a strong reduction of the ES peak in the Ge–Ge partial pair correlation function, consistently with the enumeration of rings indicative of their absence in N2G as a result from the increased depolymerization and the massive presence of NBS atoms that rule out the possibility of having closed loops (rings).

3.4.2. Crystalline sodium thiogermanates

The simulation of the different crystalline polymorphs also indicates a certain stability at ambient conditions, and calculated cell lengths or densities (Fig. 7 or Table 7) are of the same order as those determined experimentally, e.g. we find differences in density of about 5–6 % for $Na_6Ge_2S_7$ with the predicted ρ_0=2.58 g cm^{-3} to be compared to the measured [116] value of 2.44 g cm^{-3}. A calculation of the residual pressure (performed in NVT Ensemble) indicates that P is about or less than 1.0 GPa (e.g. 0.8 GPa for $Na_2Ge_2S_5$ or −1.1 GPa for Na_2GeS_3). All typical distances determined from the crystallographic data are recovered, and the shortest distances are those corresponding to Ge–S (2.04–2.25 Å) and Na–S bonds (2.78–2.92 Å).

3.5. GeS_2-Li_2S glasses and crystals

We now focus on the lithium counterpart of Na thiogermanates, and discuss once again the validity of the BM3PM on another important class of solid electrolytes which have been investigated as thin films [120], and serve also as base material for the LGPS electrolyte.

Three crystalline phases can be formed in the GeS_2–Li_2S system: Li_2GeS_3, Li_4GeS_4 and Li_8GeS_6, the latter being unstable because of phase transformation at low temperature [121]. It has been investigated recently from *ab initio* simulations [122] but we are not aware of any experiments regarding the crystallographic data. We describe the two documented compounds [123–127] below, but focus first on the glassy state.

3.5.1. Lithium thiogermanate glasses

Fig. 14a represents the calculated X-ray weighted structure factors $S_X(k)$ for different composition x in (100-x)GeS_2 – xLi_2S glasses. Here, the agreement with experimental data [17] is excellent, and all features are reproduced in terms of peak locations, widths and intensities over a broad range of compositions ranging from 20 % to 50 % Li_2S, and the difference of the FSDP region between experiment and simulation at 50Li_2S – 50GeS_2 is barely visible, and leads to a Wright parameter R_X in the range 0.40–0.70%. Upon modifier increase, the experimental location [17] of the FSDP shifts with composition (from k_{FSDP}=1.05 Å^{-1} to 1.08 Å^{-1}), and we also reproduce this trend (from 1.05 Å^{-1} to 1.11 Å^{-1}). For this composition, we also obtain a reduced contrast between the two other principal peak intensities located at 2.12 and 3.67 Å^{-1}, this feature being the only (minor) limitation of the force-field parametrization. Finally, the correctly reproduced oscillations at large k provide a reasonable reproduction in real space. This is acknowledged from corresponding pair correlation function $g(r)$ in real space (Fig. 14b), and we obtain the rather correct location for the principal peak corresponding to the Ge-S distance, albeit slightly overestimated for all compositions, e.g. we find 2.26 Å to be compared to the measured [17] value of 2.22 Å.

As for the other investigated materials, the detail of the partial correlations (Fig. 15) permits to detect the typical bond distances in the GeS_2 – Li_2S glasses which are dominated by the tetrahedral structure made of the apex Ge–S (Fig. 15b) and the S–S edge at 3.75 Å (Fig. 15a). These values are consistent with an investigation [128] from DFT on a close composition (L2G, 34GeS_2 – 66Li_2S). The latter, furthermore, indicates that upon modifier increase (from 20 % to 66 %), the Li–Li correlating distance (Fig. 15f) reduces substantially, and shifts from 4.30 Å in 80GeS_2 – 20Li_2S to about 3.0 Å for L2G. In terms of compositional effects, we note that the main difference with the DFT results arises from the presence of homopolar Ge–Ge bonds which have been detected [128] for L2G, and are linked with the presence of ethane-like units of the form $Li_6Ge_2S_6$ found in isochemical systems [48] at larger compositions (55–70 %) than those considered here. Similarly, at variance with the DFT glass, we obtain a certain amount of ES tetrahedra as detected from the peak at 3.2 Å in the Ge–Ge partial pair correlation function (Fig. 15d) which do not exist anymore in the highly depolymerized L2G glass [128]. Finally, we remark that the Li–S profile does not seem to depend on composition so that the main changes with the Li content are observable in the vicinity of Ge atoms (Fig. 15e) where a shoulder peak at $\simeq$4.0 Å corresponds to second-shell correlations which are not linked with those involved in Ge–NBS–Li triplets.

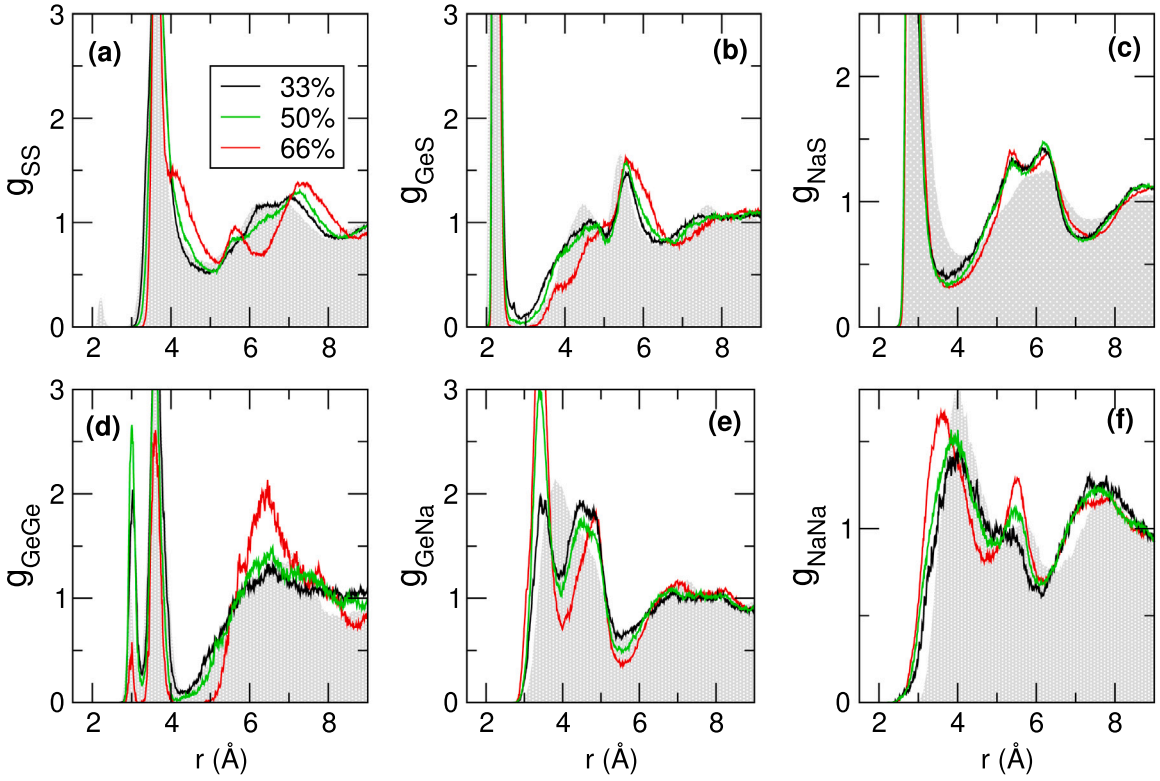

Fig. 13. Calculated partial pair correlation functions $g_{ij}(r)$ for different compositions glassy xGeS$_2$–(100-x)Na$_2$S with x=33 % (NG2, black), 50 % (NG, green) and 66 % (N2G, red). The background functions in gray correspond to a N2G glass obtained from DFT based simulations [18].

3.5.2. Crystalline phases

The crystalline orthorhombic phase Li_2GeS_3 has been studied by different authors [123,124], and has been characterized from XRD and neutron diffraction. The material displays a $P6_1$ symmetry, with lattice parameters a=6.79 Å, and c=17.91 Å (Table 8) and a rather unusual distorted hexagonal close-packed (hcp) wurtzite-like structure in which Ge and certain Li display tetrahedral sites. The former are aligned parallel to the c-axis, forming infinite chains of corner-sharing $GeS_{4/2}$ tetrahedra. Our force-field only partially reproduce the crystallographic data (Table 8), and the most noticeable change is the shift of the typical Li-Li distance (at 3.30 Å in the initial Li_2GeS_3 cell) to larger distances (3.60 Å), this being also detected for the Li-NBS bond distance which grows from the reported [124] 2.34 Å to 2.56 Å in our model. We believe that these differences result from a residual pressure (8.8 GPa calculated at fixed cell length in NVT) that is more elevated than all other previously investigated polymorphs. As a result, the crystallographic data are increased in the NPT simulation, and the density is decreased (2.26 g cm^{-3} versus the experimental [97] 2.54 g cm^{-3}), e.g. we find larger cell lengths (e.g. a=7.07 Å, and b=7.49 Å, Table 8).

The simulation of the Li-rich crystalline compound, Li_4GeS_4, leads to similar conclusions, and the calculated density (2.00 g cm^3) is also the consequence of a residual pressure found at fixed cell lengths. We find, again, an increase of the cell parameters (e.g. b=8.09 Å compared to the experimental [123,125,126] 7.75–7.77 Å) and the typical Li–S bond distance (2.51 Å compared to [125] 2.47 Å).

3.6. Alkaline earth thiogermanates

Similarly to their Silicon counterpart, alkaline earth thiogermanates have been studied several decades ago, and mostly in a series of publications by Ribes' group [77,100,129–131]. In contrast to Ba-based crystals [132,133], it seems that Mg-, and Ca-based polymorphs have not been reconsidered recently.

Table 8
Experimental cell parameters (in Å), system density (n_0, ρ_0), and main distances of different lithium thiogermanate crystals, compared to calculated values from the BM3PM model in NPT Ensemble at zero pressure, and 100 K.

	Expt.	Model
Li_2GeS_3	$P6_1$	**N = 2304**
a (Å)	6.79 [124]	7.07
b (Å)	6.81 [123], 6.79 [124]	7.49
c (Å)	17.95 [123], 17.91 [124]	18.62
n_0 (Å^{-3})	0.050 [124]	0.045
ρ_0 (g cm^{-3})	2.54 [124]	2.26
d_{Ge-S} (Å)	2.17–2.30 [124]	2.15–2.31
d_{Li-S} (Å)	2.34 [124]	2.56
Li_4GeS_4	*Pnma*	**N=2304**
a (Å)	14.00–14.10 [123,125,126]	14.63
b (Å)	7.75–7.77 [123,125,126]	8.09
c (Å)	6.14–6.19 [123,125,126]	6.41
n_0 (Å^{-3})	0.053 [125]	0.047
ρ_0 (g cm^{-3})	2.248 [134], 2.25 [126]	2.00
d_{Ge-S} (Å)	2.17–2.23 [125]	2.21
d_{Li-S} (Å)	2.47 [125]	2.51

A single crystalline phase has been reported for the Mg-Ge-S system (Mg_2GeS_4) whose structure remains stable with the BM3PM model at ambient conditions (Table 9) and crystallographic data are fully consistent with experimental determination [99,130]. The same conclusion holds for the Ca_2GeS_4 crystal (Table 9).

The Ba-Ge-S system has several polymorphs that have been studied decades ago, and now partly reinvestigated from both X-ray diffraction, and DFT calculations [132,133,136]. The low-Ba content polymorph ($BaGe_2S_5$, 33 % modifier) is the less stable crystal of the polymorphs investigated by the BM3PM force-field but is found to maintain the sheet-like structure made of the adamatane-like unit as in Na thiosilicates [79] (Fig. 16). We find at zero pressure a slight distorsion that could result from a small reduction of the system density (from 3.48

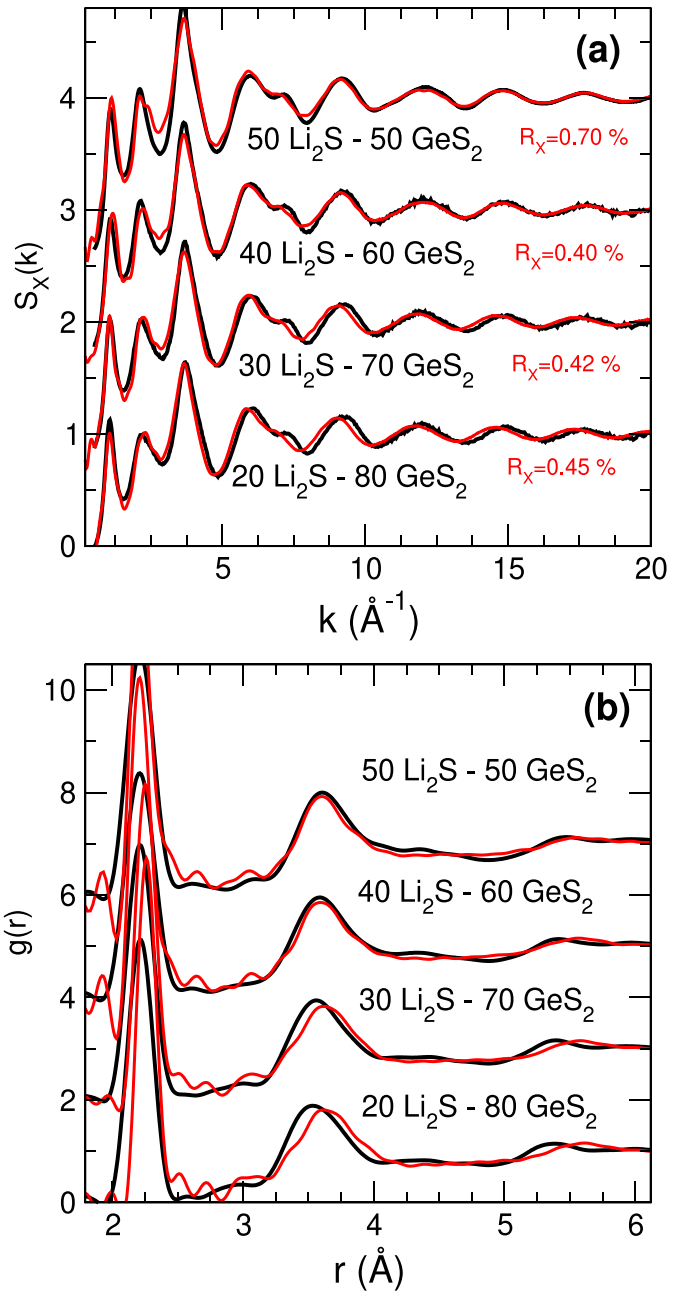

Fig. 14. Calculated (red) X-ray weighted structure factors $S_X(k)$ (a) and pair correlation functions $g(r)$ (b) of different lithium thiogermanates of the form (100-x)GeS_2 – xLi_2S, and compared to experimental data (black) from X-ray scattering [17]. Wright parameters R_X are indicated in panel a.

to 3.36 g cm^{-3}) but typical distances are preserved (e.g. d_{BaS}=3.28 Å against the experimental [78] 3.22 Å, Table 9).

The properties of corresponding glasses are displayed in Fig. 17 which represents the X-ray weighted pair correlation function $g(r)$ for different compositions. The structure is, as previously, dominated by the apex distance of the Group IV tetrahedra that is found for all systems at d_{Ge-S}=2.21 Å, i.e. at a distance identical to the one determined in alkali thiogermanates (see above). The secondary principal peak is found to be related to the sulfur-alkaline earth distance as previously acknowledged for corresponding oxides [137] or the present thiosilicates (Fig. 11), and its position shifts to large r with increasing ion size, i.e. we find d_{Mg-S}=2.39 Å which is a distance somewhat smaller than in the crystalline phase (2.50–2.66 Å, Table 9), and leads

Table 9
Experimental cell parameters, system density (n_0, ρ_0), and main distances of different alkaline earth thiogermanate crystals, compared to calculated values from the BM3PM model in NPT Ensemble at zero pressure, and 100 K. The number N of particles is indicated for each compound.

	Expt.	Model
Mg_2GeS_4	*Pnma*	**N=2520**
a (Å)	12.77 [130], 12.84 [99]	12.82
b (Å)	7.43 [130], 7.47 [99]	7.46
c (Å)	6.01 [130], 6.07 [99]	6.02
n_0 (Å^{-3})	0.049 [99]	0.049
ρ_0 (g cm^{-3})	2.91 [99]	2.88
d_{Ge-S} (Å)	2.14 [130]	2.21
d_{Mg-S} (Å)	2.54 [130]	2.50–2.66
Ca_2GeS_4	*Pnma*	**N=2520**
a (Å)	13.64 [99], 13.61 [131]	13.66
b (Å)	8.20 [99], 8.18 [131]	8.18
c (Å)	6.30 [99], 6.30 [131]	6.29
n_0 (Å^{-3})	0.040 [131]	0.040
ρ_0 (g cm^{-3})	2.66 [131]	2.66
d_{Ge-S} (Å)	2.19 [131]	2.22
$BaGe_2S_5$	$Fd\bar{3}$m	**N=3456**
a (Å)	14.90 [78]	15.19
n_0 (Å^{-3})	0.041 [78]	0.037
ρ_0 (g cm^{-3})	3.48 [78]	3.36
d_{Ge-S} (Å)	2.19 [78]	2.15–2.26
d_{Ba-S} (Å)	3.22 [78]	3.28
Ba_3GeS_5	*Pnma*	**N=4320**
a (Å)	12.05 [132]	12.15
b (Å)	9.55 [132]	9.62
c (Å)	8.60 [132]	8.70
n_0 (Å^{-3})	0.036 [132]	0.035
ρ_0 (g cm^{-3})	4.33 [132]	4.21
d_{Ge-S} (Å)	2.17 [132]	2.16
d_{Ba-S} (Å)	3.31 [132]	3.31
Ba_2GeS_4	*Pnma*	**N=2520**
a (Å)	8.96 [135], 8.98 [136]	9.02
b (Å)	6.89 [135], 6.88 [133]	6.93
c (Å)	12.22 [135,136],	12.31
n_0 (Å^{-3})	0.037 [135,136]	0.036
ρ_0 (g cm^{-3})	4.19 [135,136]	4.10
d_{Ge-S} (Å)	2.18–2.20 [133]	2.19
d_{Ba-S} (Å)	3.12–3.58 [136]	3.24
$BaGeS_3$	$P2_1/c$	**N=2520**
a (Å)	15.37 [133]	15.11
b (Å)	5.76 [133]	5.66
c (Å)	13.42 [133]	13.19
n_0 (Å^{-3})	0.037 [133]	0.039
ρ_0 (g cm^{-3})	4.19 [133]	3.99
d_{Ge-S} (Å)	2.17–2.30 [133]	2.04–2.18
d_{Ba-S} (Å)	3.11–3.61 [133]	3.16–3.32

to a shoulder peak in the amorphous state (2.30 Å). For larger alkaline earth ion size, we found d_{Ca-S}= 2.77 Å and d_{Ba-S}=3.22 Å. As for the alkali thiogermanates, the corresponding structure is made of a depolymerized network with a distribution of connecting tetrahedra (Q^n species).

3.7. P_2S_5 based glasses and crystals

The ternary Li-P-S systems have probably attracted the largest attention in the field of sulfide electrolytes given their important conductivity level that is obtained in both crystallines phases and glass (including glass ceramics). Target materials in this respect are the high Li amount polymorphs such as Li_7PS_6, Li_3PS_4 and $Li_7P_3S_{11}$ which serve as starting materials for further processing of e.g. thio-LiSICON types, halogen substituted Argyrodite-type phosphosulfide electrolytes [138], or quaternary crystals such as LGPS [4] displaying a conductivity as high as 10^{-2} Ω^{-1} cm^{-1}, which is a conductivity

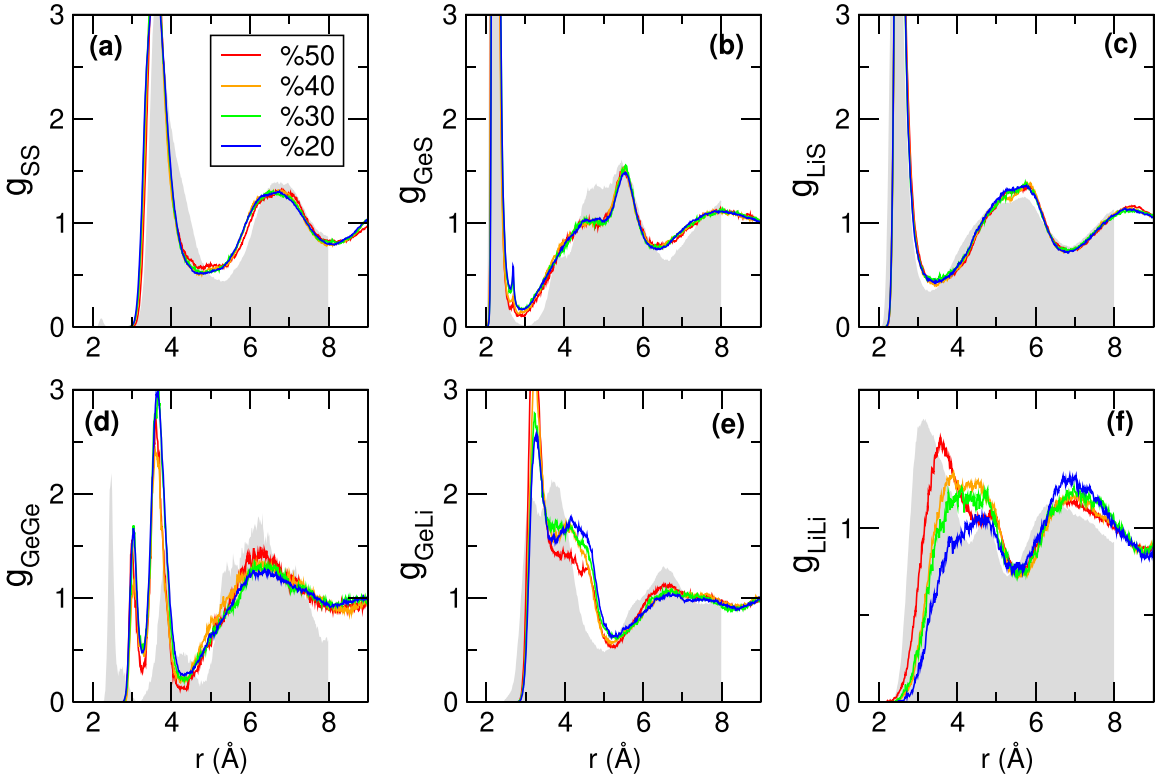

Fig. 15. Calculated partial pair correlation functions $g_{ij}(r)$ for different compositions glassy (100-x)Li_2S – $xGeS_2$ with x=20 % (LG4, blue), 30% (green), 40 % (L2G3, orange) and 50 % (LG, red). The background functions in gray correspond to a L2G (x=66 %) glass obtained from DFT based simulations [128].

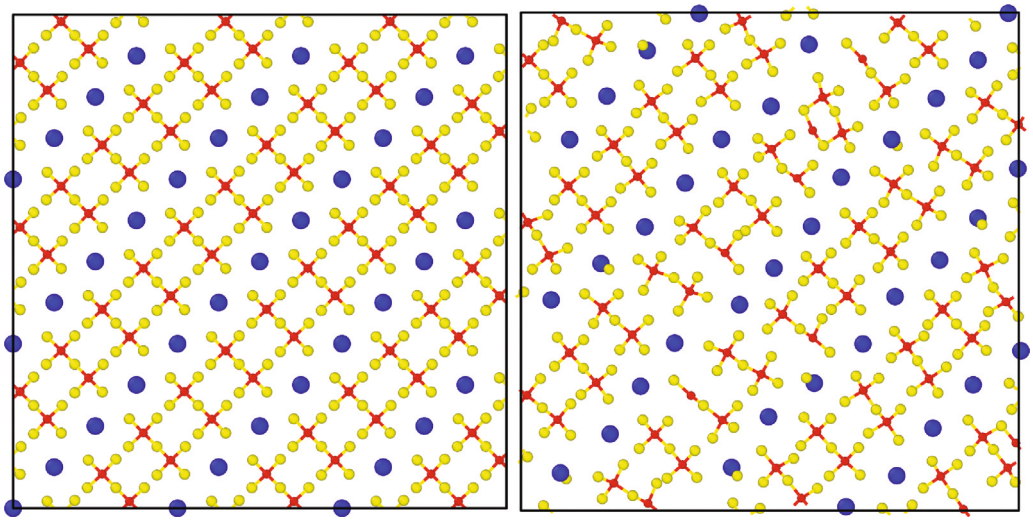

Fig. 16. 2D slab view of the initial (left, proposed structure [78]) and after 100 ps trajectory in NPT at 100 K and zero pressure of the $BaGe_2S_5$ (right). The adamatane-like $Ge_4S_{10}^{4\ominus}$ unit is proposed to be present as well [79], and forms transverse sheets of tetrahedra in the (a, c) direction. Sulfur, Germanium Silicon and Barium are colored in yellow, red, and blue, respectively.

level that is much larger than the maximum achieved in the binary systems, i.e. 3.5×10^{-4} Ω^{-1} cm^{-1} for $25P_2S_5$–$75Li_2S$ [139] and 8.5×10^{-6} Ω^{-1} cm^{-1} for $25P_2S_5$–$75Na_2S$ [140] at room temperature.

3.7.1. Glassy lithium thiophosphates

We first focus on glassy lithium thiophosphates (100-x)P_2S_5 – xLi_2S with large modifier content given the existence of reported structure functions. For all considered compositions reported experimental densities [12] are recovered from our simulations (Fig. 7), and in NVT simulations with fixed experimental densities, we find residual pressures of only 0.12 GPa, 0.06 GPa, and 0.15 GPa for x=67, 70 and 75 Li_2S, respectively. As for the previously investigated materials, Fig. 18 compares the results from the parametrized BM3PM model with the structure functions accessed from X-ray and neutron diffraction [12] ($S_N(k)$, Fig. 19). In reciprocal space, it succeeds in reproducing all relevant peaks of the function $S_X(k)$ for all considered compositions (Fig. 18a), i.e. principal peaks at k ≃3.90 Å^{-1} and k_{PP}=2.10 Å^{-1}, the FSDP at k_{FSDP}=1.6 Å^{-1}, and the typical oscillations found in the region 6 Å^{-1} ≤ k ≤ 8 Å^{-1}, together with a secondary peak at k ≃10 Å^{-1}. This latter range is usually associated with correlations

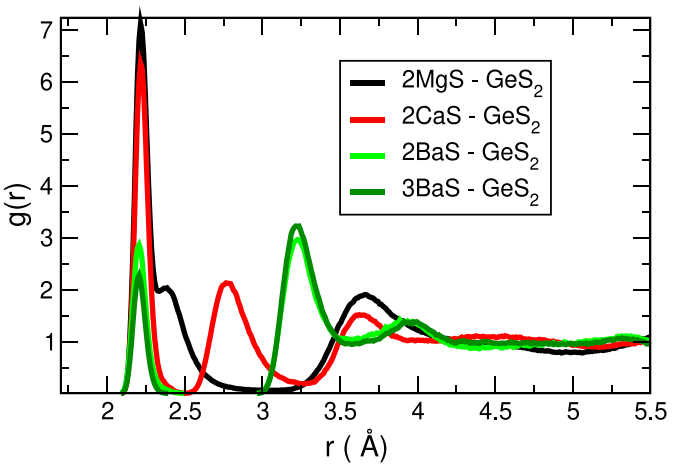

Fig. 17. Calculated X-ray weighted pair correlation function $g(r)$ in GeS_2 – 2MgS (black), GeS_2 – 2CaS (red), GeS_2 – 2BaS (green), and GeS_2 – 3BaS glasses (dark green).

arising from second shell neighbors in real space [141]. The agreement is somewhat maintained for all considered compositions ranging from x=67 % ($Li_4P_2S_7$) up to x=75 % (Li_3PS_4) but with a reduced accuracy when the Wright parameters R_X are being compared to Ge counterparts (Fig. 14). The same level of agreement holds for a neutron weighted structure factor $S_N(k)$ that we represent for the single composition $25P_2S_5 - 75Li_2S$ (Fig. 19b). Here we have used Eq. (5), and the neutron scattering lengths f_i^N of Li, P and S.

A decomposition of the partial contributions $S_{ij}(k)$ indicates that the total structure factor (exemplified for neutron weighted partials $\langle b\rangle^{-2}(2\text{-}\delta_{ij})x_i x_j b_i b_j S_{ij}(k)$ in Fig. 20) is dominated in various k ranges by all correlating pairs. Here δ_{ij} represents the Kronecker symbol. At low k, the FSDP results essentially from network species related partial structure factors, i.e. S–S, P–S, and P–P, whereas the principal peak k_{PP} found at 2.04 $Å^{-1}$ results from a superposition of all partials with a dominant contribution of $S_{SS}(k)$. Noteworthy is the fact that for such highly depolymerized glasses, the alkali ion channel structure found at lower modifier content [71,142,143] has obviously collapsed as we do not find any substantial signature of Li–Li correlations in the range $0 \leq k \leq 2.0$ $Å^{-1}$ (Fig. 20). This feature manifests, indeed, by an important contribution of the alkali–alkali partial structure factor (here $S_{LiLi}(k)$)in the FSDP region [144] which is not observed here. On this simple basis, one can argue that the Li motion at this composition is not spatially limited, and proceeds over extended regions of the glass structure [35].

3.7.2. Local structure of lithium thiophosphates

In real spaoe, the resulting SRO is displayed in Figs. 18b and 21, the latter representing the different partial pair correlation functions $g_{ij}(r)$ for the three considered compositions : 67, 70 and 75 % Li_2S. We find a dominant peak in the P–S correlations $g_{PS}(r)$ at a distance of approximatively $r \simeq 2.05$ Å (Fig. 21b), and a secondary peak at 5.40 Å corresponding to correlations between a P atom and its neighboring Q^n species. The S–S correlations are dominated by two short bond distances at 3.33 Å and 3.69 Å and these distances are related to the edge of the different P-based polyhedra, and to correlations between Q^0 species (snapshot in Fig. 21a). The other dominant peak contributing to the principal peak of the total pair correlation function (Fig. 18b) is detected in the Li–S correlation which exhibits an intense peak (2.62 Å) whose characteristics is independent of composition (Fig. 21c), and lead to broad correlations in the range 3–5 Å for e.g. P-Li and Li-Li partials (Figs. 21e and f).

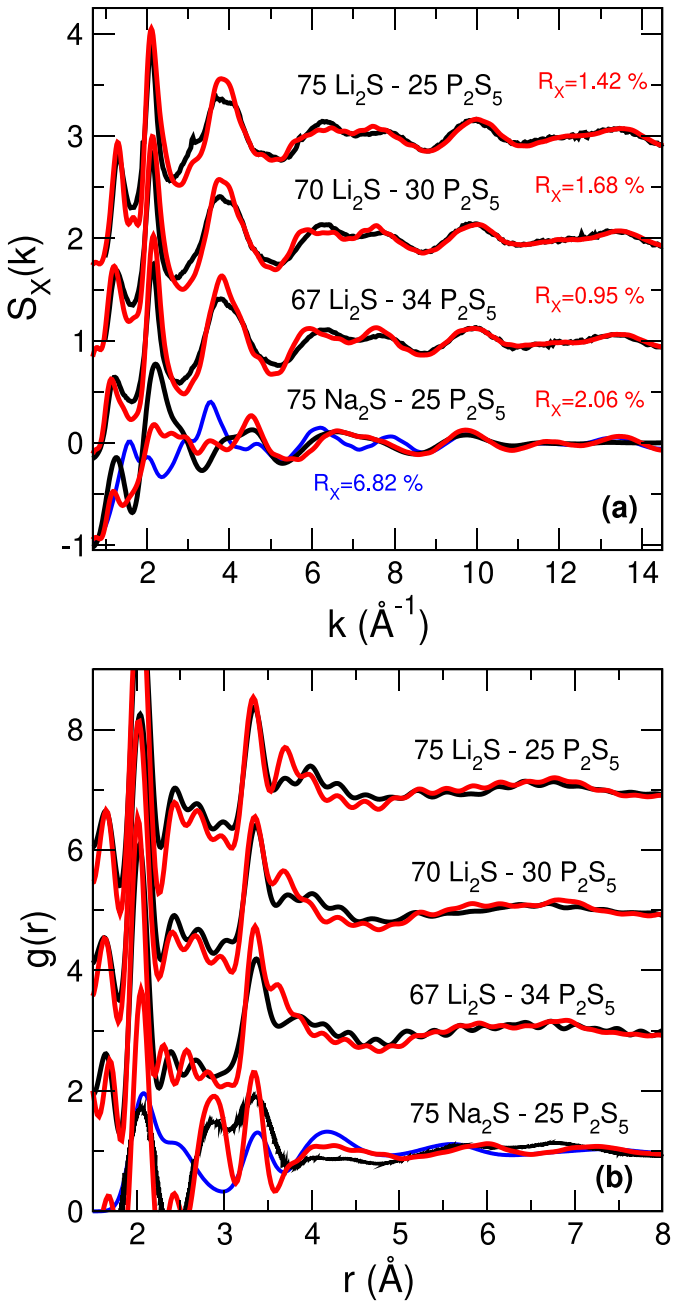

Fig. 18. Calculated (red) X-ray weighted structure factors $S_X(k)$ (a) and corresponding pair correlation functions $g(r)$ (b) of different alkali thiophosphates of the form $(100\text{-}x)P_2S_5 - xM_2S$ (M=Li, Na), and compared to experimental data from X-ray scattering on Li [12] and Na [140] glasses. The blue curve is a simulation using a simple Born–Mayer potential with a different parametrization [70]. Wright parameters R_X are indicated in panel a.

The complete depolymerization of the network is obviously achieved in $25P_2S_5 - 75Li_2S$ as we find a near vanishing of the principal peak at 3.60 Åin $g_{PP}(r)$ (green curve in Fig. 21d), and which corresponds to the distance involved in P-BS-P linkages. In contrast with other simulations however, we do not find any homopolar P–P bonds that are evidenced from DFT simulations, and Raman spectroscopy [12], and which have eventually an additional signature from NMR [145]. These represent minority species in highly depolymerized thiophosphates (4.4–33.0% depending on composition [12]), and contribute to $Li_6P_2S_6$ groupings that are supposed to cause a degradation of conductivity [12,145].

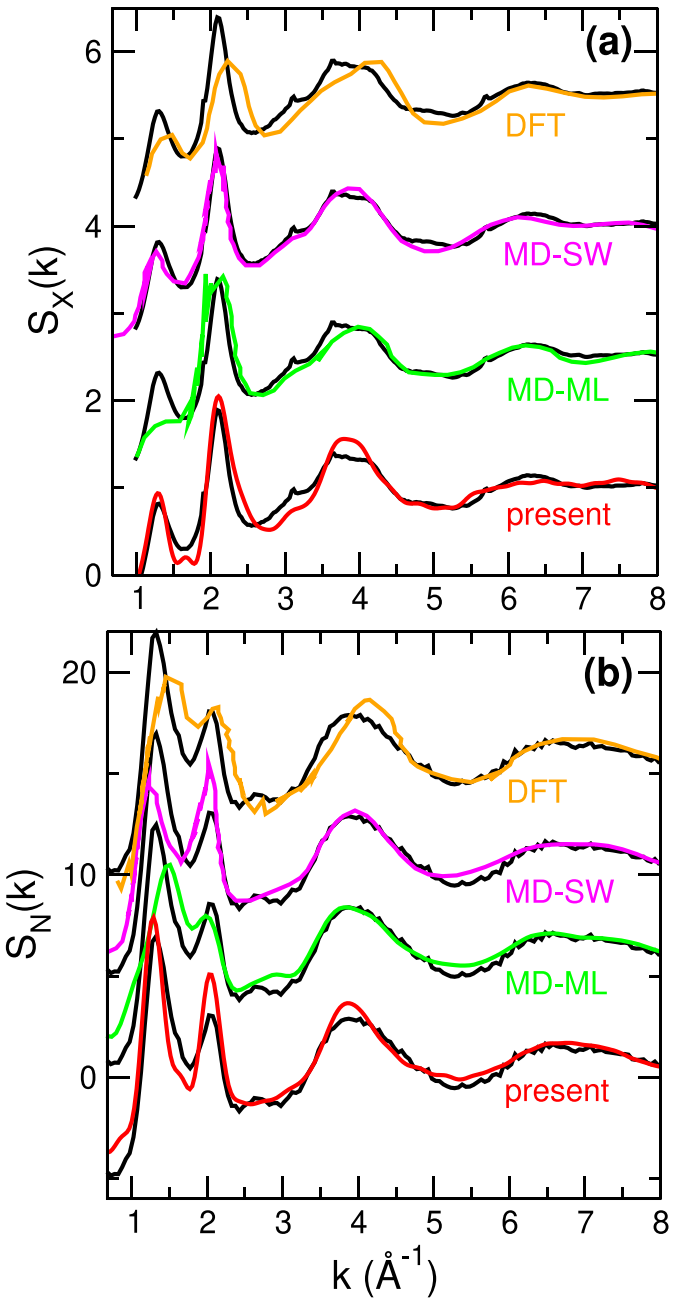

Fig. 19. Models of Li_3PS_4 glass ($75Li_2S$-$25P_2S_5$) and their calculated X-ray (a) or neutron (b) weighted structure factors. Present work (red, same as Fig. 18a), ML potential (green [38]), Stillinger–Weber classical potential (magenta [33]), and DFT based MD (orange [12]).

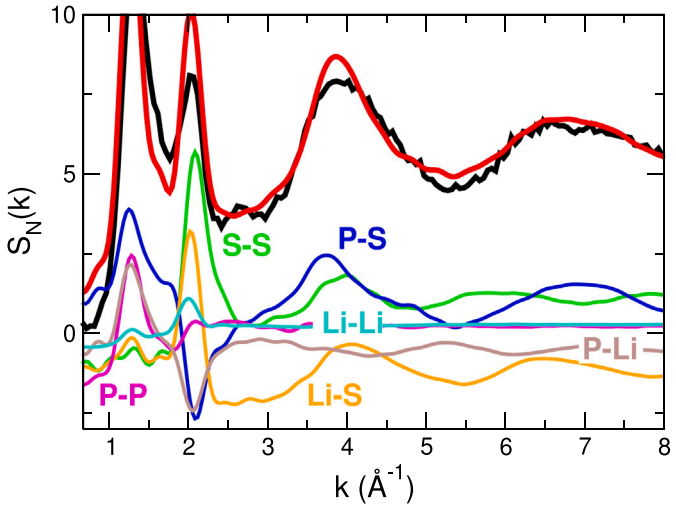

Fig. 20. Decomposition of the total neutron structure factor $S_N(k)$ of $25P_2S_5$–$75Li_2S$ (thick red, same as Fig. 19b) into neutron weighted partials $\langle b\rangle^{-2}(2\text{-}\delta_{ij})x_i x_j b_i b_j S_{ij}(k)$. The black thick curve is the experimental measurement from Ohara et al. [12]. The total structure factor has been shifted by +5 for a clearer presentation.

3.7.3. *The particular case of Li_3PS_4*

Of special interest is the Li_3PS_4 glass which corresponds to $75Li_2S$ – $25P_2S_5$, and which has received a large amount of attention in the literature in terms of atomic-scale description [12,33,38]. In Fig. 19 we compare our results with different modeling schemes that have been recently reported: a classical force-field building on a Stillinger–Weber (SW) form [33], a DFT study [12], and a ML potential [38] derived from the training of *ab initio* simulations of glasses and different crystalline Li-P-S polymorphs. See also Table 10.

A certain number of observations can be made from the X-ray weighted results. First, we remark that the calculated [12] DFT function $S_X(k)$ does not reproduce the main features in reciprocal space properties so that the agreement with experiment is only fair, and in terms of accuracy well beyond what is usually achieved in other sulfides from DFT [18,25,28,87] given that mismatch of peak positions, reduced principal peak intensities, etc. are clearly observed (orange curves in Fig. 19). The ML simulation [38] reproduces rather well the main features of the structure factor, and the short distance given the agreement at large k but completely lacks the FSDP which signals a rather incorrect description of the intermediate range order. Conversely, both classical force fields (SW [33] and the present BM3PM model) correctly reproduce all features of the structure factor $S_X(k)$ including the FSDP region. At large k, all models merely reproduce the long-range oscillations which signals that they all lead to a similar short-range order made of tetrahedral units in predominant Q^0 configuration (see below).

Our conclusions are maintained to the same extent in the case of a comparison with the function $S_N(k)$ (Fig. 19b). These neutron data blow up the peaks in the low-k region ($k \leq 2.0$ Å^{-1}) which are associated with the network-forming species (P,S) because of the small contributions of Li in terms of coherent neutron scattering length. An inspection of the principal peaks found at $k \leq 2.5$ Å^{-1}, again, indicates that both the BM3PM and the SW model describe much better the intermediate range order of the Li_3PS_4 glass as compared to DFT [12] and to ML techniques [38] as the latter lead to a systematic difference with experiment of the FSDP and PP location, width, and intensity (Table 10). In contrast with the other simulations, our decomposition indicates, indeed, that the experimental [12] position k_{FSDP}=1.32 Å^{-1} and the principal peak position k_{PP}=2.05 Å^{-1} are recovered from the BM3PM model as we found 1.31 Å^{-1} and 2.04 Å^{-1}, respectively. The SW and BM functional forms, thus, appear as the most promising interatomic models, and clearly lead to an improved description of short- and medium-range structures of lithium thiophosphates with respect to other modeling schemes.

3.7.4. *Crystalline phases*

The stability of the BM3PM model on several typical crystalline phases of the Li-P-S system has been verified. Table 11 provides calculated cell parameters, densities at zero pressure and typical calculated distances obtained, and compared to measured values.

The 50:50 system crystallizes into $Li_2P_2S_6$ (metathiophsophate) of monoclinic space group C/m, and consists in chains of Q^2 species ($PS_{3/2}$

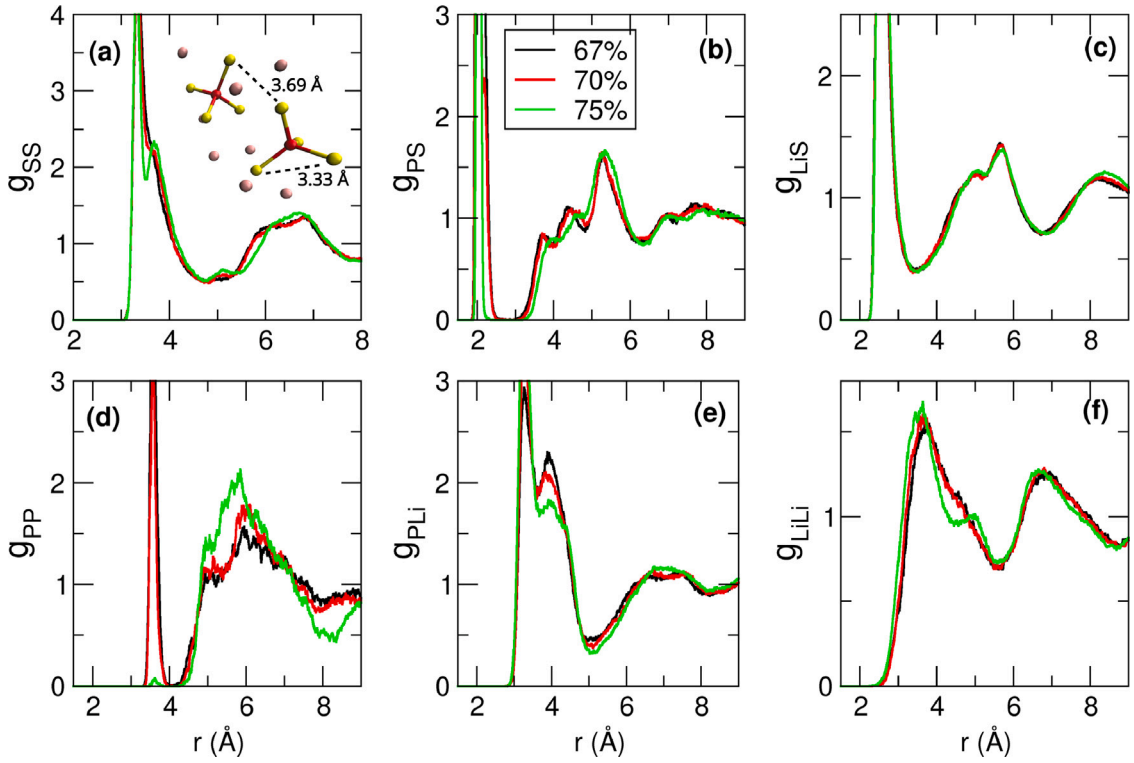

Fig. 21. Calculated partial pair correlation functions $g_{ij}(r)$ for different compositions of glassy (100-x)P_2S_5–xLi_2S with x=67 % (black), 70 % (red) and 75 % (green). The atomic snapshot in panel a is a fragment of the structure of the 75 % glass with the two characteristic S–S bond distances : edge of the $PS_{5/2}$ tetrahedra and S–S correlations between Q^0 species (S: yellow; P: red; Li: pink).

Table 10
Calculated neutron peak positions k_{FSDP} and k_{PP} (in Å^{-1}) of glassy Li_3PS_4, together with calculated Wright parameters R_X^X, and R_X^N for X-ray and neutron scattering. Note that because of the larger intensities in neutron scattering patterns, deviations $S_{exp}(k_i) - S_{calc}(k_i)$ are larger, and lead to larger values for the neutron related Wright parameter R_X^N. See also Fig. 19.

	Expt.[12]	BM3PM	DFT [12]	SW [33]	ML [38]
k_{FSDP}	1.32	1.31	1.53	1.24	1.48
k_{PP}	2.05	2.04	2.17	2.06	2.03
R_X^X (%)		1.42	2.82	0.99	2.06
R_X^N (%)		10.64	28.90	9.34	15.45

tetrahedra with two NBS) that remain stable in NPT at zero pressure with calculated cell parameters that are extremely close to reported data [150], i.e. we find a=11.30 Å, b=7.12 Å, and c=6.64 Å to be compared with the experimental a=11.12 Å, b=7.01 Å, and c=6.53 Å, and this leads to an underestimated density (2.05 g cm^{-3} against 2.15 g cm^{-3}[150]). Typical distances are merely recovered, i.e. we find P–S and Li–S bond distances of about 1.97–2.16 Å and 2.52 Å, respectively (Table 11), comparable to those determined from X-ray diffraction (d_{Li-S}=2.58 Å).

We have also considered the $Li_7P_3S_{11}$ compound which is one of the most studied thiophosphate polymorphs [148,149,151], and which crystallizes in triclinic symmetry. It contains a periodic network made of a 1:1 mixture of isolated ortho-thiophosphate Li_3PS_4 groups (i.e. Q^0 species), and pyro-thiophosphate groups (Q^1 units) of formula $Li_4P_2S_7$. The BM3PM model leads to lattice constants (a=12.71 Å, b=6.15 Å, and c=13.27 Å) which are close to their experimental counterparts [148, 149] : a=12.48–12.50 Å, b=6.03 Å, and c=12.50-12.53 Å). The corresponding calculated angles (β=103.02°, γ=78.14°)) merely reproduce the experimental data [149] (β=113.202°, γ=74.47°).

The last system that we have considered is the Li_3PS_4 compound whose γ and β polymorphs [138] represent the low- and intermediate phases separated by a transition temperature $\gamma \rightarrow \beta$ of 573 K. The low temperature γ-phase of $Pnm2_1$ symmetry is found to be stabilized at zero pressure with the BM3PM model at a somewhat reduced density (1.86 g cm^{-3}) leading to a moderate increase of the elementary cell (i.e. a=7.80 Å compared to the experimental [146] 7.71 Å). The β-phase is found to crystallize in Pnma space group, and we also find a rather good agreement of calculated crystallographic data with respect to experiments. Noteworthy is the fact that an additional phase has been examined, and has been found to be unstable ($Li_4P_2S_6$) as it consists of $P_2S_6^{4\ominus}$ anions giving rise to ethane-like units [152,153], at variance with the other reported polymorphs (Li_3PS_4, etc.) which have as building blocks only the $PS_{5/2}$ tetrahedral unit. In the $Li_4P_2S_6$, the $P_2S_6^{4-}$ anions involve a homopolar P–P bond which cannot be reproduced from the BM3PM model, and furthermore leads to a strong electrostatic repulsion arising from the Coulombic part of the 2-body force-field (Eq. (1)).

3.7.5. *Na thiophosphates*

Regarding the Na-based system, we find a more reduced agreement from the force-field as highlighted for the 75Na_2S – 25P_2S_5 glass in reciprocal (Fig. 18a) and real space (Fig. 18b) which leads to an unsatisfactory convergence of the Wright parameter (R_X=2.06%), although improved when compared to a similar numerical effort [70] (blue curve in Fig. 18a, R_X=6.82%). The oxide counterparts (i.e. phosphates) are known to be less polymerized than Group IV based glasses (silicates), and often compared [154] with polymeric materials so that force-fields inspired from the successful modeling of silicates (or thiosilicates in the present case) may not fully apply. In addition, it is also known that the presence of a terminal oxygen surrounding phosphorus leads

Table 11
Experimental cell parameters, system density (n_0, ρ_0) and main distances of different thiophosphate crystals, compared to calculated values from the BM3PM model in NPT Ensemble at zero pressure, and 100 K. The number N of particles is indicated for each compound. Calculated bond distances correspond to the maximum of pair correlation functions.

	Expt.	Model
β-Li_3PS_4	*Pnma*	N=4500
a (Å)	12.82 [146]	12.86
b (Å)	8.22 [146]	8.25
c (Å)	6.12 [146]	6.14
n_0 (Å^{-3})	0.056 [146]	0.055
ρ_0 (g cm^{-3})	1.92 [146]	1.84
d_{P-S} (Å)	2.05 [147]	2.03
d_{Li-S} (Å)	2.41–3.11 [147]	2.50
γ-Li_3PS_4	$Pmn2_1$	N=2000
a (Å)	7.71 [146]	7.80
b (Å)	6.53 [146]	6.62
c (Å)	6.13 [146]	6.21
n_0 (Å^{-3})	0.052 [77,146]	0.050
ρ_0 (g cm^{-3})	1.93 [146]	1.86
d_{P-S} (Å)	2.04 [146]	1.97
d_{Li-S} (Å)	2.27–2.52 [146]	2.45
d_{S-S} (Å)	3.32 [146]	3.32
$Li_7P_3S_{11}$	$P_{\bar{1}}$	N=5250
a (Å)	12.48–12.50 [148,149]	12.71
b (Å)	6.03 [148]	6.15
c (Å)	12.50–12.53 [148,149]	13.27
n_0 (Å^{-3})	0.049 [148,149]	0.047
ρ_0 (g cm^{-3})	1.91 [149]	1.85
d_{P-S} (Å)	1.98–2.09 [149]	1.97
d_{Li-S} (Å)	2.23–3.09 [149]	2.49
d_{Li-Li} (Å)	2.56 [149]	
$Li_2P_2S_6$	C/m	N=2500
a (Å)	11.12 [150]	11.30
b (Å)	7.01 [150]	7.12
c (Å)	6.53 [150]	6.64
n_0 (Å^{-3})	0.048	0.046
ρ_0 (g cm^{-3})	2.15	2.05
d_{P-S} (Å)	1.97, 2.13 [150]	1.97, 2.16
d_{Li-S} (Å)	2.58	2.52

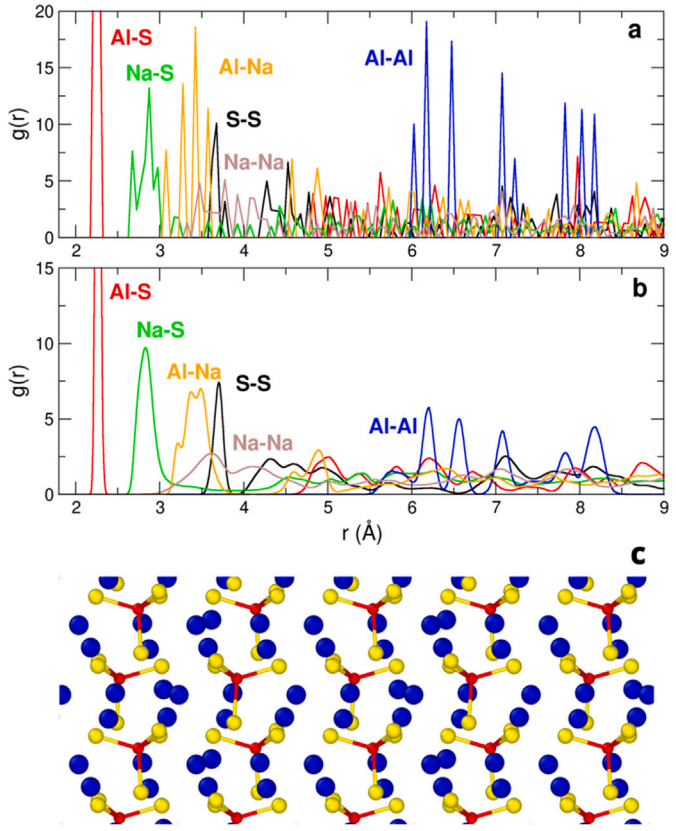

Fig. 22. (a) Pair correlation functions of the different pairs in Na_5AlS_4 taken from the initial configuration crystallographic information file (CIF). (b) Simulated pair correlation function at 100 K after 100 ps relaxation using the BM3PM model. In (c), a snapshot in (*a*, *b*) direction (10 Å slab) is represented, and signals the tetrahedral structure of Al (red). Na and S atoms are in blue, and yellow, respectively.

to an improper medium-range structure when only a two-body interaction [155,156] is considered, so that strategies using 3-body potentials have been developed [64], especially for polymerized glasses with about or less than 50 % alkali modifier. These general comments also apply to the sulfides where obvious alkali size effects (Li versus Na) play a role, and control to some extent the accuracy of the MD description, as revealed from a direct comparison between the numerical results of $75Na_2S - 25P_2S_5$, and $75Li_2S - 25P_2S_5$ (Fig. 18).

Concerning the pair correlation function $g(r)$ of the sodium thiophosphate (Fig. 18b), we acknowledge a rather correct reproduction of the principal peak corresponding to the P–S bond at 2.11 Å but have a clear separation of second-shell distances found at 2.90 Å and 3.35 Å, which correspond to the Na–S and the S–S correlations, respectively. In the simulation result, the splitting of the two peaks within this distance range is responsible [141] for the fair agreement in reciprocal space in the wavevector region $k \lesssim 3.0$ Å^{-1} (Fig. 18a), including the FSDP. Here, the contribution of Eq. (2) that we have used to model successfully the low k region (Fig. 10) in other glasses does not act efficiently given the near absence of P–BS–P linkages at such elevated modifier compositions. Despite these observed flaws, we note that the present force-field still represents an improvement with respect to a previously reported [70] force-field for Na_2PS_3 (x=75 %), at least in real space (blue curves in Fig. 18). We, furthermore, keep in mind that in corresponding oxides the molecular dynamics modeling $xNa_2O - (1\text{-}x)P_2O_5$ also remains challenging, and needs a variety of 3-body interactions, including Na-related ones [157], in order to fairly reproduce experimental structure functions. Work in this direction is in progress.

3.8. Aluminum sulfides

A certain number of Aluminum-based compounds have been recently investigated [84] in the context of an aliovalent substitution of Si by Al in the base crystalline structures Na_4SiS_4 and Li_4SiS_4. The role of substitution has been emphasized in early studies [158,159] as the increase of the number of charge carriers combined with an expansion of the crystal lattice by a larger cation (i.e. Al) with a reduced charge is supposed to enhance alkali ion conductivity. We are not aware of any study of binary M_2S-Al_2S_3 glasses due probably to a poor glass-forming tendency that has been emphasized in studies on the effect of Al on the ternary Li_2S — Al_2S_3 — SiS_2 [160–162] or Li_2S — Al_2S_3 — P_2S_5 systems [163,164].

As for the alkaline earth based materials, we apply the GULP methodology alone to the Na_5AlS_4, and Li_5AlS_4 compounds, and corresponding results of the BM3PM model are provided in Table 12 which emphasize the reproducibility of the crystallographic data for both Li- and Na thioaluminates as densities are maintained at zero pressure, and cell lengths recovered, i.e. we found in Li_5AlS_4 formed in a=6.91 Å (exp. [165] 6.86 Å), and b=7.84 Å and c=6.25 Å identical to the experimental result. In the sodium system (Fig. 22), the initial crystalline structure (panel a) is also maintained after 100 ps relaxation (Fig. 22b) with a global broadening of the crystalline peaks from phonon vibration, an insight into the structure signaling the sheet-like structure of Na_5AlS_4, and the tetrahedral geometry of Al (Fig. 22c).

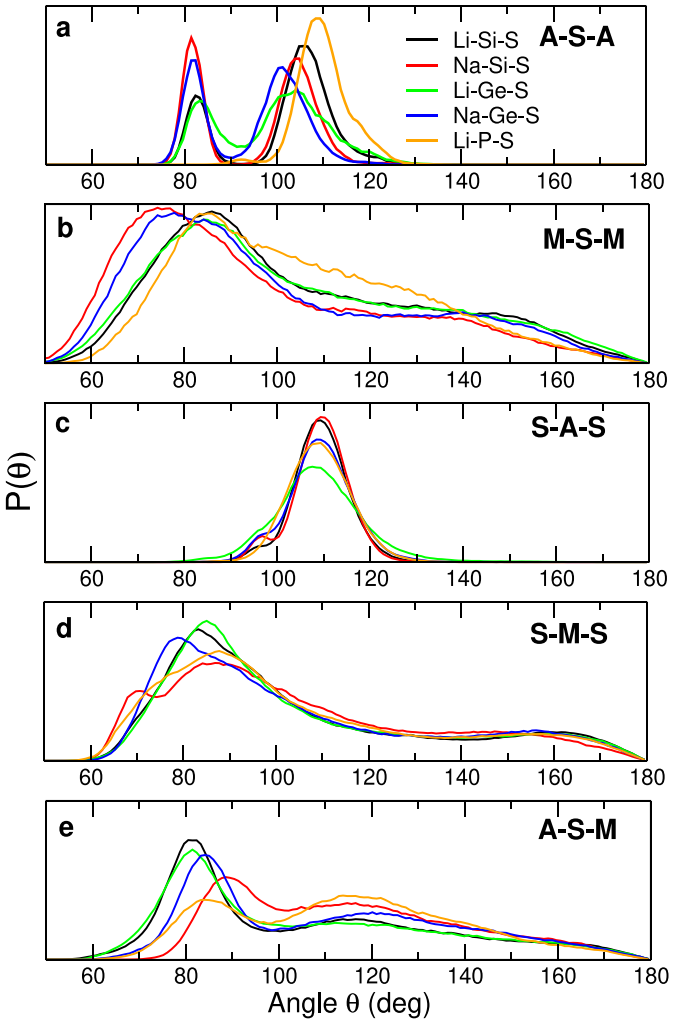

Fig. 23. Calculated bond angle distribution in $50AS_2$–$50M_2S$ (A=Ge, Si, and M=Li, Na), and $50P_2S_5$–$50Li_2S$ for various triplets which are relevant in such glasses.

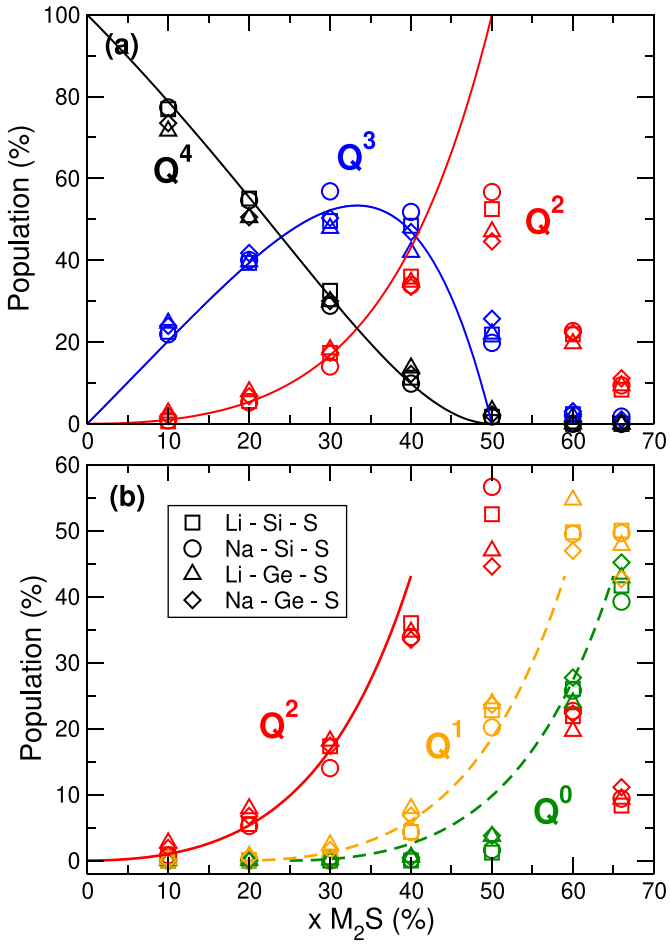

Fig. 24. Calculated population of Q^n species in Li-Si-S (boxes), Na-Si-S (circles), Li-Ge-S (triangles), and Na-Ge-S (diamonds) glasses as a function of modifier composition M_2S. The solid lines at low modifier content correspond to a statistical speciation model [167] (Eq. (13)) with K_e=0.19. Broken lines for Q^1 and Q^0 serve only as a guide. The Q^2 speciation is duplicated in panel b.

4. Sulfide glasses : Bonds and topology in real space

Having established the force-fields for a variety of modified sulfide glasses using as network former SiS_2, GeS_2, and P_2S_5, it is instructive to inquire how the alkali modifier will induce modifications of the base structure. In the following, we first focus on a 50:50 composition containing 50 % modifier, in order to disentangle effects of both network formers, and modifiers on angles or rings, but then also consider the global effect of Na_2S and Li_2S on the Q^n speciation, and coordination numbers.

4.1. Bond angle distributions

In Fig. 23, we represent a select number of BADs of the different glasses in the 50:50 ratio of network former vs. modifier. We first note that, as expected from the study of the effect of the 3-body interaction (Eq. (2)), the A–S–A BAD (A=Si,Ge) displays a bimodal distribution (Fig. 23a) indicative of the two types of connections present in sulfide glasses, i.e. ES and CS tetrahedra with typical angles of about 81–83° (ES) and 101–106° (CS), the latter evolving to lower angles with increasing alkali and Group IV atom size, i.e. we found θ=106° for the Li–Si–S system, and θ=101° for the Na–Ge–S system. Noteworthy is the fact that the ES connections in the thiophosphate glass are barely visible which signals a reduced statistics, as also described, and confirmed below from the ring enumeration. This feature is also evidenced from the profile of the correlation function g_{PP} (Fig. 21d) which does not contain the typical ES peak found in corresponding Group IV glasses (e.g. Fig. 13d).

We, furthermore, recover the tetrahedral character for all glasses, and this manifests by a sharp peak centered at $arccos(-1/3)$=109.47° (Fig. 23c). The BADs involving alkali ions are represented in the other panels. Fig. 23d which represents S–Li–S and S–Na–S BADs, indicates that the alkali ions are in a defect octahedral geometry given the dominant contribution at 80–90°, and a significant tail at $\theta \simeq$160°. The coordination number of Li, and Na, are, indeed, found to be lower than 6 ($\simeq$ 4–5) which justifies the possibility of such defect geometries, as in other chalcogenide materials [166].

We, finally, note that the NBS environment is largely system dependent (Fig. 23e), as all BADs display a different profile but with a dominant contribution at $\theta \simeq$80–90°, corresponding to the dominant angle in, e.g. Si-NBS-Na in the $50SiS_2$ – $50Na_2S$ system.

4.2. Q^n speciation

The present sulfide glasses display the same trend of the Q^n speciation with modifier content as their oxide counterparts [39,40], i.e. a

progressive conversion from the base Q^4 unit representing the SRO of the network former (Fig. 1) to Q^3, Q^2, etc. upon modifier addition.

We calculate from the amorphous trajectories of the different glasses the statistics of such Q^n species with varying composition by enumerating for each given central A atom (A=Si, Ge, P) the number n of A–S–A linkages within a distance lower than the cutoff-distance r_c of the partial pair correlation function $g_{AA}(r)$ (e.g. $r_c \simeq 4.3$ Å in Na–Ge–S, see Fig. 13d).

Figs. 24 and 25 display such statistics as a function of the network modifier M_2S (M=Li, Na). In Group IV sulfides (Fig. 24), the global behavior reproduces the one determined in the early NMR study [39] on alkali silicates, i.e. a maximum is found in the Q^3, Q^2, Q^1 populations at $x \simeq 33$ % and 50 %, and 60 %, respectively. Unlike the silicates however for which effects of Li, Na and K are important, we find only a small alkali size dependence on the statistics which appears to be weakly sensitive, indeed, to the nature of the (Ge, Si) and (Li, Na) atoms, except a small increase of Q^3 and Q^2 populations in the Na-Si-S glass (Fig. 24a). At low modifier content ($x \leq 40$ %), the Q^n species population can be exactly predicted from a statistical speciation model [167] (solid lines, Fig. 24) which builds on probability p_n (n=4, 3, 2) of finding three species Q^n. Charge conservation leads to :

$$R = \frac{2x}{1-x} = p_3 + 2p_2 \tag{11}$$

and the definition of an equilibrium constant $K_e = p_2 p_4 / p_3^2$ of the reaction [40]:

$$2Q^3 \longleftrightarrow Q^2 + Q^4, \tag{12}$$

leads to an explicit statistics for the species :

$$p_3 = \frac{R(2-R)}{1+\sqrt{(1-R)^2 + 4K_e R(2-R)}}, \tag{13}$$

out of which one determines $p_2 = (R - p_3)/2$, and $p_4 = 1 - p_2 - p_3$ (solid curves in Fig. 24).

In sulfides, the system dependence of the fitted parameter K_e is small, and its average value ($K_e \simeq 0.19$) is larger than the K_e values determined for different alkali silicates [39] (0.01–0.08), which indicates an increased depolymerization, and a reduced Q^3 population in the region $0 \leq x \leq 50$ %. The calculated statistics (Fig. 24) also appears to be consistent with the populations calculated from previous force-fields, either a simple 2-body potential [32] or a ML-derived one [36], which all lead to a dominant population of Q^2 units at the 50:50 composition, the fraction being somewhat underestimated for the former (35.4%, Table 13). Finally, we note that the calculated statistics for the $50SiS_2 - 50Na_2S$ (NS) system is very close to the one determined from NMR [48], and corresponds to a glass dominated by Q^2 species. For larger modifier concentrations (Fig. 24b), the population of isolated A tetrahedra increases (Q^0) and becomes the dominant motif at the most elevated composition (66 % modifier, Fig. 24b) with a probability of about 40–45 %, of the same order as the Q^1 species which is the base motif of crystalline pyro-thiosilicates or pyro-thiogermanates.

In the lithium thiophosphate (Fig. 25, the calculated Q^n follows the same trend as the Group IV sulfides, i.e. the Q^4 fraction typical of P_2S_5 decreases to nearly zero at about 50 % modifier, and closely follows the behavior of corresponding oxides (sodium phosphates [157], broken curves in Fig. 25) which is found to be similar to the Van Waser theoretical distribution [169] which builds on the chemical reaction [154]: $2Q^n + Li_2S \rightarrow 2Q^{n-1}$. Consistently, with increasing modifier content, Fig. 25 suggests the progressive conversion $Q^4 \rightarrow Q^3 \rightarrow Q^2 \rightarrow Q^1 \rightarrow Q^0$, rather different from an ideal chemical model [168], and at 75 % Li_2S, one expects nearly 100 % Q^0 as already analyzed from the calculated partial correlations (Fig. 21).

Table 12
Experimental cell parameters, system density (n_0, ρ_0) and main distances of different alkali thioaluminate crystals, compared to the present calculated values from the BM3PM model in NPT Ensemble at zero pressure, and 100 K. The number N of particles is indicated for each compound.

	Expt.	Model
Na_5AlS_4	*Pbca*	N=**3840**
a (Å)	12.01 [84]	12.05
b (Å)	7.05 [84]	7.06
c (Å)	21.56 [84]	21.61
n_0 (Å^{-3})	0.043 [84]	0.043
ρ_0 (g cm^{-3})	1.96 [84]	1.95
d_{Si-S} (Å)	2.24–2.27 [84]	2.26
d_{Na-S} (Å)	2.86–2.96 [84]	2.81
Li_5AlS_4	$P2_1/m$	N=**2500**
a (Å)	6.86 [165]	6.91
b (Å)	7.84 [165]	7.90
c (Å)	6.25 [165]	6.25
n_0 (Å^{-3})	0.059 [165]	0.058
ρ_0 (g cm^{-3})	1.88 [165]	1.84
d_{Al-S} (Å)	2.24–2.29 [165]	2.24
d_{Li-S} (Å)	2.34–2.56 [165]	2.45

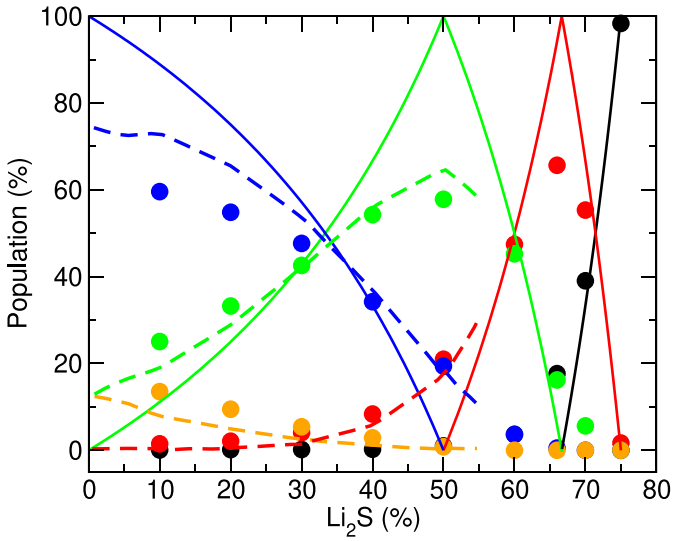

Fig. 25. Calculated population of Q^n species (symbols) in Li-P-S glasses as a function of modifier composition Li_2S. The solid lines correspond to the prediction of the general chemical order (ideal) model [168], and the broken lines are results from MD simulations of corresponding sodium phosphates [157].

4.3. Ring statistics

We have mentioned above the crucial question of the ES population that are specific to modified sulfides. Here we address this issue by using a ring statistics algorithm which builds on a rigorous investigation of networks generated using simulation (RINGS) code [170]. We determine for the different 50:50 systems the fraction of such ES motifs and the concentration of small rings of size $n \leq 8$ where n is the number of atoms belonging to a ring. The algorithm is based on the King [94]-Franzblau [171] shortest-path search to find rings containing a maximum of n=8. Results are provided in Table 13 for ES-related structures alone (E^k functions) for the $50SiS_2 - 50Li_2S$ and $50SiS_2 - 50Na_2S$ glasses, and in Table 14 for all types of rings, and other systems.

We first note that in thiosilicates for which a NMR determination is available [44,47], the calculated fraction of E^k functions is close to the one obtained experimentally, i.e. we found a E^1:E^0 ratio equal

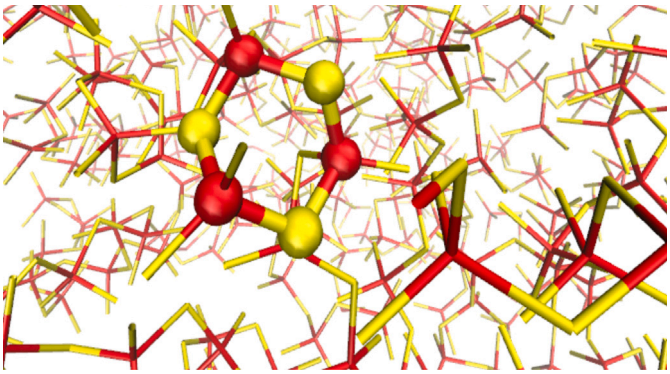

Fig. 26. A 6-ring (spheres) detected in glassy $50P_2S_5$–$50Li_2S$. Only P (red) and S (yellow) atoms are represented.

Table 13
Comparison of the Q^n speciation ($0 \leq n \leq 4$) and E^k functions (k=0, 1, 2) obtained from the BM3PM model in $50SiS_2$ – $50Li_2S$ (LS), and $50SiS_2$ – $50Na_2S$ (NS), together with previous results (theoretical or experimental).

n	4	3	2	1	0	E^2	E^1	E^0
LS								
Present work	1.7	21.8	52.5	22.8	1.2		16.0	84.0
Expt (NMR [44])	50.0		50.0				23.0	77.0
FF-MD [32]	7.5	30.6	35.4	20.7	5.8			100.0
ML-MD [36]	4.2	14.4	59.6	20.6	1.1	0.3	65.2	34.5
NS								
Present work	1.8	19.8	56.6	20.2	1.6		26.9	73.1
Expt (NMR [44,48])		14.1	69.4	17.4			50.0	50.0

Table 14
Calculated population (in %) of A atoms (Si, Ge, P) belonging to rings in $50AS_2$-$50M_2S$ (A=Ge, Si, and M=Li, Na), and $50P_2S_5$–$50Li_2S$. To determine the populations, a cutoff of 2.7 Å has been used (minimum of the partial pair correlation functions A-S).

n	4 (ES)	6	8
$50SiS_2$–$50Li_2S$	24.0	9.6	1.6
$50GeS_2$–$50Li_2S$	31.6	10.2	1.6
$50SiS_2$–$50Na_2S$	40.4	5.4	
$50GeS_2$–$50Na_2S$	37.2	12.6	2.4
$50P_2S_5$–$50Li_2S$	2.9	14.1	

to 16:84 and 27:73 for the lithium, and sodium glass, respectively, whereas NMR suggests 23:77, and 50:50. At this composition of 50 % modifier, the network does not contain anymore E^2 motifs which are usually promoted by the presence of Q^4 and Q^3 species (Fig. 24a). In contrast to earlier numerical studies [32,36] which pointed either to a complete absence of small rings (100 % E^0) or a dominant population of E^1 (65.2%), our result appear, thus, to be fully in line with the experimental determination, albeit underestimated.

In the other glasses (Table 14), we find that Na-based systems systematically lead to a larger fraction of ES tetrahedra as we found 40.4% ES, and 37.2% in thiosilicates and thiogermanates, respectively, to be compared with 24.0%, and 31.6% for the lithium counterpart, respectively. For all Group IV sulfides, larger rings ($6 \leq n \leq 8$, Fig. 26) are found as minority motifs (i.e. 12.6% in $50GeS_2$ – $50Na_2S$) but we note that 6-rings seem to be promoted with increasing atomic size (sodium thiogermanates), and such motifs have been also detected in corresponding DFT based simulations [18]. Conversely, we note that the corresponding thiophosphate glass does not display a tendency to form ES connections as the corresponding statistics is found to be very small (2.9%), consistently with the P-S-P BAD (Fig. 23a), and the absence of P-BS-P linkages. The population of 6-rings is of the same order as the one found in the other glasses.

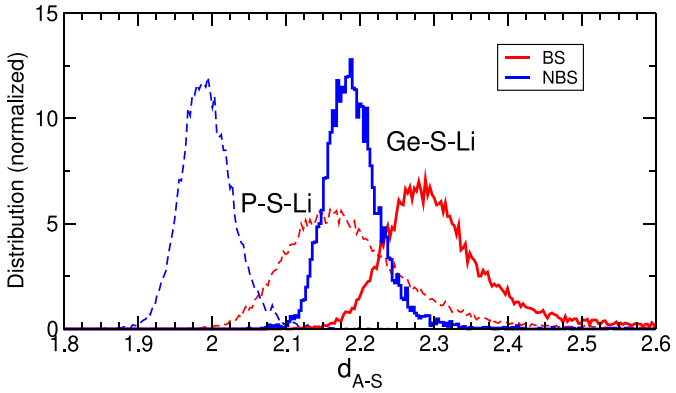

Fig. 27. Si-BS, P-BS (red) and Si-NBS, and P-NBS (blue) bond distributions in glassy $50GeS_2$–$50Li_2S$ (solid curves) and $50P_2S_5$–$50Li_2S$ (broken curves.

4.4. BS and NBS bonds

We, finally, investigate the bonding properties of sulfur atoms of the different glass systems. Fig. 27 represents the A-BS (red, with A=Ge,P) and A-NBS (blue) bond-distance distribution for two select glass systems, $50GeS_2$–$50Li_2S$, $50P_2S_5$–$50Li_2S$. We find a bond length difference between the distributions, i.e. the average Ge-BS and Ge-NBS distances are found to be 2.28 Å and 2.18 Å in the Ge-S-Li system, which is of the order of the one determined in amorphous [172,173] or crystalline silicates [174,175]. For the other system represented in Fig. 27 (P-S-Li), we find an increased bond length difference with average P-BS and P-NBS distances of 2.15 Å, and 1.90 Å, respectively. These features are systematically observed in variety of materials, including for the recently examined Li_2S-SiS_2 glass [32]. In the literature, the origin of this difference has been assigned to the influence of the alkali ions on the neighboring charges and the Si–NBS iono-covalent character of the bonding that modifies the electronic structure of next neighbor A atoms.

Recently, the origin has been completely solved from an analysis of the charge density [18], and the nature of the chemical bonding which reflects a delicate balance between electron localization on the atomic sites involved in ionic bonding and electronic delocalization, i.e., covalent effects. The bond length difference has been found to result from the non directional character of the NBS-M bond (M=Li, Na), the electronic density of NBS atoms pointing essentially towards the close A atom with a relatively well-defined depletion of the valence charge. This feature has been found to be at variance with the electronic characteristics of the BS atoms for which the p orbitals contribute to the deformation of the valence charge in a direction perpendicular to an A-A line connecting two CS tetrahedra, and which involve a reduced charge depletion.

5. Summary and conclusion

Here we have introduced and discussed the possibility to model numerically sulfide glasses and crystals using molecular dynamics simulations. The number of available force-fields published in the literature remains small as compared to corresponding oxide glasses.

We have built on an approach [65] successfully applied to oxides in order to provide the force field parametrization of different modified binary sulfide glasses and crystals containing a network former (SiS_2, GeS_2, P_2S_5, Al_2S_3, …) and network modifiers, i.e. alkali (essentially Li_2S and Na_2S), and alkaline earth sulfides (MgS, CaS, BaS). The approach builds on 1) a minimization of the spread of crystallographic data within the GULP method, and 2) on the minimization of another spread (the so-called Wright parameter) comparing calculated and

experimental structure factors $S(k)$ in glasses. We have used a Born–Mayer potential together with a 3-body angular interaction, termed as the BM3PM model. While the former interaction permits to reproduce qualitatively [32] a certain number of structural properties such as coordination numbers and an overall network depolymerization (quantified via the Q^n speciation) with increasing modifier content, this simple 2-body parametrization leads a rather poor agreement with the experimental structure functions for certain r and k ranges (pair correlations, structure factor), and does not reproduce the salient features of sulfides, and more generally chalcogenides. Among such properties, we had previously noticed [32] that such simple BM potentials do not lead to the possibility of having both ES and CS tetrahedra which are well documented from NMR and Raman spectroscopic studies. The inclusion of a 3-body term that severely constrains (θ_0=0) the angular interaction not only permits to obtain such motifs as revealed from the resulting bimodal Si–S–Si bond angle distributions with ES and CS contributions, but also leads to an accurate reproduction of the structure factor and the FSDP region at low k vector.

We have then extensively checked the parametrization of the BM3PM model for different binaries at different compositions including SiS_2–M_2S (M=Li, Na), SiS_2–M'S (M'=Mg, Ca, Ba), GeS_2–M_2S (M=Li, Na), GeS_2–M'S (M'=Mg, Ca, Ba), P_2S_5–M_2S (M=Li, Na), both in the crystalline and amorphous phases. Results reveal an agreement with experiments that ranges from excellent (e.g. GeS_2–Li_2S) to good (e.g. P_2S_5–Na_2S), depending on the nature of the network former and the modifier cation. The reasons of the system-dependent level of accuracy of the BM3PM model quantified by the Wright parameter R_X are not fully understood at this stage. We conjecture that there might be intrinsic limitations of the used functional form unable to capture certain features related to chemistry such as e.g. chemical bonding, alkali size effects, but we cannot fully discard the need to have accurate, and reliable experimental data for various glass compositions in order to improve the optimization process of the force-field parameters.

When the comparison is possible, the resulting structural BM3PM models are fully consistent with select *ab initio* data on thiogermanates, and thiosilicates which provide the partial correlations in real space, and also display a combination of ES and CS tetrahedral connections, the former being disrupted by the network depolymerization. For select cases (thiosilicates, thiophosphates), the BM3PM model can be compared with reported classical MD, ML-MD and *ab initio* results, and it is found that our parametrization leads to an improved reproduction of the structural properties.

Having established this first systematic computational effort on an important class of sulfide materials, future directions and extensions can be sketched. For select systems (e.g. Na_2S-P_2S_5), there will be need to improve the parametrization either by considering alternative popular functionals (Morse, Stillinger–Weber), additional interactions involving e.g. the alkali cation, or by targeting more compositions for which experimental data are available in order to constrain the parameter space. For other systems, there is clearly need to accumulate new experimental data on structural or mechanical properties, the latter being crucial for optimized fitting strategies within the GULP approach.

Regarding other directions of inquiry, one might use such models to investigate crystallization and crystallization kinetics including with e.g. prepared germs. For e.g. the Ca-Ge-S system which has a melting temperature of about 2000 K, we have verified that on the nanosecond scale a crystal–liquid interface remains stable at a somewhat lower temperature. As in many other disordered systems (See however Ref. [176]), the caveat is the limitation of computer timescale (typically 10 ns) so that a complete crystallization might not be accessible numerically as in other chalcogenides (GeTe or Ge-Sb-Te) prone to crystallization [177]. On the other hand, the investigation of interfaces at low temperature such as those involved in glass ceramics [38] might well represent a natural and future extension of this work and results.

CRediT authorship contribution statement

L.-M. Poitras: Writing – review & editing, Writing – original draft, Visualization, Validation, Methodology, Investigation, Formal analysis, Data curation. **M. Micoulaut:** Writing – review & editing, Writing – original draft, Visualization, Validation, Supervision, Project administration, Methodology, Investigation, Funding acquisition, Formal analysis, Conceptualization.

Declaration of competing interest

The authors declare the following financial interests/personal relationships which may be considered as potential competing interests: Matthieu Micoulaut reports financial support and administrative support were provided by Fondation MAIF pour la recherche. If there are other authors, they declare that they have no known competing financial interests or personal relationships that could have appeared to influence the work reported in this paper.

Acknowledgments

This work is supported by Fondation MAIF pour la recherche. MM acknowledges Chaire d'Excellence between Sorbonne Université and Universidad Autónoma de Mexico (UNAM) for financial support and repeated funding from CNRS and Sorbonne Université. He also acknowledges supercomputing access to the cluster Romeo from Université de Reims Champagne-Ardennes, and has abandoned the idea of being funded by the controversial ANR. Ongoing discussions with Gerardo Naumis, Hugo Flores-Ruiz, S. Sørensen, Olivier Masson, Andrea Piarristeguy, Virginie Viallet, Jean-Gabriel Barthélemy, and P. Boolchand are gratefully acknowledged.

References

[1] M. Weiss, R. Ruess, J. Kasnatscheew, Y. Levartovsky, N.R. Levy, P. Minnmann, L. Stolz, T. Waldmann, M. Wohlfahrt-Mehrens, D. Aurbach, et al., Fast charging of lithium-ion batteries: a review of materials aspects, Adv. Energy Mater. 11 (2021) 210112.
[2] J.-M. Tarascon, M. Armand, Issues and challenges facing rechargeable lithium batteries, Nature 414 (2001) 359–367.
[3] C. Masquelier, Lithium ions on the fast track, Nat. Mater. 10 (2011) 649–650.
[4] N. Kamaya, K. Homma, Y. Yamakawa, M. Hirayama, R. Kanno, M. Yonemura, T. Kamiyama, Y. Kato, S. Hama, K. Kawamoto, et al., A lithium superionic conductor, Nat. Mater. 10 (2011) 682–686.
[5] Z.A. Grady, C.J. Wilkinson, C.A. Randall, J.C. Mauro, Emerging role of non-crystalline electrolytes in solid-state battery research, Front. Energy Res. 8 (2020) 218.
[6] S.S. Sørensen, D. Boysen, E.R. Lindbjerg, H.N. Mortensen, K.T. Lippert, S.M. Diget, Z. Konieczna, M. Micoulaut, M.M. Smedskjaer, Balancing fracture toughness and ionic conductivity in lithium thiosilicate glassy electrolytes, Phys. Chem. Chem. Phys. 27 (2025) 10331–10341.
[7] K. Mori, K. Iwase, Y. Oba, K. Ikeda, T. Otomo, T. Fukunaga, Structural and electrochemical features of $(Li_2S)_x$ - $(SiS_2)_{100-x}$ superionic glasses, Solid State Ion. 344 (2020) 115141.
[8] A. Pradel, A. Piarristeguy, Thio and selenosilicates, sulfide and selenide counterparts of silicates: similarities and differences, C. R. Géosci. 354 (2022) 79–99.
[9] H. Eckert, Z. Zhang, J.H. Kennedy, Structural transformation of non-oxide chalcogenide glasses. The short-range order of lithium sulfide (Li_2S)-phosphorus pentasulfide (P_2S_5) glasses studied by quantitative phosphorus-31, lithium-6, and lithium-7 high-resolution solid-state NMR, Chem. Mater. 2 (1990) 273–279.
[10] F. Mizuno, A. Hayashi, K. Tadanaga, M. Tatsumisago, New, highly ion-conductive crystals precipitated from Li_2S–P_2S_5 glasses, Adv. Mater. 17 (2005) 918–921.
[11] K. Mori, T. Ichida, K. Iwase, T. Otomo, S. Kohara, H. Arai, Y. Uchimoto, Z. Ogumi, Y. Onodera, T. Fukunaga, Visualization of conduction pathways in lithium superionic conductors: Li_2S-P_2S_5 glasses and $Li_7P_3s_{11}$ glass–ceramic, Chem. Phys. Lett. 584 (2013) 113–118.
[12] K. Ohara, A. Mitsui, M. Mori, Y. Onodera, S. Shiotani, Y. Koyama, Y. Orikasa, M. Murakami, K. Shimoda, K. Mori, et al., Structural and electronic features of binary Li_2S-P_2S_5 glasses, Sci. Rep. 6 (2016) 1–9.
[13] C. Massobrio, J. Du, M. Bernasconi, P.S. Salmon, et al., Molecular Dynamics Simulations of Disordered Materials, Springer, 2015, p. 215.

[14] C. Angell, Fast ion motion in glassy and amorphous materials, Solid State Ion. 9 (1983) 3–16.

[15] C. Angell, Recent developments in fast ion transport in glassy and amorphous materials, Solid State Ion. 18 (1986) 72–88.

[16] M. Seshasayee, K. Muruganandam, Molecular dynamics study of Li_2SiS_3 glass, Solid State Ion. 91 (1996) 285–288.

[17] K. Itoh, Structural study of Li_2S-GeS_2 glasses: GeS network and local environment of Li, Solid State Ion. 383 (2022) 115986.

[18] M. Micoulaut, A. Piarristeguy, O. Masson, L.-M. Poitras, R. Escalier, A. Kachmar, A. Pradel, Quantitative assessment of network depolymerization in archetypal superionic glasses and its relationship with ion conduction: A case study on Na_2S-GeS_2, Phys. Rev. B 108 (2023) 144205.

[19] J. Lee, A. Pradel, G. Taillades, M. Ribes, S. Elliott, Structural studies of glassy $(Li_2S)_{0.5}(SiS_2)_{0.5}$ by isotopic-substitution neutron diffraction, Phys. Rev. B 56 (1997) 10934.

[20] S. Elliott, Isotopic-substitution neutron diffraction as a probe of the structural environment of cations in superionic glasses, Solid State Ion. 105 (1998) 39–45.

[21] J.C. Mauro, A.K. Varshneya, Multiscale modeling of arsenic selenide glass, J. Non-Cryst. Solids 353 (2007) 1226–1231, Non-Oxide and New Optical Glasses 15.

[22] M. Wilson, B.K. Sharma, C. Massobrio, Ionicity in disordered GeSe2: A comparison of first-principles and atomistic potential models, J. Chem. Phys. (2008) 128.

[23] M. Micoulaut, R. Vuilleumier, C. Massobrio, Improved modeling of liquid $GeSe_2$: impact of the exchange–correlation functional, Phys. Rev. B 79 (2009) 214205.

[24] C. Massobrio, M. Celino, A. Pasquarello, Charge fluctuations and concentration fluctuations at intermediate-range distances in the disordered network-forming materials SiO_2, $SiSe_2$, and $GeSe_2$, Phys. Rev. B 70 (2004) 174202.

[25] C. Massobrio, M. Celino, P.S. Salmon, R.A. Martin, M. Micoulaut, A. Pasquarello, Atomic structure of the two intermediate phase glasses $SiSe_4$ and $GeSe_4$, Phys. Rev. B 79 (2009) 174201.

[26] M. Bauchy, M. Micoulaut, Structure of As_2Se_3 and AsSe network glasses: Evidence for coordination defects and homopolar bonding, J. Non-Cryst. Solids 377 (2013) 34–38.

[27] M. Bauchy, A. Kachmar, M. Micoulaut, Structural dynamic, electronic, and vibrational properties of flexible, intermediate, and stressed rigid As-Se glasses and liquids from first principles molecular dynamics, J. Chem. Phys. (2014) 141.

[28] S. Chakraborty, P. Boolchand, M. Micoulaut, Structural properties of Ge-S amorphous networks in relationship with rigidity transitions: An ab initio molecular dynamics study, Phys. Rev. B 96 (2017) 094205.

[29] G. Ferlat, M. Micoulaut, First principle simulations of liquid and vitreous B_2S_3, Phys. Chem. Glasses-European J. Glas. Sci. Technol. Part B 50 (2009) 284–288.

[30] A. Dive, C. Benmore, M. Wilding, S. Martin, S. Beckman, S. Banerjee, Molecular dynamics modeling of the structure and Na^+-ion transport in Na_2S-SiS_2 glassy electrolytes, J. Phys. Chem. B 122 (2018) 7597–7608.

[31] S.S. Sørensen, M.M. Smedskjaer, M. Micoulaut, Evidence for complex dynamics in glassy fast ion conductors: The case of sodium thiosilicates, J. Phys. Chem. B 127 (2023) 10179–10188.

[32] L.-M. Poitras, M. Micoulaut, Establishment of an empirical force-field for crystalline and amorphous Li_2S- SiS_2 electrolytes, Phys. Rev. B 107 (2023) 214205.

[33] S. Ariga, T. Ohkubo, S. Urata, Y. Imamura, T. Taniguchi, A new universal force-field for the Li_2S–P_2S_5 system, Phys. Chem. Chem. Phys. 24 (2022) 2567–2581.

[34] R.P. Rao, M. Seshasayee, Molecular dynamics simulation of ternary glasses Li_2S–P_2S_5–LiI, J. Non-Cryst. Solids 352 (2006) 3310–3314.

[35] M. Micoulaut, Molecular dynamics simulations of SiS_2-Li_2S-LiI fast ion glasses: Increase of conductivity is driven by network atoms, J. Non-Cryst. Solids 636 (2024) 123017.

[36] R. Zhou, K. Luo, S.W. Martin, Q. An, Insights into lithium sulfide glass electrolyte structures and ionic conductivity via machine learning force field simulations, ACS Appl. Mater. & Interfaces 16 (2024) 18874–18887.

[37] S. Urata, M. Bertani, A. Pedone, Applications of machine-learning interatomic potentials for modeling ceramics, glass, and electrolytes: A review, J. Am. Ceram. Soc. (2024).

[38] Z. Chen, T. Du, N.A. Krishnan, Y. Yue, M.M. Smedskjaer, Disorder-induced enhancement of lithium-ion transport in solid-state electrolytes, Nat. Commun. 16 (2025) 1057.

[39] H. Maekawa, T. Maekawa, K. Kawamura, T. Yokokawa, The structural groups of alkali silicate glasses determined from ^{29}Si MAS-NMR, J. Non-Cryst. Solids 127 (1991) 53–64.

[40] G.S. Henderson, The structure of silicate melts: a glass perspective, Can. Miner. 43 (2005) 1921–1958.

[41] A. Zeidler, J. Drewitt, P. Salmon, A. Barnes, W. Crichton, S. Klotz, H. Fischer, C. Benmore, S. Ramos, A. Hannon, Establishing the structure of GeS_2 at high pressures and temperatures: A combined approach using x-ray and neutron diffraction, J. Phys.: Condens. Matter. 21 (2009) 474217.

[42] H. Diercks, B. Krebs, Crystal structure of B_2S_3: Four-membered B_2S_2 rings and six-membered B_3S_3 rings, Angew. Chem. Int. Ed. Engl. 16 (1977) 313–313.

[43] O.L. Alderman, G. Ferlat, A. Baroni, M. Salanne, M. Micoulaut, C. Benmore, A. Lin, A. Tamalonis, J. Weber, Liquid B_2O_3 up to 1700 K: x-ray diffraction and boroxol ring dissolution, J. Phys.: Condens. Matter. 27 (2015) 455104.

[44] A. Pradel, G. Taillades, M. Ribes, H. Eckert, ^{29}Si NMR structural studies of ionically conductive silicon chalcogenide glasses and model compounds, J. Non-Cryst. Solids 188 (1995) 75–86.

[45] A. Pradel, M. Ribes, Electrical properties of lithium conductive silicon sulfide glasses prepared by twin roller quenching, Solid State Ion. 18 (1986) 351–355.

[46] H. Eckert, J.H. Kennedy, A. Pradel, M. Ribes, Structural transformation of thiosilicate glasses: ^{29}Si MAS-NMR evidence for edge-sharing in the system Li_2S-SiS_2, J. Non-Cryst. Solids 113 (1989) 287–293.

[47] H. Eckert, Z. Zhang, J.H. Kennedy, Glass formation in non-oxide chalcogenide systems. Structural elucidation of Li_2S-SiS_2-LiI solid electrolytes by quantitative ^{29}si, ^{6}Li and ^{7}Li high resolution solid state NMR methods, J. Non-Cryst. Solids 107 (1989) 271–282.

[48] D.E. Watson, S.W. Martin, Short range order characterization of the Na_2S-SiS_2 glass system using Raman, infrared and 29Si magic angle spinning nuclear magnetic resonance spectroscopies., J. Non-Crystalline Solids 471 (2017) 39–50.

[49] P.S. Salmon, Structure of liquids and glasses in the Ge–Se binary system, J. Non-Cryst. Solids 353 (2007) 2959–2974.

[50] R.F. Rowlands, A. Zeidler, H.E. Fischer, P.S. Salmon, Structure of the intermediate phase glasses $GeSe_3$ and $GeSe_4$: the deployment of neutron diffraction with isotope substitution, Front. Mater. 6 (2019) 133.

[51] M. Micoulaut, I. Pethes, P. Jóvári, L. Pusztai, M. Krbal, T. Wágner, V. Prokop, Michalik Š, K. Ikeda, I. Kaban, Structural properties of chalcogenide glasses and the isocoordination rule: Disentangling effects from chemistry and network topology, Phys. Rev. B 106 (2022) 014206.

[52] M. Micoulaut, A. Kachmar, M. Bauchy, S. Le Roux, C. Massobrio, M. Boero, Structure, topology, rings, and vibrational and electronic properties of Ge_xSe_{1-x} glasses across the rigidity transition: A numerical study, Phys. Rev. B 88 (2013) 054203.

[53] B.T. Ahn, R.A. Huggins, Phase behavior and conductivity of Li_2SiS_3 composition, Solid State Ion. 46 (1991) 237–242.

[54] J. Kennedy, Ionically conductive glasses based on SiS_2, Mater. Chem. Phys. 23 (1989) 29–50.

[55] A. Hayashi, N. Masuzawa, S. Yubuchi, F. Tsuji, C. Hotehama, A. Sakuda, M. Tatsumisago, A sodium-ion sulfide solid electrolyte with unprecedented conductivity at room temperature, Nat. Commun. 10 (2019) 5266.

[56] L. Legrand, L.-M. Poitras, N. Sator, M. Micoulaut, Intrinsic limitation of conductivity in depolymerized sodium-ion glassy networks, Solid State Ion. 427 (2025) 116889.

[57] A. Pedone, G. Malavasi, M.C. Menziani, A.N. Cormack, U. Segre, A new self-consistent empirical interatomic potential model for oxides, silicates, and silica-based glasses, J. Phys. Chem. B 110 (2006) 11780–11795.

[58] R. Oeffner, S. Elliott, Interatomic potential for germanium dioxide empirically fitted to an ab initio energy surface, Phys. Rev. B 58 (1998) 14791.

[59] S. Tsuneyuki, H. Aoki, M. Tsukada, Y. Matsui, Molecular-dynamics study of the α to β structural phase transition of quartz, Phys. Rev. Lett. 64 (1990) 776.

[60] A. Kato, M. Nose, M. Yamamoto, A. Sakuda, A. Hayashi, M. Tatsumisago, Mechanical properties of sulfide glasses in all-solid-state batteries, J. Ceram. Soc. Japan 126 (2018) 719–727.

[61] J.D. Gale, Empirical potential derivation for ionic materials, Phil. Mag. B 73 (1996) 3–19.

[62] J.D. Gale, GULP: A computer program for the symmetry-adapted simulation of solids, J. Chem. Soc. Faraday Trans. 93 (1997) 629–637.

[63] J.D. Gale, A.L. Rohl, The general utility lattice program (GULP), Mol. Simul. 29 (2003) 291–341.

[64] M. Bertani, M.C. Menziani, A. Pedone, Improved empirical force field for multicomponent oxide glasses and crystals, Phys. Rev. Mater. 5 (2021) 045602.

[65] M. Bertani, A. Pallini, M. Cocchi, M.C. Menziani, A. Pedone, A new self-consistent empirical potential model for multicomponent borate and borosilicate glasses, J. Am. Ceram. Soc. 105 (2022) 7254–7271.

[66] A.N. Cormack, J. Du, T.R. Zeitler, Alkali ion migration mechanisms in silicate glasses probed by molecular dynamics simulations, Phys. Chem. Chem. Phys. 4 (2002) 3193–3197.

[67] L.T. Kong, Phonon dispersion measured directly from molecular dynamics simulations, Comput. Phys. Comm. 182 (2011) 2201–2207.

[68] L. Koester, H. Rauch, E. Seymann, Neutron scattering lengths: a survey of experimental data and methods, At. Data Nucl. Data Tables 49 (1991) 65–120.

[69] A.C. Wright, The comparison of molecular dynamics simulations with diffraction experiments, J. Non-Cryst. Solids 159 (1993) 264–268.

[70] J.A. Dawson, P. Canepa, M.J. Clarke, T. Famprikis, D. Ghosh, M.S. Islam, Toward understanding the different influences of grain boundaries on ion transport in sulfide and oxide solid electrolytes, Chem. Mater. 31 (2019) 5296–5304.

[71] J. Du, A. Cormack, The medium range structure of sodium silicate glasses: a molecular dynamics simulation, J. Non-Cryst. Solids 349 (2004) 66–79.

[72] N. Bisbrouck, M. Micoulaut, J.-M. Delaye, M. Bertani, T. Charpentier, S. Gin, F. Angeli, Influence of magnesium on the structure of complex multicomponent silicates: insights from molecular simulations and neutron scattering experiments, J. Phys. Chem. B 125 (2021) 11761–11776.

[73] H. Lipson, X-ray diffraction by BE warren, Found. Crystallogr. 27 (1971) 192–192.

[74] B.E. Warren, H. Krutter, O. Morningstar, Fourier analysis of X-ray patterns of vitreous SiO_2 and B_2O_3, J. Am. Ceram. Soc. 19 (1936) 202–206.

[75] O. Masson, P. Thomas, Exact and explicit expression of the atomic pair distribution function as obtained from X-ray total scattering experiments, J. Appl. Crystallogr. 46 (2013) 461–465.

[76] P.J. Brown, A.G. Fox, E.N. Maslen, M.A. O'Keefe, B.T.M. Willis, International Tables for Crystallography, vol. C, Chapter 6.1, IUCr, 2006, pp. 554–595.

[77] A. Cade, E. Philippot, M. Ribes, M. Maurin, Crystal-structure of sodium thiosilicate $Na_4Si_4S_{10}$, C.-R. Acad. Des Sci. Sér. C 274 (1972) 1054–+.

[78] M. Ribes, J. Olivier-Fourcade, E. Philippot, M. Maurin, Etude structurale de thiocomposés à groupement anionique de type tétrane $Na_4X_4s_{10}$ (X=Ge, Si) et $Ba_2Ge_4S_{10}$, J. Solid State Chem. 8 (1973) 195–205.

[79] J. Olivier-Fourcade, E. Philippot, M. Ribes, M. Maurin, Étude structurale d'un thiogermanate de sodium a chaines infinies $(Na_2GeS_3)_n$ caractérisation dans le binaire Na_2S-GeS_2, Rev. Chim. Miner. 9 (1972) 757–770.

[80] J. Olivier-Fourcade, J. Jumas, M. Ribes, E. Philippot, M. Maurin, Evolution structurale et nature des liaisons dans la série des composés soufrés du silicium, du germanium, et de l'étain, J. Solid State Chem. 23 (1978) 155–176.

[81] B. Krebs, Thio-and seleno-compounds of main group elements—novel inorganic oligomers and polymers, Angew. Chem. 22 (1983) 113–134.

[82] B.T. Ahn, Huggins, Structures and conductivities of Li_2SiS_3 phases, Mater. Res. Bull. 25 (1990) 381–389.

[83] N. Tanibata, K. Noi, A. Hayashi, M. Tatsumisago, Preparation and characterization of highly sodium ion conducting Na_3P_4–Na_4SiS_4 solid electrolytes, RSC Adv. 4 (2014) 17120–17123.

[84] S. Harm, A.-K. Hatz, C. Schneider, C. Hoefer, C. Hoch, B.V. Lotsch, Finding the right blend: interplay between structure and sodium ion conductivity in the system Na_5AlS_4–Na_4SiS_4, Front. Chem. 8 (2020) 90.

[85] A. Feltz, G. Pfaff, Zur bindungsenergie der Si-Si und Ge-Ge bindung in den verbindungen $Na_6Si_2X_6$ und $Na_6Ge_2X_6$ (X= S, Se), Z. Für Anorg. Und Allg. Chem. 504 (1983) 173–178.

[86] A. Feltz, G. Pfaff, Die verbindungen $Na_6Si_2S_6$ und $Na_6Si_2Se_6$ und deren Bromspaltungsprodukte Na_3SiSe_3Br und Na_3SiSe_3Br, Z. Für Chem. 23 (1983) 68–68.

[87] M. Micoulaut, L. Poitras, A. Piarristeguy, O. Masson, R. Escalier, B. Ruta, V. Viallet, S. Sørensen, Experimental and theoretical characterisation of the prototypical Na_2S – SiS_2 electrolyte glass : conductivity enhancement is driven by network depolymerization, Phys. Rev. B (2025) 111.

[88] M. Micoulaut, Structure of densified amorphous germanium dioxide, J. Phys.: Condens. Matter. 16 (2004) L131.

[89] P.S. Salmon, Real space manifestation of the first sharp diffraction peak in the structure factor of liquid and glassy materials, Proc. R. Soc. Lond. Ser. A: Math. Phys. Sci. 445 (1994) 351–365.

[90] M. Tenhover, M.A. Hazle, R.K. Grasselli, Atomic structure of SiS_2 and $SiSe_2$ glasses, Phys. Rev. Lett. 51 (1983) 404–406.

[91] M. Tenhover, M. Hazle, R. Grasselli, Atomic structure of SiS_2 and $SiSe_2$ glasses, Phys. Rev. Lett. 51 (1983) 404.

[92] S. Elliott, Extended-range order, interstitial voids and the first sharp diffraction peak of network glasses, J. Non-Cryst. Solids 182 (1995) 40–48.

[93] M. Bauchy, M. Micoulaut, Atomic scale foundation of temperature-dependent bonding constraints in network glasses and liquids, J. Non-Cryst. Solids 357 (2011) 2530–2537.

[94] S.V. King, Ring configurations in a random network model of vitreous silica, Nature 213 (1967) 1112–1113.

[95] B.T. Ahn, R.A. Huggins, Synthesis and lithium conductivities of Li_2SiS_3 and Li_4SiS_4, Mater. Res. Bull. 24 (1989) 889–897.

[97] J. Roh, H. Kim, H. Lee, H. Bu, A. Manjón-Sanz, H. Kim, S.-T. Hong, Unraveling polymorphic crystal structures of Li_4SiS_4 for all-solid-state batteries: Enhanced ionic conductivity via aliovalent Sb substitution, Chem. Mater. 36 (2024) 6973–6984.

[96] A. Weiss, G. Rocktäschel, Zur kenntnis von thiosilicaten, Z. Für Anorg. Und Allg. Chem. 307 (1960) 1–6.

[98] W. Huang, K. Yoshino, S. Hori, K. Suzuki, M. Yonemura, M. Hirayama, R. Kanno, Superionic lithium conductor with a cubic argyrodite-type structure in the Li–Al–Si–S system, J. Solid State Chem. 270 (2019) 487–492.

[99] G. Rocktäschel, W. Ritter, A. Weiss, Ternäre chalkogenide mit elementen der 4. hauptgruppe und olivinstruktur, Z. Für Naturforschung B 19 (1964) 958–958.

[100] R. Dumail, M. Ribes, E. Philippot, Study of a solid solution between barium ortho-thiogermanate and barium ortho-thiosilicate $Ba_x[Si_{1-x}Ge_x]S_4$ crystal structure of Ba_2SiS_4, C.-R. Acad. Sci. Sér. C 272 (1971) 303–+.

[101] J. Lemley, The crystal structure of Ba_2SiS_4, Acta Crystallogr. Sect. B: Struct. Crystallogr. Cryst. Chem. 30 (1974) 549–550.

[102] D. Schmitz, Vergleich der kristallstrukturen von $(NH_4)_3$-$ZnCl_5$ und Ba_3SiS_5, Acta Crystallogr. Sect. B: Struct. Crystallogr. Cryst. Chem. 37 (1981) 518–525.

[103] A. Weiss, G. Rocktäschel, Zur kenntnis von thiosilicaten, Z. Für Anorg. Und Allg. Chem. 307 (1960) 1–6.

[104] Z. Bouguerra, H. Bennacer, A. Boukortt, A.H. Denawi, S. Meskine, Comput. Condens. Matter 41 (2024) e00983.

[105] I. Mikailo, V. Lazarev, E. Peresh, Z. Kish, Phase equilibria in the $Na_2S(Se)$ - $GeS_2(Se_2)$ systems, Zh. Neorg. Khim. 34 (1989) 2319–2323.

[106] E. Plumat, New sulfide and selenide glasses: preparation, structure, and properties, J. Am. Ceram. Soc. 51 (1968) 499–507.

[107] P. Richet, M. Roskosz, J. Roux, Glass formation in silicates: Insights from composition, Chem. Geol. 225 (2006) 388–401.

[108] B. Barrau, M. Ribes, M. Maurin, A. Kone, J.-L. Souquet, Glass formation, structure and ionic conduction in the Na_2S-Ges_2 system, J. Non-Cryst. Solids 37 (1980) 1–14.

[109] M. Ribes, B. Barrau, J. Souquet, Sulfide glasses: glass forming region, structure and ionic conduction of glasses in Na_2S-XS_2 (X=Si; Ge), Na_2S-P_2S_5 and Li_2S-GeS_2 systems, J. Non-Cryst. Solids 38 (1980) 271–276.

[110] J. Souquet, E. Robinel, B. Barrau, M. Ribes, Glass formation and ionic conduction in the M_2S-GeS_2 (M=Li, Na, Ag) systems, Solid State Ion. 3 (1981) 317–321.

[111] C. Bischoff, K. Schuller, N. Dunlap, S.W. Martin, Ir, Raman, and NMR studies of the short-range structures of 0.5 Na_2S+0.5 [X GeS_2+(1–X) PS_5/2] mixed glass-former glasses, J. Phys. Chem. B 118 (2014) 1943–1953.

[112] Z. Zhou, K. Kamiya, K. Tsutsumi, T. Hashimoto, H. Nasu, Structure of Na_2s–GeS_2 sulphide glasses—comparison with Na_2O–GeO_2 oxide glasses, Phys. Chem. Glasses 40 (1999) 146–152.

[113] K. Itoh, T. Fukunaga, Structure of Na_2S–GeS_2 glasses studied by using neutron and X-ray diffraction and reverse Monte Carlo modeling, Solid State Ion. 180 (2009) 351–355.

[114] M. Kassem, T. Bounazef, A. Sokolov, M. Bokova, D. Fontanari, A.C. Hannon, I. Alekseev, E. Bychkov, Deciphering fast ion transport in glasses: A case study of sodium and silver vitreous sulfides, Inorg. Chem. 61 (2022) 12870–12885.

[115] E. Philippot, M. Ribes, O. Lindqvist, Crystal structure of $Na_4Ge_4S_{10}$, Rev. Chim. Miner. 8 (1971) 477.

[116] J. Olivier-Fourcade, E. Philippot, M. Ribes, M. Maurin, Structure cristalline du thiogermanate de sodium Na_2GeS_3, C. R. Acad. Sci. Ser. C, Sci. Chim. 274 (1972) 1185–1187.

[117] J. Olivier-Fourcade, M. Ribes, E. Philippot, M. Maurin, Etude radiocristallographique des thiogermanates de sodium, C. R. Acad. Sci. Ser. C, Sci. Chim. 272 (1971) 1964.

[118] J. Jumas, J. Olivier-Fourcade, J. Vermot-Gaud-Daniel, M. Ribes, E. Philippot, M. Maurin, Etude structurale de thiocomposés á groupements anioniques de type pyro, $Na_6X_2s_7$ (X=Ge, Sn) et $Ba_3Sn_2S_7$, Rev. de Chim. Minérale 11 (1974) 13–26.

[119] H.B. Yahia, K. Motohashi, S. Mori, A. Sakuda, A. Hayashi, Synthesis, structure and properties of Na_4GeS_4, J. Alloys Compd. 960 (2023) 170600.

[120] I. Seo, S.W. Martin, Fast lithium ion conducting solid state thin-film electrolytes based on lithium thio-germanate materials, Acta Mater. 59 (2011) 1839–1846.

[121] V. Tomashyk, Quaternary Alloys Based on IV-VI and IV-VI2 Semiconductors, CRC Press, 2023.

[122] B. Yildiz, A. Erkisi, An ab initio study on the elasticity and optical features of semiconductor lithium-based germanate chalcogenides (Li_8GeS_6 and Li_8GeSe_6), Phys. B 699 (2025) 416851.

[123] R. Kanno, T. Hata, Y. Kawamoto, M. Irie, Synthesis of a new lithium ionic conductor, thio-LISICON–lithium germanium sulfide system, Solid State Ion. 130 (2000) 97–104.

[124] J. Roh, N. Do, A. Manjón-Sanz, S.-T. Hong, Li2GeS3: Lithium ionic conductor with an unprecedented structural type, Inorg. Chem. 62 (2023) 15856–15863.

[125] M. Murayama, R. Kanno, Y. Kawamoto, T. Kamiyama, Structure of the thio-LISICON, Li_4GeS_4, Solid State Ion. 154 (2002) 789–794.

[126] J.H. MacNeil, D.M. Massi, J.-H. Zhang, K.A. Rosmus, C.D. Brunetta, T.A. Gentile, J.A. Aitken, Synthesis, structure, physicochemical characterization and electronic structure of thio-lithium super ionic conductors, Li_4GeS_4 and Li_4SnS_4, J. Alloys Compd. 586 (2014) 736–744.

[127] Y. Matsushita, M.G. Kanatzidis, Crystal structure of a new Li–Ge–S compound, Li_4GeS_4, Acta Crystallogr. Sect. A 52 (1996) C328–C328.

[128] Micoulaut M. Pockets, Jumps and filaments: classifying ionic motion and determining the role of structure in electrochemical properties of $2Li_2S$-GeS_2 superionic glasses, J. Phys.: Condens. Matter. 36 (2024) 195703.

[129] M. Ribes, M. Maurin, Sur le système GeS_2-BaS, C.-R. Acad. Sci. Sér. C 265 (1967) 1461.

[130] H. Vincent, G. Perrault, Structure cristalline des orthothiogermanates de magnésium et de fer, Bull. de Minéralogie 94 (1971) 551–555.

[131] M. Ribes, E. Philippot, M. Maurin, Etude structurale des orthothiogarmenates de calcium et de strontium Mg_2GeS_4 Sr_2GeS_4, C.-R. Acad. Sci. Sér. C 270 (1970) 716.

[132] M.-Y. Pan, S.-Q. Xia, X.-C. Liu, X.-T. Tao, Ba_3GeS_5 and Ba_3InS_4Cl: Interesting size effects originated from the tetrahedral anions, J. Solid State Chem. 219 (2014) 74–79.

[133] K. Wu, X. Su, Z. Yang, S. Pan, An investigation of new infrared nonlinear optical material: $BaCdSnSe_4$, and three new related centrosymmetric compounds: Ba_2SnSe_4, Mg_2GeSe_4, and $Ba_2Ge_2S_6$, Dalton Trans. 44 (2015) 19856–19864.

[134] Y. Matsushita, M.G. Kanatzidis, Synthesis and structure of Li4GeS4a, Z. Für Naturforschung B 53 (1998) 23–30.

[135] M. Ribes, M. Maurin, Etude radiocristallographique des thiogermanates des baryum, Rev. Chim. Min. 7 (1970) 75–86.

[136] K. Wu, S. Pan, Z. Yang, Ba_2GeS_4 and Mg_2SnS_4: synthesis, structures, optical properties and electronic structures, RSC Adv. 5 (2015) 33646–33652.

[137] O.L. Alderman, A.C. Hannon, S. Feller, R. Beanland, D. Holland, The germanate anomaly in alkaline earth germanate glasses, J. Phys. Chem. C 121 (2017) 9462–9479.

[138] X. Lu, C.-L. Tsai, S. Yu, H. He, O. Camara, H. Tempel, Z. Liu, A. Windmüuller, E.V. Alekseev, S. Basak, et al., Lithium phosphosulfide electrolytes for solid-state batteries: Part I, Funct. Mater. Lett. 15 (2022) 2240001.

[139] A. Sakuda, A. Hayashi, M. Tatsumisago, Sulfide solid electrolyte with favorable mechanical property for all-solid-state lithium battery, Sci. Rep. 3 (2013) 2261.

[140] A. Dive, Y. Zhang, Y. Yao, S. Martin, S. Banerjee, Investigations of the structure of Na_2S+P_2S_5 glassy electrolytes and its impact on Na+ ionic conductivity through ab initio molecular dynamics, Solid State Ion. 338 (2019) 177–184.

[141] M. Micoulaut, Diffraction patterns of amorphous materials as a series expansion of neighbor distribution functions, J. Phys.: Condens. Matter. 31 (2019) 285402.

[142] M. Bauchy, M. Micoulaut, From pockets to channels: Density-controlled diffusion in sodium silicates, Phys. Rev. B 83 (2011) 184118.

[143] P. Jund, W. Kob, R. Jullien, Channel diffusion of sodium in a silicate glass, Phys. Rev. B 64 (2001) 134303.

[144] A. Meyer, J. Horbach, W. Kob, F. Kargl, H. Schober, Channel formation and intermediate range order in sodium silicate melts and glasses, Phys. Rev. Lett. 93 (2004) 027801.

[145] A. Hayashi, S. Hama, H. Morimoto, M. Tatsumisago, T. Minami, Preparation of Li_2S–P_2S_5 amorphous solid electrolytes by mechanical milling, J. Am. Ceram. Soc. 84 (2001) 477–479.

[146] K. Homma, M. Yonemura, T. Kobayashi, M. Nagao, M. Hirayama, R. Kanno, Crystal structure and phase transitions of the lithium ionic conductor Li_3PS_4, Solid State Ion. 182 (2011) 53–58.

[147] R. Mercier, J.-P. Malugani, B. Fahys, G. Robert, J. Douglade, Structure du tetrathiophosphate de lithium, Acta Crystallogr. Sect. B: Struct. Crystallogr. Cryst. Chem. 38 (1982) 1887–1890.

[148] Y. Onodera, K. Mori, T. Otomo, A. C. Hannon, S. Kohara, K. Itoh, M. Sugiyama, T. Fukunaga, Crystal structure of $Li_7P_3S_{11}$ studied by neutron and synchrotron X-ray powder diffraction, J. Phys. Soc. Japan 79 (2010) 87–89.

[149] H. Yamane, M. Shibata, Y. Shimane, T. Junke, Y. Seino, S. Adams, K. Minami, A. Hayashi, M. Tatsumisago, Crystal structure of a superionic conductor, $Li_7P_3S_{11}$, Solid State Ion. 178 (2007) 1163–1167.

[150] C. Dietrich, D.A. Weber, S. Culver, A. Senyshyn, S.J. Sedlmaier, S. Indris, J. Janek, W.G. Zeier, Synthesis, structural characterization, and lithium ion conductivity of the lithium thiophosphate $Li_2P_2S_6$, Inorg. Chem. 56 (2017) 6681–6687.

[151] S. Ito, M. Nakakita, Y. Aihara, T. Uehara, N. Machida, A synthesis of crystalline $Li_7P_3S_{11}$ solid electrolyte from 1 2-dimethoxyethane solvent, J. Power Sources 271 (2014) 342–345.

[152] S. Neuberger, S.P. Culver, H. Eckert, W.G. Zeier, J.S. auf der Günne, Refinement of the crystal structure of $Li_4P_2S_6$ using NMR crystallography, Dalton Trans. 47 (2018) 11691–11695.

[153] C. Dietrich, M. Sadowski, S. Sicolo, D.A. Weber, S.J. Sedlmaier, K.S. Weldert, S. Indris, K. Albe, J. Janek, W.G. Zeier, Local structural investigations, defect formation, and ionic conductivity of the lithium ionic conductor $Li_4P_2S_6$, Chem. Mater. 28 (2016) 8764–8773.

[154] R.K. Brow, The structure of simple phosphate glasses, J. Non-Cryst. Solids 263 (2000) 1–28.

[155] J. Capobianco, et al., Structural investigation of $NaPO_3$ glass using molecular dynamics simulation, Phys. Chem. Chem. Phys. 1 (1999) 173–177.

[156] J.-J. Liang, R.T. Cygan, T.M. Alam, Molecular dynamics simulation of the structure and properties of lithium phosphate glasses, J. Non-Cryst. Solids 263 (2000) 167–179.

[157] N. Marchin, S. Urata, J. Du, Effect of three-body interaction on structural features of phosphate glasses from molecular dynamics simulations, J. Chem. Phys. (2024) 161.

[158] R.D. Shannon, Revised effective ionic radii and systematic studies of interatomic distances in halides and chalcogenides, Found. Crystallogr. 32 (1976) 751–767.

[159] E. Hellstrom, R. Huggins, Study of the systems Li_2S-Al_2S_3, Na_2S-Al_2S_3, K_2S-Al_2S_3-preparation, phase study and electrical-conductivity, Mater. Res. Bull. 14 (1979) 881–889.

[160] V. Deshpande, A. Pradel, M. Ribes, Influence of Al_2S_3 on the electrical conductivity of the Li_2S- SiS_2 glass system, Solid State Ion. 28 (1988) 756–761.

[161] J. Sills, S. Martin, D. Torgeson,^{11}B NMR studies of the short range order in wide composition range $x$$Na_2S$-(1-$x$)$B_2S_3$ glasses, J. Non-Cryst. Solids 168 (1994) 86–96.

[162] A. Hayashi, T. Fukuda, H. Morimoto, T. Minami, M. Tatsumisago, Amorphous solid electrolytes in the system Li_2S-Al_2S_3-SiS_2 prepared by mechanical milling, J. Mater. Sci. 39 (2004) 5125–5127.

[163] Y. Ooura, N. Machida, M. Naito, T. Shigematsu, Preparation of amorphous solid electrolytes in the system Li_2S-Al_2S_3-P_2S_5 by high-energy ball-milling methods, J. Japan Soc. Powder Powder Metall. 58 (2011) 279–284.

[164] Y. Ooura, N. Machida, M. Naito, T. Shigematsu, Electrochemical properties of the amorphous solid electrolytes in the system Li_2S–Al_2S_3–P_2S_5, Solid State Ion. 225 (2012) 350–353.

[165] H. Lim, S.-C. Kim, J. Kim, Y.-I. Kim, S.-J. Kim, Structure of Li_5AlS_4 and comparison with other lithium-containing metal sulfides, J. Solid State Chem. 257 (2018) 19–25.

[166] M. Micoulaut, A. Piarristeguy, H. Flores-Ruiz, A. Pradel, Towards accurate models for amorphous gete: Crucial effect of dispersive van der waals corrections on the structural properties involved in the phase-change mechanism, Phys. Rev. B 96 (2017) 184204.

[167] M. Micoulaut, Rigidity and intermediate phases in glasses driven by speciation, Phys. Rev. B 74 (2006) 184208.

[168] M.S. Bødker, J.C. Mauro, S. Goyal, R.E. Youngman, M.M. Smedskjaer, Predicting Q-speciation in binary phosphate glasses using statistical mechanics, J. Phys. Chem. B 122 (2018) 7609–7615.

[169] J. van Waser, Phosphorus and Its Compounds, vol. 1, Interscience Publ. Inc., New York, NY, 1958, p. 123.

[170] S. Le Roux, P. Jund, Ring statistics analysis of topological networks: New approach and application to amorphous GeS_2 and SiO_2 systems, Comput. Mater. Sci. 49 (2010) 70–83.

[171] D. Franzblau, Computation of ring statistics for network models of solids, Phys. Rev. B 44 (1991) 4925.

[172] X. Yuan, A.N. Cormack, Local structures of MD-modeled vitreous silica and sodium silicate glasses, J. Non-Cryst. Solids 283 (2001) 69–87.

[173] J. Du, L.R. Corrales, Structure, dynamics, and electronic properties of lithium disilicate melt and glass, J. Chem. Phys. 125 (2006) 114702.

[174] A. Pant, A reconsideration of the crystal structure of β-$Na_2Si_2O_5$, Acta Crystallogr. Sect. B: Struct. Crystallogr. Cryst. Chem. 24 (1968) 1077–1083.

[175] W.T. McDonald, D. Cruickshank, A reinvestigation of the structure of sodium metasilicate, Na_2SiO_3, Acta Crystallogr. 22 (1967) 37–43.

[176] H. Niu, P.M. Piaggi, M. Invernizzi, M. Parrinello, Molecular dynamics simulations of liquid silica crystallization, Proc. Natl. Acad. Sci. 115 (2018) 5348–5352.

[177] J. Hegedüs, S. Elliott, Microscopic origin of the fast crystallization ability of Ge–Sb–Te phase-change memory materials, Nat. Mater. 7 (2008) 399–405.